INSTITUTO SUPERIOR DE ENGENHARIA DE LISBOA

Departamento de Engenharia de Electrónica e Telecomunicações

On-Chip-Antenna for Millimeter Wave Technology

Raquel Alexandra Louro Ribeiro

Dissertação para obtenção do Grau de Mestre
em Engenharia Eletrónica e de Telecomunicações

Orientadores : Professor Doutor Carlos Mendes
Professor Doutor Pedro Pinho

Júri:

Presidente: Professor Doutor Vitor Fialho

Vogais: Doutora Carolina Gouveia
Professor Doutor Carlos Mendes
Professor Doutor Pedro Pinho

Novembro, 2023

INSTITUTO SUPERIOR DE ENGENHARIA DE LISBOA

Departamento de Engenharia de Electrónica e Telecomunicações

On-Chip-Antenna for Millimeter Wave Technology

Raquel Alexandra Louro Ribeiro

Dissertação para obtenção do Grau de Mestre
em Engenharia Eletrónica e de Telecomunicações

Orientadores : Professor Doutor Carlos Mendes
Professor Doutor Pedro Pinho

Júri:

Presidente: Professor Doutor Vitor Fialho

Vogais: Doutora Carolina Gouveia
Professor Doutor Carlos Mendes
Professor Doutor Pedro Pinho

Novembro, 2023

Para a minha avó

Acknowledgments

First of all, I would like to thank my two supervisors Professor Carlos Mendes and Professor Pedro Pinho for their precious help and guidance during the course of this work. Thank you for believing in me and for being a role model for who I aspire to be in my future career.

I would also like to thank Professor António Teixeira and Instituto de Telecomunicações de Aveiro for giving me the opportunity to engage in the POWER project through a research grant. Their generous support, including the provision of essential equipment, significantly facilitated the successful completion of my work. Thank you for everything.

I would like to express my sincere gratitude to Ricardo Figueiredo for his contribution to the practical aspects of this work.

To my family and friends, I would like to thank you for all the unconditional support and love given in this journey called life.

Lastly, a special thank you to my grandmother who is always present in my thoughts.

Abstract

Recently, On-Chip-Antennas, for both millimeter wave and terahertz technologies, have been one of the most researched topics in the antenna community. The possibility of integrating the antenna with the remaining circuitry in a single chip and possible large data rates (provided by the high frequencies used) are two of the main reasons for interest in this type of technology. However, there are some challenges associated with combining antennas and integrated circuits such as the materials used which are beneficial for integrated circuits but bad for On-Chip-Antennas design.

In this work, two types of antennas were studied, the folded slot antenna and the microstrip patch antenna as potential options for antenna integration. The folded slot antenna on an indium phosphide substrate showed to be a possible solution achieving a bandwidth of 314 MHz, with a maximum gain of 8.5 dBi, half-power beamwidths of 25.3º and 46.8º in the two principal planes, and an efficiency of 51%. The microstrip patch antenna was designed as well on the indium phosphide substrate and achieved a bandwidth of 1.39 GHz with a maximum gain of 5.45 dBi, half power beamwidth of 123.9º and 92.1º in the two principal planes, and an efficiency of 95.5%.

The simulations started with an indium phosphide substrate, however, the indium phosphide substrate manufacture calendar is out of the scope of this dissertation calendar, so, the study continued with the silicon substrate. The microstrip patch antenna on silicon substrate achieved a 2.18 GHz bandwidth, 5.28 dBi maximum gain, a half power beamwidth of 124.1º and 107.9º in the two principal planes, and an efficiency of 89%.

To achieve a more directive radiation pattern, a 2x2 microstrip array was designed. A feeding network was studied and designed consisting of a microstrip line and a microstrip to coplanar waveguide transition. The array, occupying an area of 5x6 mm^2 presented a bandwidth of 5.78 GHz, a gain of 8.5 dBi with 42.7º and 42.6º half power

beamwidth on the principal planes, and an efficiency of 85.5% improving the performance in terms of gain and directivity compared with a single element. In the end, four 2x2 microstrip arrays were built and their input match was measured using a probe station and a VNA where it was observed similar behavior to the simulations.

Keywords: On-Chip-Antenna, Millimeter-wave, Integrated Circuits

Resumo

Recentemente, as antenas em chip, para as tecnologias de ondas milimétricas e terahertz, têm sido um dos tópicos mais pesquisados na comunidade de antenas. A possibilidade de integração da antena com circuitos integrados num único chip e as potenciais taxas de dados elevadas (proporcionadas pelas altas frequências utilizadas) são duas das principais razões de interesse neste tipo de tecnologia. No entanto, existem alguns desafios associados com a combinação de antenas e circuitos integrados como os materiais utilizados que são benéficos para os circuitos integrados mas que prejudicam a performance da antenas.

Neste trabalho, dois tipos de antenas são estudados como potenciais cadidatos para integração, o complementar do dipolo dobrado e a antena impressa retangular. O complementar do dipolo dobrado foi dimensionada num substrato de fosfato de índio e mostrou ser uma possivel solução atingindo uma largura de banda de 314 MHz, ganho máximo de 8.5 dBi, largura de feixe a meia potência de 25.3º e 46.8º nos dois planos principais e uma eficiência de 51%. A antena impressa retangular também dimensionada num substrate de fosfato de índio atingiu uma largura de banda de 1.38 GHz, com um ganho máximo de 5.45 dBi, uma largura de feixe a meia potência de 123.9º e 92.1º nos dois planos principais e uma eficiência de 95.5%.

As simulações começaram com o substrato de fosfato de índio, no entanto, como o calendário de fabrico deste substrato está fora do calendário de entrega da dissertação o estudo continuo com o substrato de silício. A antena impressa no substrato de silício atingiu uma largura de banda de 2.18 GHz, ganho máximo de 5.28 dBi. uma largura de feixe a meia potência de 124.1º e 107.9º nos dois planos principais e uma eficiência de 89%.

De forma a melhor a diretividade da antena, um agregado 2x2 foi dimensionado assim com a sua rede de alimentação que consiste em linhas impressas com uma transição

para guia de onda coplanar. No fim, o agregado ocupou uma área de 5x6 mm^2, apresentou uma largura de banda de 5.78 GHz, um ganho de 8.5 dBi com 42.7º e 42.6º largura de feixe a meia potência nos planos principais, e uma eficiência de 85.5%, melhorando o desempenho em termos de ganho e diretividade em comparação com um único elemento. Por fim, quatro agregados 2x2 foram construídos e o seu coeficiente de refleção foi medido recorrendo à utilização de uma *probe station* e um *VNA*, onde se verificou um comportamento semelhante ao simulado.

Palavras-chave: Antenas em chip, Ondas Milimétricas, Cicuitos Integrados

Contents

List of Figures **xvii**

List of Tables **xxiii**

Acronyms **xxv**

1 Introduction **1**

1.1 Objectives 2

1.2 Report Layout 3

2 On-Chip-Antenna **5**

2.1 OCA on semiconductor substrates 6

2.2 Methods for Improving OCA Performance 7

2.2.1 Substrate manipulation 8

2.2.2 Dielectric resonator antennas 9

2.2.3 Metamaterials 10

2.2.4 Substrate integrated waveguides 11

2.2.5 Multi-Method Approach 12

2.3 Indium Phosphide (InP) 14

3 Folded Slot Antenna (FSA) 17

3.1 Antenna Geometry . . . 17

3.2 FSA in free space . . . 18

3.2.1 Initial design . . . 18

3.2.2 Parametric study . . . 19

3.2.3 FSA design . . . 23

3.3 Printed Folded Slot Antenna (PFSA) . . . 24

3.3.1 permittivity Impact . . . 25

3.3.2 PFSA with Ground plane . . . 28

3.3.3 FPSA design . . . 31

4 Rectangular Microstrip Antenna 35

4.1 Microstrip Design . . . 35

4.2 Microstrip antenna on InP substrate . . . 37

4.2.1 Parametric study . . . 37

4.2.2 Inset Feed . . . 44

4.2.3 Microstrip Patch Final Model on InP . . . 48

4.3 Microstrip Antenna on Silicon substrate . . . 51

4.3.1 Silicon Thickness impact . . . 52

4.3.2 Resistivity impact . . . 56

4.3.3 Microstrip Patch final model in Silicon . . . 57

5 Antenna Array 61

5.1 Array Design . . . 61

5.1.1 Analitical Model . . . 62

5.1.2 Numerical Model . . . 63

5.2 Simulation with discrete port . . . 68

5.3 Feeding network . . . 72

5.4 Microstrip to CPW transition . . . 75

5.4.1 Circular transition . . . 76

5.4.2 Triangular transition 79
5.4.3 Final transition model 82
5.5 Final Array 82
5.6 Antenna Array Measurement 88
5.6.1 Measurement Setup 88
5.6.2 Input Match Measurements 90

6 Conclusions and Future work **93**

References **97**

List of Figures

1.1 Illustration of (a) a McM (b) a SiP (c) a SoC [1]. 2

2.1 Representation of substrate cavity by Micromachining. 8
2.2 Representation of the use of a DRA. 9
2.3 Representation of an AMC. 10
2.4 Representation of SIW. 11

3.1 FSA structure. 18
3.2 Input impedance and input match of the Folded Slot Antenna (FSA) with L = 2.5 mm, g = 0.1, s = 0.3, Wg = 5 mm and Lg = 5 mm. 19
3.3 Impact of L on the input impedance of the FSA. 19
3.4 Impact of L on the S_{11} parameter of the FSA. 20
3.5 Impact of g on the input impedance of the FSA. 20
3.6 Impact of g on the S_{11} parameter of the FSA. 21
3.7 Impact of s on the input impedance of the FSA. 21
3.8 Impact of s on the S_{11} parameter of the FSA. 22
3.9 Impact of Lg on the impedance of the FSA. 22
3.10 Impact of Lg on the S_{11} parameter of the FSA. 23
3.11 Impact of Wg on the impedance of the FSA. 23
3.12 Impact of Wg on the S_{11} parameter of the FSA. 24
3.13 FSA free space optimization. 24

3.14 Impact of permittivity on the impedance of the PFSA. 25
3.15 Impact of permittivity on the S_{11} parameter of the PFSA. 25
3.16 Impedance with different permittivities of the PFSA. 26
3.17 ε_r = 1 impact in the radiation pattern. 27
3.18 ε_r = 12 impact on the normalized radiation pattern. 27
3.19 Distance of the ground plane impact on the S_{11} of the FSA. 28
3.20 Distance of the ground plane impact on the normalized radiation pattern. 29
3.21 S_{11} parameter for different distances of the ground plane with a substrate of $\varepsilon_r = 12$. 30
3.22 Cavity structure. 30
3.23 S_{11} of the PFSA without losses of the InP. 31
3.24 Electric field distribution. 31
3.25 S_{11} of the PFSA with losses of the InP. 32
3.26 FSA final design. 33
3.27 S_{11} of the PFSA with CPW. 33
3.28 Normalized radiation pattern of the final design of the PFSA. 34

4.1 Fringe effect [8]. 36
4.2 Microstrip S_{11} and structure with L = 0.72 mm, W = 0.72 mm, FP = -0.2 mm, Wg = 3 mm and Lg = 3 mm. 38
4.3 Impact of L on the input impedance of the Microstrip antenna. 38
4.4 Impact of L on the S_{11} parameter of the Microstrip antenna. 39
4.5 Impact of W on the input impedance of the microstrip antenna. 39
4.6 Impact of W on the S_{11} parameter of the microstrip antenna. 40
4.7 Impact of fp on the input impedance of the microstrip antenna. 40
4.8 Impact of fp on the S_{11} parameter of the microstrip antenna. 41
4.9 Impact of Wg on the input impedance of the microstrip antenna. 41
4.10 Impact of Wg on the S_{11} parameter of the microstrip antenna. 42
4.11 Impact of Lg on the input impedance of the microstrip antenna. 42
4.12 Impact of Lg on the S_{11} parameter of the microstrip antenna. 43

4.13 Microstrip optimization with discrete port. 43
4.14 Microstrip optimization with discrete port considering dimensions of product HHI-4-2-8. 44
4.15 Impedance point demonstration in inset feed. 44
4.16 Inset feed representation on the antenna. 45
4.17 Impact of *sl* on the input impedance of the microstrip antenna. 45
4.18 Impact of *sl* on the S_{11} parameter of the microstrip antenna. 46
4.19 Impact of *aux* on the input impedance of the microstrip antenna. 46
4.20 Impact of *aux* on the S_{11} parameter of the microstrip antenna. 47
4.21 Impact of *sx* on the input impedance of the microstrip antenna. 47
4.22 Impact of *sx* on the S_{11} parameter of the microstrip antenna. 48
4.23 Microstrip final design. 48
4.24 Final microstrip S_{11} and impedance. 49
4.25 Normalized radiation pattern for final microstrip model on InP. 50
4.26 3D radiation pattern microstrip on InP. 50
4.27 S_{11} microstrip antenna with silicon substrate. 51
4.28 Thickness impact on S_{11} of the microstrip antenna on silicon. 52
4.29 S_{11} and efficiency for several substrate heights of the microstrip antenna on silicon. 53
4.30 Normalized radiation pattern of the microstrip antenna on silicon with a height of 100 µm. 53
4.31 Normalized radiation pattern of the microstrip antenna on silicon with a height of 200 µm. 54
4.32 Normalized radiation pattern of the microstrip antenna on silicon with a height of 300 µm. 54
4.33 Normalized radiation pattern of the microstrip antenna on silicon with a height of 400 µm. 55
4.34 Normalized radiation pattern of the microstrip antenna on silicon with a height of 500 µm. 55
4.35 Normalized radiation pattern of the microstrip antenna on silicon with a height of 600 µm. 56

4.36 Resistivity of the silicon impact on S_{11} of the microstrip antenna. 57
4.37 Normalized radiation Pattern of the microstrip antenna on silicon with low resistivity substrate. 57
4.38 Final microstrip S_{11} and impedance on silicon. 58
4.39 Normalized radiation pattern for final microstrip model on silicon substrate. 59
4.40 3D radiation pattern of microstrip on silicon substrate. 59

5.1 Planar array [8]. 63
5.2 Normalized radiation pattern of 2-element horizontal array with 1.095 mm distancing. 64
5.3 Normalized radiation pattern of 2-element horizontal array with 1.7595 mm distancing. 64
5.4 Normalized radiation pattern of 2-element horizontal array with 2.5 mm distancing. 65
5.5 Normalized radiation pattern of 2-element vertical array with 1.095 mm distancing. 66
5.6 Normalized radiation pattern of 2-element vertical array with 1.7595 mm distancing. 66
5.7 Normalized radiation pattern of 2-element vertical array with 2.5 mm distancing. 67
5.8 Normalized radiation pattern of the 4-element array with 2.5 mm distancing. 68
5.9 2-element horizontal array structure with discrete port. 69
5.10 Normalized radiation pattern of 2-element horizontal array with discrete port. 69
5.11 2-element vertical array structure with discrete port. 70
5.12 Normalized radiation pattern of 2-element vertical array with discrete port. 70
5.13 4-element array structure with discrete port. 71
5.14 Normalized radiation pattern for 4 elements with discrete port. 71
5.15 Array feeding network line 1. 72

5.16 Array feeding network line 1 impedance. 72
5.17 Array feeding network line 2. 73
5.18 Array feeding network line 2 impedance. 73
5.19 Array feeding network line 3. 74
5.20 Array feeding network line 3 impedance. 74
5.21 Array feeding network line 4. 74
5.22 Array final feeding network. 75
5.23 CPW transition to microstrip line. 75
5.24 Microstrip line transition to CPW. 76
5.25 Impact of *dT* on the circular transition. 77
5.26 Impact of *Wgl* on the circular transition. 77
5.26 Impact of *Wgl* on the circular transition. 78
5.27 Impact of *dimCPW* on the circular transition. 78
5.27 Impact of *dimCPW* on the circular transition. 79
5.28 Impact of *dT* on the triangular transition. 79
5.28 Impact of *dT* on the triangular transition. 80
5.29 Impact of *Wgl* on the triangular transition. 80
5.29 Impact of *Wgl* on the triangular transition. 81
5.30 Impact of *dimCPW* on the triangular transition. 81
5.31 S-Parameters final transition. 82
5.32 Array with Microstrip to CPW transition. 83
5.33 S_{11} Array with Microstrip to CPW transition. 83
5.34 Normalized radiation pattern of the array with microstrip to CPW transition. 84
5.35 S_{11} of the array with silicon nitride layers. 85
5.36 Array dimensions. 85
5.37 S_{11} of the final array. 86
5.38 Normalized radiation pattern of the final array. 86
5.39 3D radiation pattern of the final array. 87

5.40 Antennas under test. 87
5.41 Setup equipment. 89
5.42 Contact substrate. 90
5.43 Calibration substrate. 90
5.44 Antenna placement on the probe station. 91
5.45 S_{11} comparison between simulation and measured results. 91

List of Tables

2.1 OCA characteristics. 7

2.2 Overall methods with better efficiency. 13

2.3 OCA performance on InP substrates. 15

3.1 Dimensions of the FSA in free space. 24

3.2 PFSA dimensions and impedance for different permittivities. 26

3.3 InP characteristics 32

3.4 PFSA final dimensions. 32

3.5 PFSA overall performance. 34

4.1 Patch antenna parameters and values. 49

4.2 Microstrip on InP overall performance. 50

4.3 Silicon characteristics. 51

4.4 Patch antenna parameters and values with Silicon substrate. 58

4.5 Microstrip on silicon overall performance. 59

5.1 Radiation pattern aspects for the 2-element horizontal array. 65

5.2 Radiation pattern aspects for 2-element vertical array. 67

5.3 Radiation pattern aspects of the 4-element array. 68

5.4 Prediction vs Simulation for 2-element horizontal array. 69

5.5 Prediction vs Simulation for 2-element vertical array. 70

5.6 Prediction vs Simulation for 4-element array. 71
5.7 Final parameter values for triangular transition. 82
5.8 Comparison between the array fed with the discrete port and transmission line transition to CPW. 83
5.9 Silicon Nitride characteristics. 84
5.10 Array overall performance. 87
5.11 Materials used for practical measurements. 88

Acronyms

AMC Artificial Magnetic Conductor. 10, 11, 12

BCB Benzocyclobutene. 8, 9

CMOS Complementary Oxide Semiconductors. 6, 9, 11, 14
CPW Coplanar Waveguide. 2, 6, 8, 11, 13, 14, 17, 32, 44, 45, 72, 75, 76, 78, 82, 84

DRA Dielectric Resonator Antenna. 9

FSA Folded Slot Antenna. xvii, 17, 18, 19, 21, 26, 35, 49

GaAs Gallium Arsenide. 14

InP Indium Phosphide. 3, 5, 14, 31, 32, 34, 35, 37, 44, 51, 58

LWA Leaky-Wave Antenna. 15

McM Multi-chip module. 1
MEMS Micro-electro-Mechanical System. 13
MTS Metasurface. 10

OCA On-Chip Antenna. 2, 3, 5, 6, 7, 8, 10, 13, 14, 56, 88

PCB Printed Circuit Board. 11, 32, 44, 88

PFSA Printed Folded Slot Antenna. 17
PIC Photonic Integrated Circuits. 2, 3

RF Radio Frequency. 1

SiGe Silicon-Germanium. 12
SiP System-in-Package. 1
SIW Substrate Integrated Waveguide. 7, 11, 12, 13
SoC System-on-Chip. 1

1

Introduction

Traditional wireless systems have historically been structured around four distinct functionality-specific modules: the digital baseband module responsible for signal processing, the mixed-signal module, the Radio Frequency (RF) front-end, and the antenna for signal transmission. The horizontal integration of these distinct functional modules gave rise to Multi-chip module (McM) technology. However, this method occupies a significant amount of chip space, presenting a notable drawback, particularly in the face of the ongoing trend of reducing sizes in cellular and other wireless devices [1]. So, to reduce the size, a viable alternative is the vertical integration approach, known as System-in-Package (SiP) technology. While SiP technology proves to be a useful alternative, the antenna still remains outside the package due to its size, since it is the largest component of the system and, for higher frequencies, the integration between different technologies can lead to losses and increased costs since it is necessary to use wire bond connections or flip-bonding [1].

The System-on-Chip (SoC) concept has emerged as a response to the demand for compact, economical, and low-power wireless systems. The SoC integration method has gained significant interest, where all sections of modern wireless systems are integrated onto a single chip. This integration mitigates the need for off-chip interconnections and packaging processes associated with off-chip antennas. As the application landscape moves towards higher frequencies, particularly millimeter-waves and terahertz bands, antenna sizes have reduced to only a few millimeters, enabling both the possibility and practicality of on-chip implementation [1]. These three technologies are

illustrated in Figure 1.1.

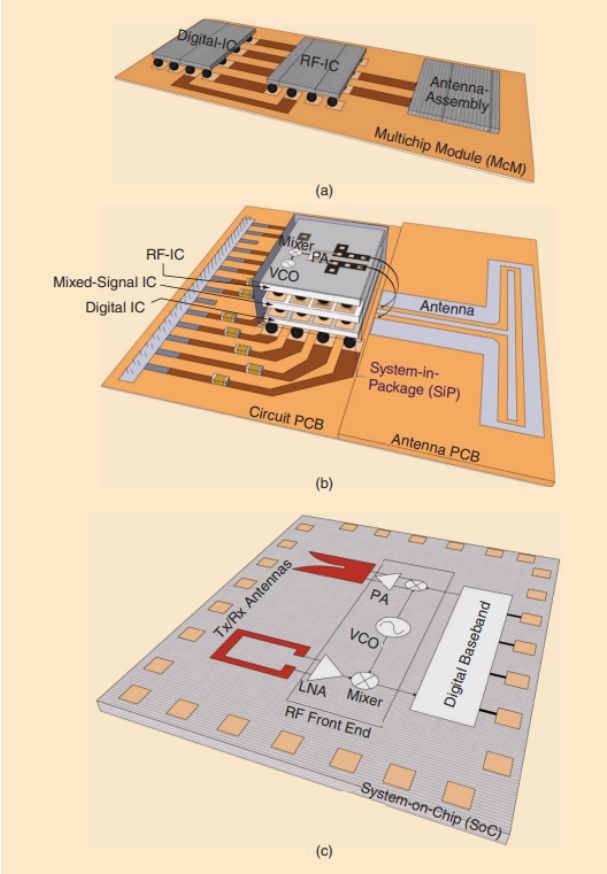

Figure 1.1: Illustration of (a) a McM (b) a SiP (c) a SoC [1].

The integration between an antenna and integrated circuits combined with high frequencies turns the On-Chip Antenna (OCA) an attractive solution since it has the advantage of being small and supporting large data rates having a great potential for applications such as IoT devices, communication modules for 5G, highly integrated transceivers for a wireless personal area and more [1].

1.1 Objectives

The main goal of this dissertation is to build an OCA to operate in the millimeter wave band, specifically in the 60 GHz frequency. This antenna will be integrated into a Photonic Integrated Circuits (PIC), a technology that combines both optical and electronic components on a single chip [2]. So, when designing the OCA, it is crucial to consider the feeding structure, especially since the RF signal will originate from a PIN with a Ground Signal Ground (GSG) output making the Coplanar Waveguide (CPW) the

most suitable feeding technique for the antenna. Moreover, the antenna should be designed to exhibit a directive radiation pattern, anticipating future integration possibilities within communication systems. To achieve this goal it is necessary to understand the challenges associated with building an OCA. Therefore, the following specific goals have been established:

- Study the state of the art of OCA. Have a clear understanding of the trade-offs of the technologies used when building this system;
- Perform simulations of the chosen antennas including parametric studies, methods to solve the problems encountered in the state of the art, and compare results regarding each antenna and technology used;
- Build and simulate an array and a feeding network in order to improve the antenna performance;
- Build the antenna and compare the simulated and measured results.

1.2 Report Layout

This dissertation contains six chapters crucial to the main conclusions of this dissertation.

In the second chapter, is present a literature review that contains the main obstacles to be faced when designing on-chip antennas on typical silicon based substrates, some of the antennas present in the literature, and methods to improve the efficiency and gain of these antennas. This chapter ends with a brief explanation of Indium Phosphide (InP) substrates, which have shown promise for PICs, and some antenna designs integrated into this substrate, marking the beginning of this dissertation work by exploring the possibility of integrating an antenna on an InP substrate.

In Chapter 3, we delve into the first antenna under study, which is the folded slot antenna. A parametric study of the antenna is conducted in this chapter. It also covers one of the expected problems when building an OCA, which is the high permittivity of semiconductor substrates, introducing the characteristics of the InP substrate. Conclusions about this structure are drawn, paving the way for the next chapter.

Chapter 4, we explore the microstrip antenna for this application, first on an InP substrate, and we make a comparison between this antenna and the folded slot antenna.

Additionally, we study the microstrip antenna on a silicon substrate. The silicon substrate introduces other problems covered in the state of the art, and in this chapter, we aim to address these problems, such as thick substrates and high resistivity.

Chapter 5, we design an array. This chapter covers the theory of arrays, simulation results for the array, and the process of building the feed network for this structure. Four array antennas were built and the input match was measured. A brief explanation of the process of measuring antennas in a probe station and a comparison between the measured and simulated results was made.

Lastly, in Chapter 6, we present the conclusions of this dissertation and outline future work.

2

On-Chip-Antenna

Implementing an OCA can be challenging due to the many aspects that can compromise the antenna's performance. This Chapter focuses on the problems that arise from building an OCA such as building an antenna on chip-based materials, with high permittivity, low resistance, and thickness that affect the antenna's efficiency and gain. Although millimeter wave and Terahertz technology offer promising opportunities for antenna integration on chip, working with high frequencies results in increased free-space path loss. Since high frequencies are relevant for the received signal, the antenna must be dimensioned to have high gain so that the systems can be used for longer distances [3]. Additionally, there is an increase in propagation losses due to the radio waves being absorbed by gases in the atmosphere, making these links better suited for short distances [4], [5]. Also, during the fabrication of the antenna, there can be imperfections in the manufacturing process that lead to gain and efficiency deterioration. Therefore, it is important to characterize the antenna for parameters such as input impedance, gain and radiation for these potential tolerances [1].

This chapter discusses the challenges encountered when designing an OCA and explores methods used to enhance gain and radiation efficiency. It is followed by a section introducing the InP technologies that will be explored in this dissertation as the substrate used to design the antenna.

2.1 OCA on semiconductor substrates

OCA has been a great topic of research over the years. Some of the first appearances of these antennas were reported in 1986 [6] and in 1988 [7]. However, as shown in these papers these antennas have poor performances not being suited for practical applications.

The most suited substrates for integrated circuits are semiconductors, like silicon, indium phosphide, silicon-germanium, and others, that usually have low resistivity of $\approx 10\ \Omega \cdot cm$ which is beneficial for integrated circuits but, not appropriate for on-chip antennas. Low resistivity implies a high loss tangent degrading the antenna gain [1]. Another issue that comes with the substrate is its high dielectric constant [1]. Silicon substrates have a permittivity of ≈11.7 causing most power to be radiated into the substrate instead of being radiated into free-space degrading the antenna radiation efficiency. Furthermore, silicon substrates are usually thick which increases the possibility of surface waves [8], [1]. In the following paragraphs there are some examples of dimensioned OCAs that do not rely on more elaborate techniques that exhibit low gain and efficiency due to the silicon substrate used.

In [9] an on-chip yagi antenna is proposed to operate in the 60 GHz band. The antenna was fabricated with a 0.18 μm standard Complementary Oxide Semiconductors (CMOS) process using CPW feeding technique. The CPW mode excitation was preferred in this paper to avoid interference of the electromagnetic fields with the other on chip components. The maximum measured gain was -10 dBi with a simulated radiation efficiency of 10%.

A planar monopole antenna in a standard CMOS process is present in [10]. The proposed antenna is designed with a 50 Ω substrate-shielded CPW line as a feeding network. The antenna maximum gain was 0.1 dBi with a radiation efficiency of around 39% at 60 GHz.

In [11], a on-chip inverted-F and quasi-Yagi antenna were built for 60 GHz with back-end-of-line process of silicon substrates. The results show that inverted-F achieved a gain of -19 dBi at 61 GHz and the quasi-Yagi antenna a -12.5 dBi at 65 GHz.

In [12], a 60 GHz CMOS RFIC-on chip triangular monopole antenna is present. Fed through a CPW line, the antenna was fabricated with a 0.18 μm CMOS process achieving a -9.4 dBi gain and 12% simulated radiation efficiency.

Several on-chip antenna structures fabricated with standard CMOS technology are

present in [13]. The antennas studied in this paper are the dipole antenna, Yagi antenna, rhomic antenna, and loop antenna for the 60 GHz band. The dipole antenna radiation efficiency was 9% and the maximum gain -6.7 dBi. For the Yagi antenna, the highest gain was -3.55 dBi and a radiation efficiency of 15.8%. The overall gain of the rhombic antenna as -0.2 dBi with a radiation efficiency of 85% and the loop antenna's overall gain was -1.2 dBi and radiation efficiency of 77%. The rhombic antenna showed the highest gain reported in [13].

In [14], a 60 GHz on-chip antenna based on silicon technology is design based on a monopole antenna. Gain of -4.96 dBi was achieved for 60 GHz.

Table 2.1 contains the characteristics of the antennas mentioned above, which as it is possible to verify have low gains and efficiency, proving the impact of using such substrates on antennas.

Table 2.1: OCA characteristics.

Ref	Antenna	Frequency	Gain	Efficiency
[9]	Yagi	60 GHz	-10 dBi	10%
[10]	Planar monopole	60 GHz	0.1 dBi	39%
[11]	Inverted-F	61 GHz	-19 dBi	––
[11]	Quase-Yagi	65 GHz	-12.5	––
[12]	Triangular monopole	60 GHz	-9.4 dBi	12%
[13]	Dipole	60 GHz	-6.7	9%
[13]	Yagi	60 GHz	-3.55 dBi	15.8%
[13]	Rhomic	60 GHz	-0.2 dBi	85%
[13]	Loop	60 GHz	-1.2 dBi	77%
[14]	Monopole	60 GHz	-4.96 dBi	––

2.2 Methods for Improving OCA Performance

Several techniques can be applied to improve the OCA gain and efficiency. In this section, some of these methods like micromachining, superstrates, metamaterials, and Substrate Integrated Waveguide (SIW) are approached on antennas integrated on silicon based substrates.

2.2.1 Substrate manipulation

As mentioned before, one of the biggest problems with OCA's is the substrate characteristics that lead to poor radiation efficiency and gain. One of the ways to contradict this behavior is by removing parts of the substrate creating a cavity, as demonstrated in Figure 2.1, through micromachining. That causes a reduction of the permittivity value of the substrate and lowers the overall losses due to surface waves. However, this method can cause mechanical instabilities of the backend process [15], increases fabrication complexity, poor flexibility [16] and not all foundries support this mechanism.

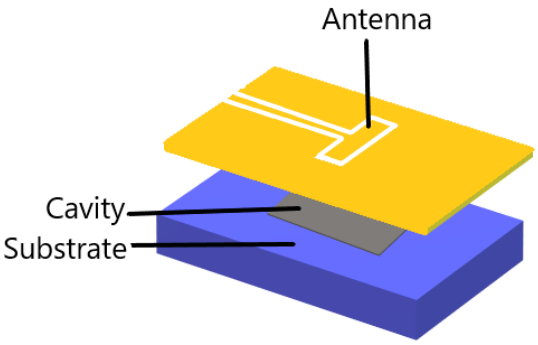

Figure 2.1: Representation of substrate cavity by Micromachining.

In [17], a monopole antenna and a 2x1 patch antenna array fabricated on a two-layer Benzocyclobutene (BCB) material membrane are present. Through micromachining, the silicon material was removed creating a cavity surrounded by metal and filled with polymer providing better support to the membrane than a conventional air cavity. The proposed antenna designs achieved a 12 GHz and 11.5 GHz bandwidth and 6.74 dBi at 131 GHz and 8.66 dBi at 130 GHz gain respectively.

A single patch antenna and a 2x1 patch antenna array fed by CPW are present in [18]. Micromachining technology is used to improve antenna performance. In the antenna proposed structure, the patch and the feed line are optimized separately with a substrate. The simulated gain and radiation efficiencies are 8.7 dBi and 96%, respectively for the single patch antenna, and 9.9 dBi and 94% for the 2x1 patch array.

2.2.2 Dielectric resonator antennas

Another approach to improve the antenna's performance is by using a Dielectric Resonator Antenna (DRA). By using a suitable excitation technique, a dielectric structure can become a radiator at certain frequencies [19]. DRAs can have various shapes such as cylindrical shown in Figure 2.2. In [20], [21], [22] the use of a dielectric resonator antenna shows to have an impact on the antenna performance. A single large-sized DRA is proposed in [23] to increase the antenna gain of each element of a CMOS antenna array. The results showed an improvement of 7 dB gain over a traditional on-chip patch antenna.

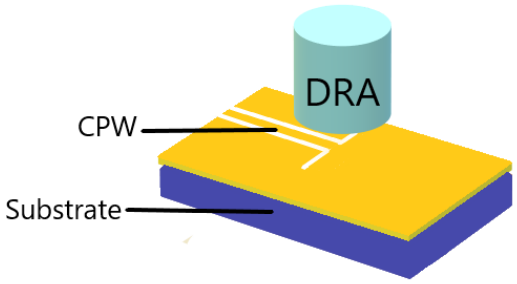

Figure 2.2: Representation of the use of a DRA.

In [24], a dual-linear polarized on-chip mm-wave radiator based on a dielectric resonator is designed. The dielectric resonator is a sphere of 1 mm diameter made of Alumina ceramic material. Through a microstrip resonator, the dielectric resonator is excited and fed with a 50 Ω microstrip feed line both fabricated on a thin on-chip BCB dielectric. A prototype test antenna was designed to operate at 104 GHz achieving a 7-9 dBi gain and simulated peak efficiency of 80%.

A Terahertz dielectric resonator antenna is present in [25]. The proposed antenna is made of high-resistivity silicon material and a feeding patch realized in a 0.18 μm CMOS technology to excite the desired electromagnetic mode. The simulated antenna achieved a 7.9 dBi gain and radiation efficiency of 74% at 341 GHz.

2.2.3 Metamaterials

A metamaterial is a material designed to have custom properties that do not exist in the original material. They are produced by the manipulation of internal material structures through different techniques. According to the shape, geometry, size, orientation, and arrangement, it is possible to manipulate electromagnetic waves by blocking, absorbing, or enhancing waves. Metasurfaces can be considered planar versions of metamaterials with subwavelength thickness [26]. Metasurfaces have been a significant topic of research due to the many applications they can be used. These artificial sheet materials, which are usually composed of metallic patches or dielectric etchings in planar or multi-layer configurations, have the advantages of light weight, ease of fabrication, and ability to control wave propagation both on the surface and in the surrounding free space [26].

Artificial Magnetic Conductor (AMC) also known by High Impedance Surface (HIS) is a type of metamaterial characteristic due to its negative magnetic permeability. A representation of this technique is present in Figure 2.3. The AMC structure in [27], is used as a ground plane to reduce the antenna profile. However, implementing an AMC comes with disadvantages such as the extra space that occupies on the chip area [28],[29] and cost [30].

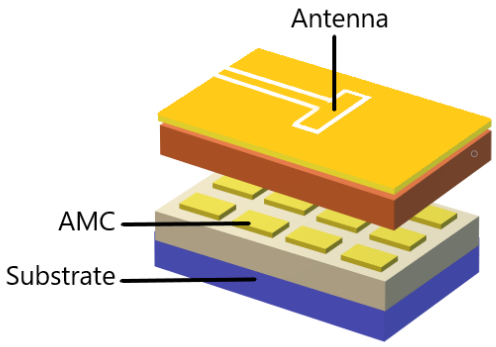

Figure 2.3: Representation of an AMC.

In [31], an octagonal shorted annular ring antenna is built. According to [31] the characteristics of this antenna reduce the excitation of surface waves which is one of the most important problems of an OCA. This antenna was fabricated using a 130 nm silicon-germanium BiCMOS process and to improve gain a 1x2 octagonal shorted annular ring antenna array was built reaching a 4.1 dBi gain at 320 GHz and 17 GHz bandwidth.

A simple prototype of a Metasurface (MTS) based OCA is present in [32]. The antenna

structure consists of two layers of polyimide-substrated with 0.1 nm thickness that sandwich a middle metallic ground-plane layer of 50-μm thickness. The metasurface is on the top layer created by a series of linear slots etched on the radiation patches. This showed to improve the radiation performance of the antenna without affecting the overall footprint. Using a reference on-chip antenna it was possible to compare the effect of the metasurface that showed to improve the radiation gain, radiation efficiency, and reflection coefficient obtaining a 2.5 dBi gain, 40% radiation efficiency, and over 20 GHz bandwidth.

In [33], an on-chip circular ring-shaped monopole antenna based on 0.18 μm CMOS process with an AMC is designed. The antenna is fed by a 50 Ω CPW. By adding the AMC plane, the gain improved by 0.77 dB at 60 GHz and the radiation efficiency improved from 29% to 35%.

2.2.4 Substrate integrated waveguides

A SIW structure consists of a synthetic rectangular electromagnetic waveguide formed in a dielectric substrate. The upper and lower metal plates of the substrate are connected by two rows of vias delimiting the wave propagation area, as demonstrated in Figure 2.4. The advantages of this method are the ability to implement a compact and cost-effective waveguide-like structure using standard wPrinted Circuit Board (PCB) techniques and low loss, high-quality factor, good power handling capability, and shielding, and can be easily integrated with planar circuitry [34].

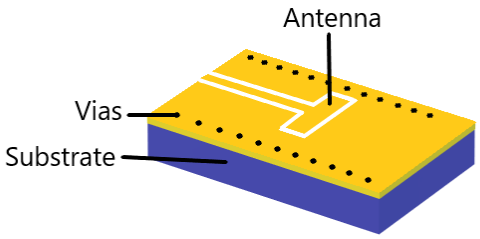

Figure 2.4: Representation of SIW.

A 340 GHz SIW cavity-backed on-chip antenna is present in [35]. The antenna is fabricated using standard silicon technology and its structure, a rectangular slot loop is etched into the upper wall to form a magnetic current loop radiator. A single antenna and a 2x2 antenna array were designed, achieving a maximum gain of 7.9 dBi with an efficiency of 48% at 340 GHz.

In [36], three array designs using SIW are proposed, to work in the Q-band. First, a 8x8 magneto-eletric dipole antenna design to work at 37 GHz. The peak gain of the antenna was 26.7 dBi and a radiation efficiency of 83.2% was obtained for 40 GHz. In the 45 GHz frequency, a SIW-fed cross-slot antenna element was designed. The proposed 4x4 antenna array was fabricated obtaining a measured peak gain of 19.4 dBi at 50 GHz and a radiation efficiency of 81.7% at the same frequency. Still in this paper, a 8x8 antenna array fabricated in LTCC process for the 145 GHz frequency achieved a measured peak gain of 20.5 dBi and radiation efficiency of 59.2%.

2.2.5 Multi-Method Approach

As seen in the literature these techniques work, resulting in an improvement in the antenna performance and it is common to use more than one of these mechanisms to try and enhance gain, radiation efficiency, and bandwidth.

In [37] a Yagi-like structure antenna with SIW and cavity is designed using a standard 0.13 μm Silicon-Germanium (SiGe) BiCMOS technology. By using a dielectic resonator vertically stacked on the antenna forming the 3D Yagi-like it was possible to increase the antenna gain and radiation efficiency achieving 10 dBi and 80% at 340 GHz respectively.

An on-chip antenna based on metamaterial and SIW for the millimeter and terahertz band is designed in [38]. The proposed structure comprises five alternating layers of metallization and silicon and an array of circular radiation patches slots with metamaterial slots are etched. Below the silicon layer is a cavity and underneath this layer is an open-ended microstrip feedline used to excite the antenna. The antenna provided an average measured gain of 6.9 dBi and radiation efficiency of 53%.

In [39] the same authors from [32] proposed a similar novel antenna design using metasurface and was implemented on two layers of polyimide substrates using AMC structure. The use of AMC suppresses the surface waves reducing the substrate losses. This structure exhibited a very large bandwidth of 350-385 GHz, an average gain of 8.15 dBi, and 65.71% radiation efficiency. The same authors also design an antenna array to operate over 0.450-0.475 GHz comprising two dielectric resonators in [40] placed on the surface of the slot antenna. According to the authors, the combination of slot and vias transforms the antenna into a metamaterial structure providing a small footprint. The antenna achieved a maximum gain of 4.5 dBi and 45.7% radiation efficiency.

Another example of the combination of metasurface and SIW technologies is in [41]. In addition to those technologies, an effective RF cross-shaped feed structure is added

to excite the antenna from its underside by coupling which, according to the authors, facilitates the integration with the integrated circuits. The OCA shows to have a gain and efficiency of 8.5 dBi and 67.5%, respectively, on a frequency range of 200-220 GHz.

In another approach, a CPW-fed suspended-on-chip phased array is designed in [42]. By using a micro-electro-mechanical system Micro-electro-Mechanical System (MEMS), creating a low ε_r substrate of air instead of a lossy silicon substrate the radiating elements were suspended improving the radiation efficiency. The antenna is a 5x5 array peak realized gain was 19.7 dBi achieving a radiation efficiency $\geqslant$ 80% at 60 GHz.

Discussion

Upon reviewing the previous OCA designs, it becomes evident that each of these techniques contributes to enhancing antenna performance. Since the examples provided encompass various antenna designs, frequencies, and technologies, it would not be fair to directly compare these methods and determine which one is the best choice. However, when we examine the results and focus on those with an efficiency greater than 80%, we find that the microstrip antenna using micromachining, the dielectric resonator antenna, the magneto-electric dipole array, the 4x4 metallic cross slots array using SIW, and the Yagi-like array using SIW and a dielectric resonator exhibit superior performance in terms of efficiency and gain for this application. The characteristics of these antennas are summarized in Table 2.2. Despite these methods proving to be an asset for increasing antenna performance, during this dissertation, other ways of obtaining better performance will be explored to avoid design complexity.

Table 2.2: Overall methods with better efficiency.

Ref	Method	Frequency	Gain	Efficiency
[18]	Micromachining	60 GHz	8.7	96%
[18]	Micromachining	60 GHz	9.9	94%
[24]	Dieletric resonator	104 GHz	7-9	80%
[36]	SIW	37 GHz	26.7	83.2%
[36]	SIW	45 GHz	19.4	81.7%
[37]	SIW and DR	340 GHz	10	80%
[42]	MEMS	60 GHz	19.7	80%

2.3 Indium Phosphide (InP)

This thesis proposes to focus on the OCA design and performances. However, as one of the important topics for OCA is the technology used for the structure, a small review on InP platform for photonic integrated circuits is done in this section with the introduction of OCA's using this platform. Most of the work present so far shows the construction of OCA on silicon substrates. This may have to due with the small cost compared with Gallium Arsenide (GaAs) and InP material.

Depending on the system requirements, the materials used for integrated circuits fabrication technology must be carefully chosen to guarantee integration and compatibility with the different system blocks. The main technologies available are CMOS, silicon germanium or semicondutors from group III-V such as GaAs or InP [43], [44].

The InP platform is one of the most advanced platforms for high-performance and has the advantage over silicon by allowing monolithic integration of all the required active elements improving the system reliability, reduction on packaging cost, system footprint, fiber coupling loss, and power consumption [45].

In [46], a 4x4 planar array antenna on indium phosphide is designed and fabricated to operate at 300 GHz. The antenna is fed by a CPW feed line and the antenna element is composed of a top metal, dielectric substrate, and bottom floating metal layer. One side directional radiation is possible by optimizing the length of the bottom layer. At 300 GHz the antenna gain is 11.7 dBi.

A novel linear polarized cavity-backed antenna is simulated in [47]. The backed cavity of the antenna is triangular shaped and it is done by metallic via arrays in the InP substrate. The antenna is fed by an inset coplanar waveguide and reaches a 3.8 dBi gain and 89% radiation efficiency.

A grounded and diced bow-tie slot antenna with a stub for terahertz application is present in [48]. The antenna is fed by CPW and by limiting the area around the conductor is possible to reduce the substrate effects. The ground plane below acts as a reflector and re-directs the energy to the air-side region of the antenna. The antenna gain is 11 dBi at 280 GHz and achieved an average of 92% radiation efficiency.

In [49] an on-chip patch antenna design on InP substrate. The antenna is fed by ECPW transition to a rectangular waveguide and for higher directivity, a horn antenna is used to form an extended packaging structure. The simulated gain is 11.9 dBi.

An on-chip rectangular waveguide-to-microstrip transition using a dipole antenna with an integrated balun is present in [50]. The proposed structure allows a compact size,

simple design, and broad bandwidth characteristics.

In [51], a bow-tie antenna loaded with a bullet silicon lens is proposed. The use of a lens increases the gain and radiation efficiency of the antenna however, the use silicon lens can narrow the antenna bandwidth. The antenna shows a gain of 13.5 dBi and an efficiency of 90%.

In [52], a beam steering leaky-wave antenna is reported. According to the authors, leaky-wave antennas are attractive because they do not require complex feeding control circuits and the beam steering is simply accomplished. The average realized gain was 11 dBi for a single Leaky-Wave Antenna (LWA) and for an array of 3 LWA maximum realized gain was over 18 dBi.

Table 2.3 presents the characteristics of the antennas mentioned above.

Table 2.3: OCA performance on InP substrates.

Ref	Antenna	Frequency	Gain	Efficiency
[46]	4x4 antenna array	300 GHz	11.7 dBi	−−
[47]	Linear polarized cavity-backed	60 GHz	3.8 dBi	89%
[48]	Grounded and diced bow-tie slot	230-325 GHz	11 dBi	92%
[49]	Patch	140 GHz	12.3 dBi	−−
[51]	Bow-tie with lens	340 GHz	13.5 dBi	90%
[52]	4 array LWA	230-330 GHz	18 dBi	−−

3

Folded Slot Antenna (FSA)

In this section, one of the antennas under study is introduced: the FSA. This antenna was chosen due to its ease of integration with the CPW line. A parametric study of this antenna is presented, along with an exploration of the impact of introducing substrates with different permittivities on the impedance and radiation pattern. The impact of the introduction of a reflective ground plane is also evaluated.

3.1 Antenna Geometry

The geometry of the Printed Folded Slot Antenna (PFSA) is shown in Figure 3.1. This is a printed version of a complementary of the folded dipole antenna where the antenna is surrounded with conductive material in specific copper and center fed with a discrete port. According to [8], a folded dipole has a length L given by Equation 3.1 where λ represents the wavelength and the parameters corresponding to the width (s) $\ll L$ and the gap (g) $< s$.

$$L \approx \frac{\lambda}{2} \tag{3.1}$$

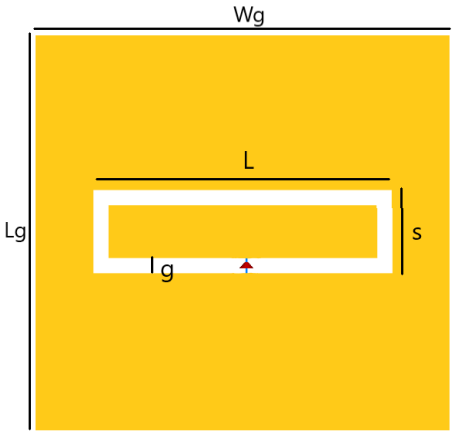

Figure 3.1: FSA structure.

3.2 FSA in free space

To simplify the model, the antenna substrate will not be included in the initial design. This antenna will be referred to as FSA in free space. The impact of the substrate will be evaluated at a later stage.

3.2.1 Initial design

Considering Equation 3.1, the theoretical value for the length is 2.5 mm. Since the values for the gap and width have to be much smaller than the length, a first approach considered the $g = 0.1$ mm, $s = 0.3$ mm and the Wg and Lg to be 5 mm corresponding to λ. The input impedance is shown in Figure 3.2a and the corresponding input match, referred to 50Ω, is shown in Figure 3.2b. As can be seen, the antenna presents two resonances at 54.2 GHz and 69.5 GHz with a peak real part at 53 GHz. The best input match was obtained at 66 GHz and a level of -10.23 dB was observed at the target frequency of 60 GHz. As the antenna is slightly detuned, with the best input match at a higher frequency than the target, adjustments have to be made to retune the antenna. For that purpose, a parametric study of the effect of every geometry parameter will be performed.

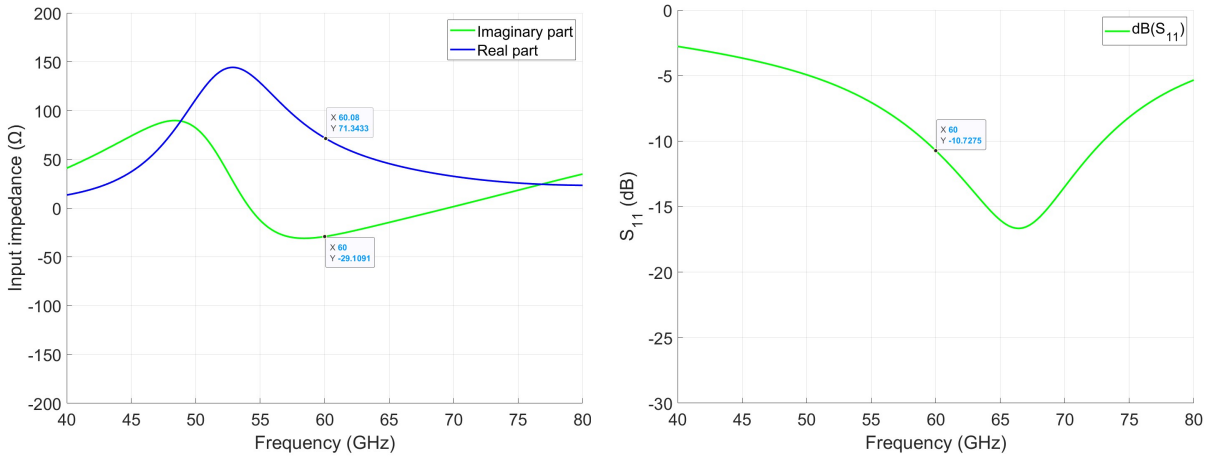

(a) Impedance Imaginary Part. (b) S_{11}.

Figure 3.2: Input impedance and input match of the FSA with L = 2.5 mm, g = 0.1, s = 0.3, Wg = 5 mm and Lg = 5 mm.

3.2.2 Parametric study

First, a parametric study of L is conducted. The impact of the variation of L in the input impedance is shown in Figure 3.3 and the input match is shown in Figure 3.4. As we can see, increasing the value of the parameter L decreases the resonant frequency, the same behavior is observed in the impedance graphics where there is a shift in the real and imaginary parts of the impedance that decreases when the length of the slot increases.

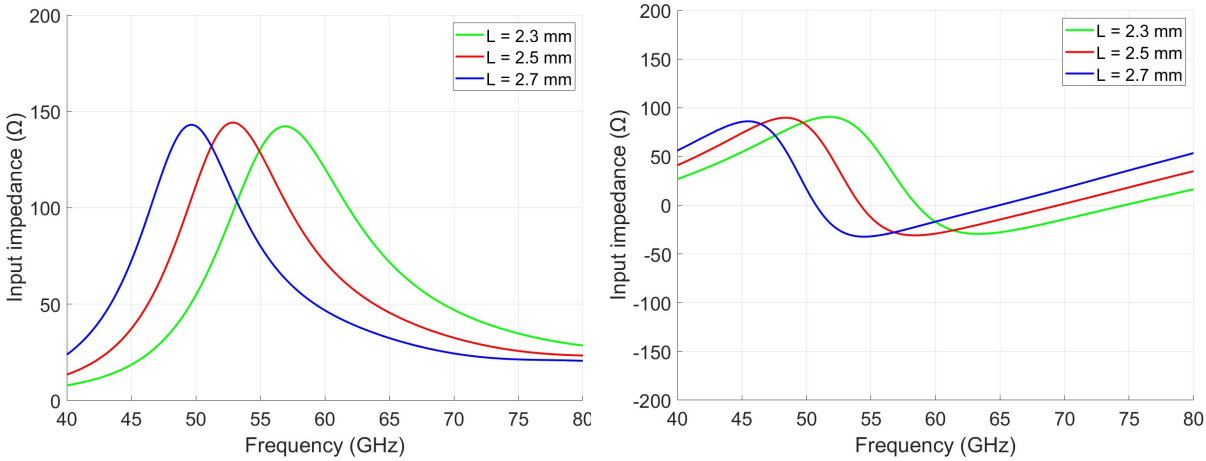

(a) Real Part. (b) Imaginary Part.

Figure 3.3: Impact of L on the input impedance of the FSA.

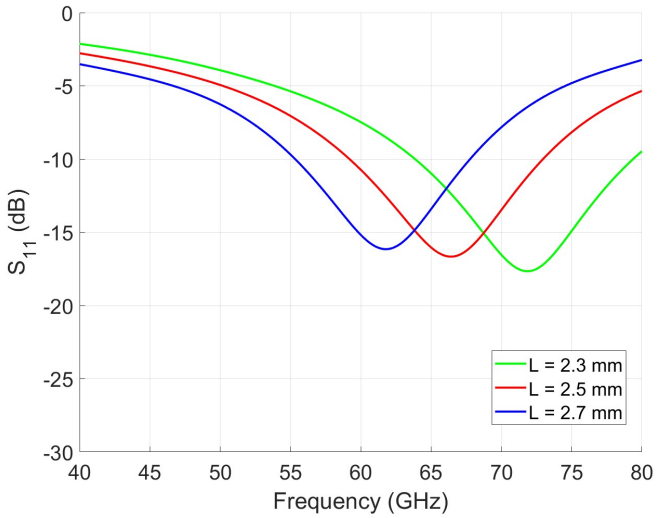

Figure 3.4: Impact of L on the S_{11} parameter of the FSA.

As mentioned earlier, both the g and s parameters must be much smaller than L, and s must be greater than g. Starting with the g parameter, the input impedance is shown in Figure 3.5 and the input match in Figure 3.6. As can be seen when evaluating the impedance it becomes apparent that as the gap increases, both the real and imaginary parts of the impedance also increase. As for the S_{11}, as the gap increases the S_{11} decreases showing a better input match.

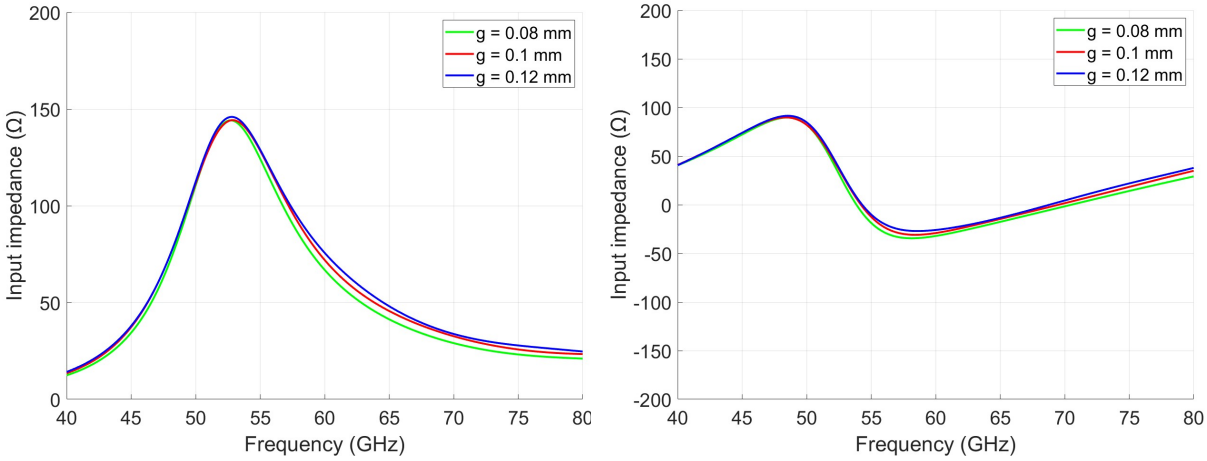

(a) Real Part. (b) Imaginary Part.

Figure 3.5: Impact of g on the input impedance of the FSA.

As for the s value, this parameter exhibits a behavior similar to that of the g parameter, although its impact is less pronounced. Increasing the s value results in minimal changes in impedance, as demonstrated in Figure 3.7a and Figure 3.7b. As for S_{11} in

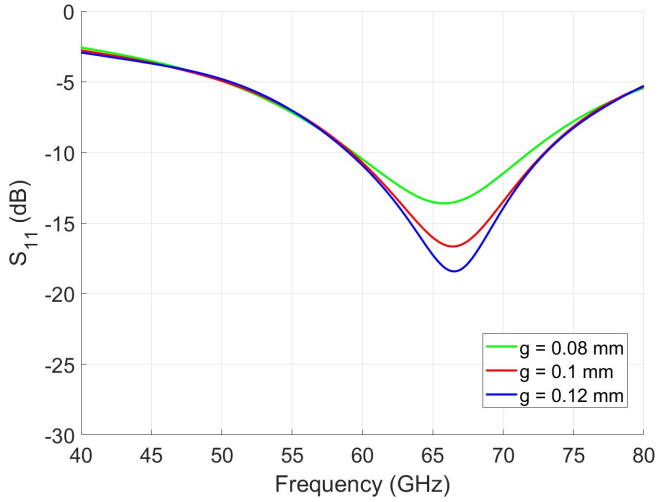

Figure 3.6: Impact of g on the S_{11} parameter of the FSA.

Figure 3.8, it shows a slight decrease.

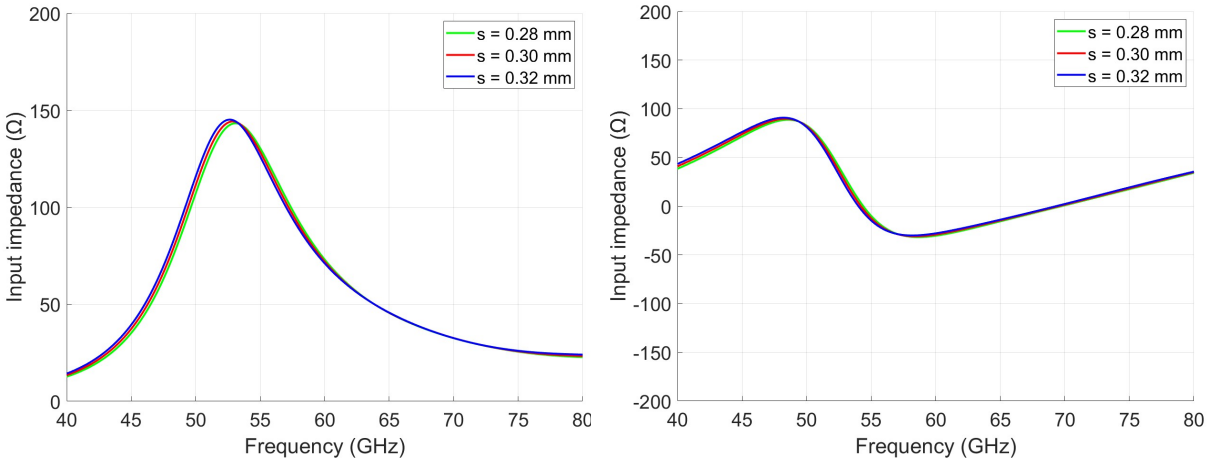

(a) Real Part. (b) Imaginary Part.

Figure 3.7: Impact of s on the input impedance of the FSA.

Since the purpose of this parametric study is to understand the impact of all the parameters regarding the FSA, variations in the dimensions of the copper surrounding the antenna were examined to assess their impact on antenna input impedance and input match. Starting with the length (Lg), the input impedance and input match can be observed in Figure 3.9 and Figure 3.10, respectively. By increasing the Lg the real and imaginary parts of the impedance become slightly more flattened as a result of increasing the Lg. By observing the frequencies around 60 GHz is visible that the variation is smaller for the higher value of the Lg (blue line) in the real and imaginary parts resulting in the increased bandwidth observed in the input match.

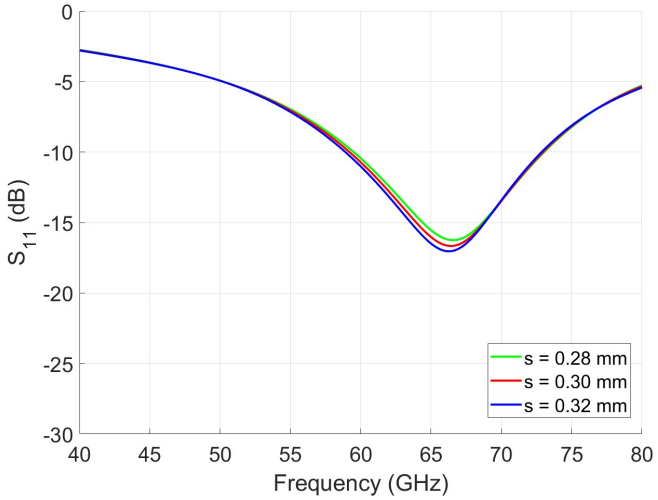

Figure 3.8: Impact of s on the S_{11} parameter of the FSA.

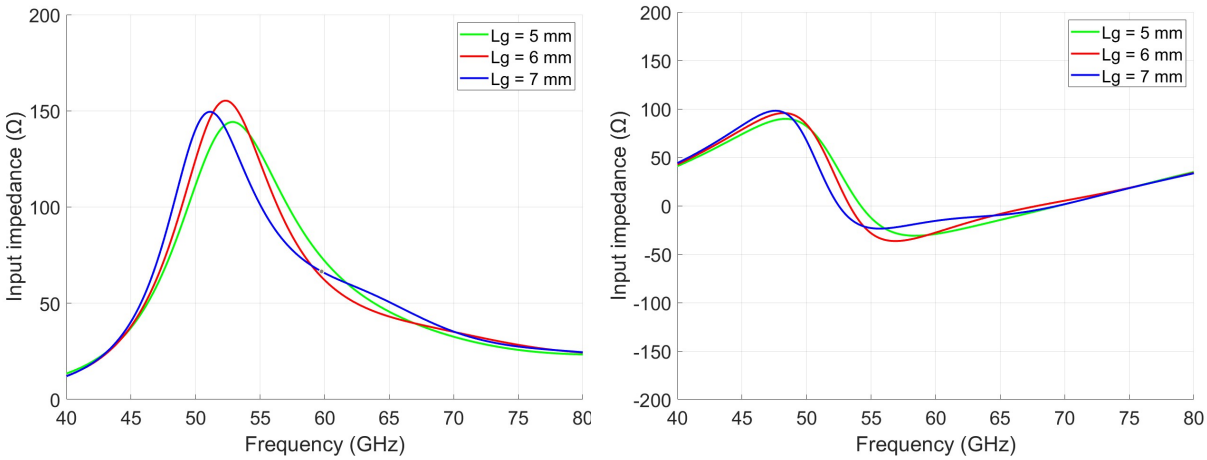

(a) Real Part. (b) Imaginary Part.

Figure 3.9: Impact of Lg on the impedance of the FSA.

As for the width (Wg), this parameter has a minor impact on the input impedance and input match visible in Figure 3.11 and Figure 3.12. By looking at the impedance, increasing the Wg results in a decrease in the peak values for the impedance just as the Lg. However, around 60 GHz, there is not much variation in the impedance's real and imaginary parts.

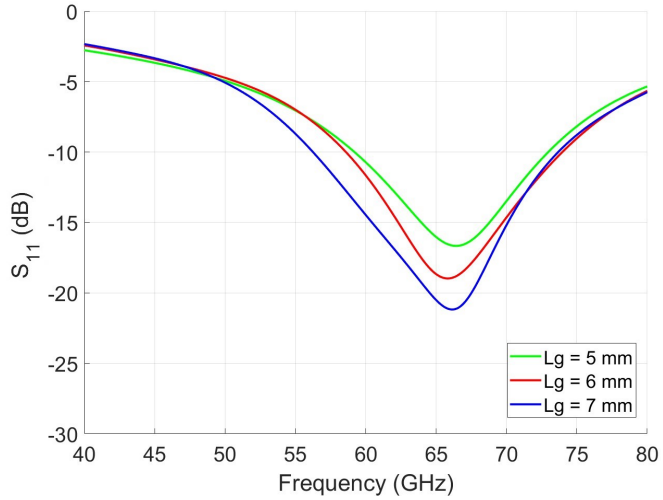

Figure 3.10: Impact of Lg on the S_{11} parameter of the FSA.

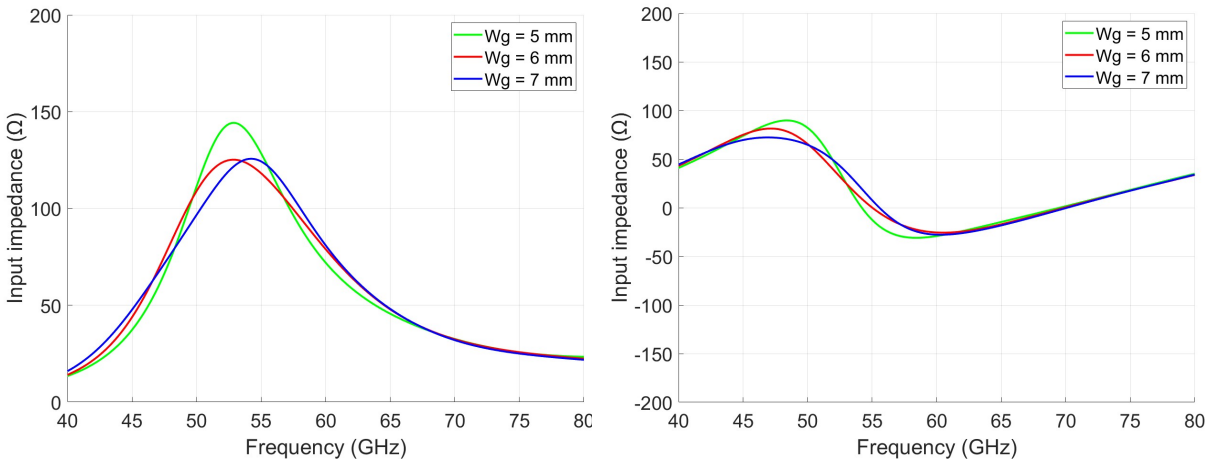

(a) Real Part.

(b) Imaginary Part.

Figure 3.11: Impact of Wg on the impedance of the FSA.

3.2.3 FSA design

Building upon the earlier parametric study, the dimensions of the antenna in an air environment were optimized. The specific dimensions are provided in Table 3.1 where it can be seen that for L parameter, the best value was slightly above the expected 0.5 λ and g and s are 0.05L and 0.11L, respectively. The input impedance is shown in Figure 3.13b and input match in Figure 3.13a. An impedance of approximately 49.4 Ω was obtained resulting in an excellent input match of −43.3 dB at 60 GHz.

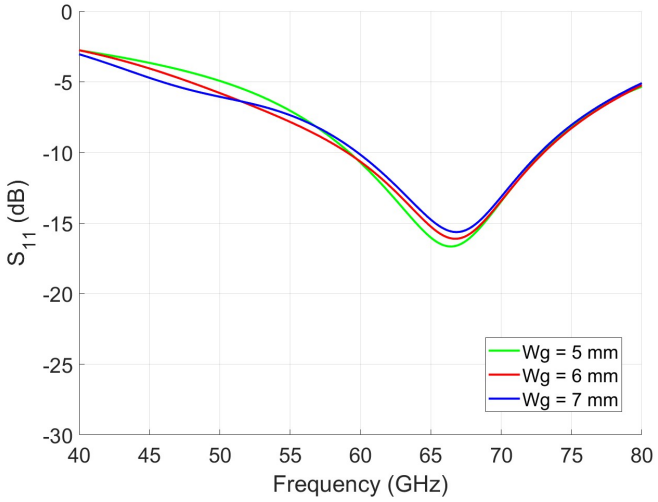

Figure 3.12: Impact of Wg on the S_{11} parameter of the FSA.

Table 3.1: Dimensions of the FSA in free space.

Parameters	L	g	s	Lg	Wg
Values (mm)	2.79	0.28	0.3	5	5
Values(λ)	0.558λ	0.056λ	0.06λ	λ	λ

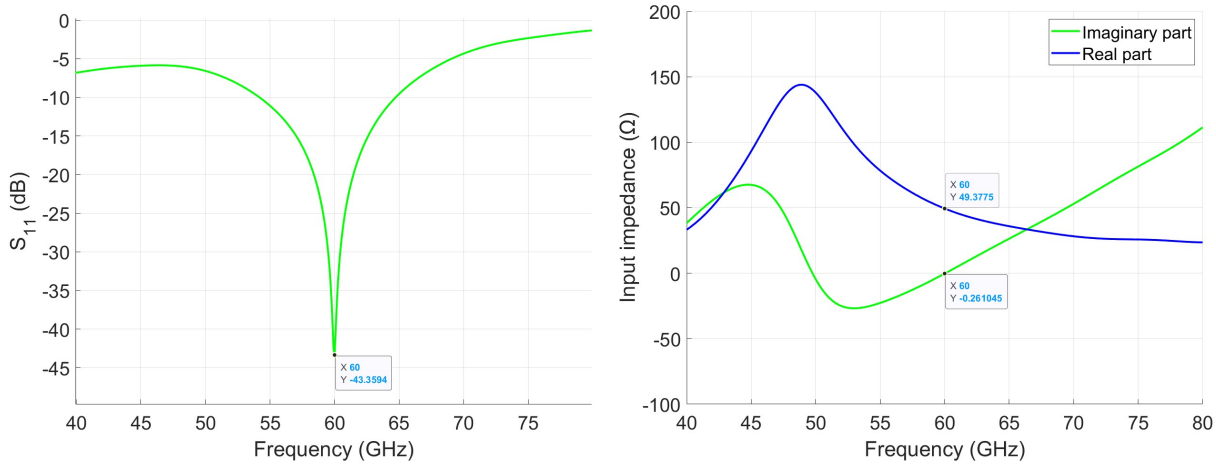

(a) S_{11}. (b) Impedance.

Figure 3.13: FSA free space optimization.

3.3 Printed Folded Slot Antenna (PFSA)

After studying the impact of each parameter relative to this structure, a substrate was introduced, with only the permittivity as the variable under investigation. Later the

impact of a ground plane will be evaluated.

3.3.1 permittivity Impact

Substrates with permittivities ranging from $\varepsilon_r = 3$ to $\varepsilon_r = 12$, each with a height of 250 µm and without losses were considered. According to the parametric study, the first theoretical design was considered. The input impedance is visible in Figure 3.14 and input match in Figure 3.15. Increasing the permittivity of the substrate leads to a decrease in the resonant frequency with the appearance of a new mode within the frequency range used.

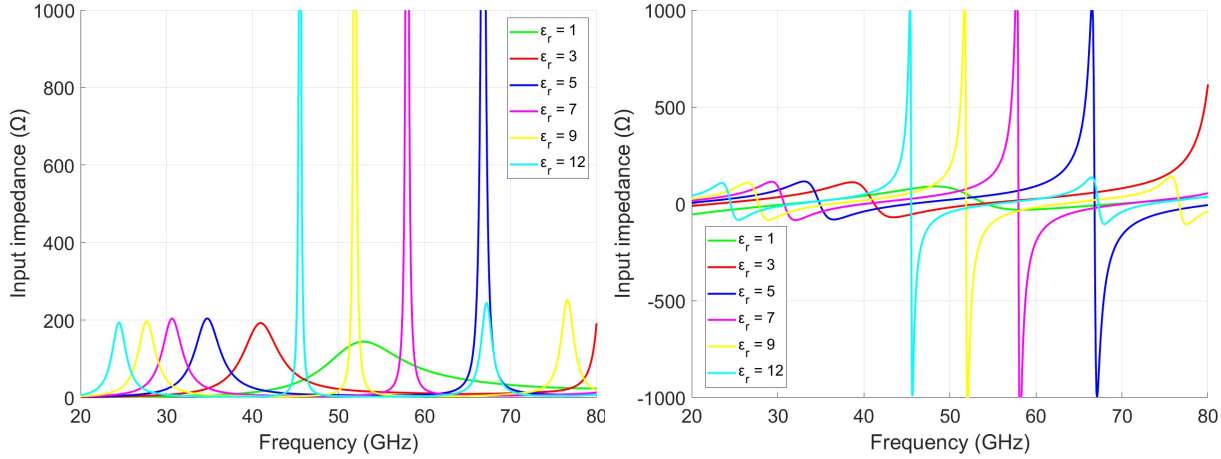

(a) Real Part. (b) Imaginary Part.

Figure 3.14: Impact of permittivity on the impedance of the PFSA.

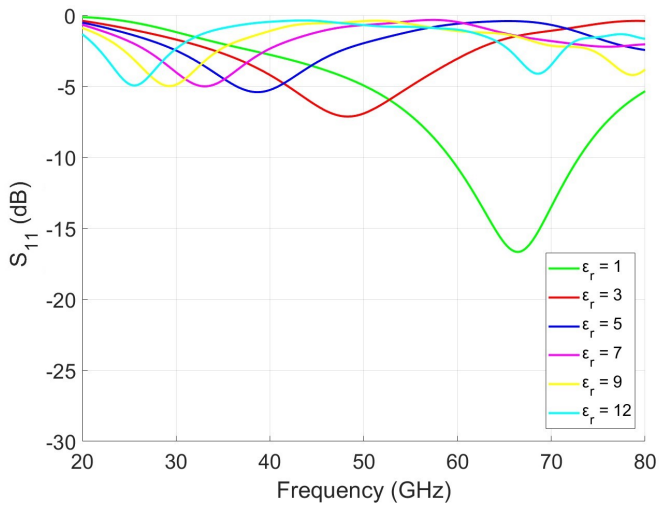

Figure 3.15: Impact of permittivity on the S_{11} parameter of the PFSA.

Six antennas were dimensioned with ε_r varying from 1-12 and respecting the Equation 3.1 for the different wavelengths (λ_d) respecting the permittivity of each dielectric. Respecting the method of characterization of the FSA where $g < s$ and $s \ll L$ it was not possible to get the S_{11}< -10 dB for antennas with high permittivity. So, using impedance as the primary criterion, we aimed to assess the influence of permittivity on the impedance. To achieve an imaginary part of the impedance equal to zero at 60 GHz, the antennas were adjusted. The real and imaginary parts of the impedance are displayed in Figure 3.16, demonstrating that as the permittivity increases, the real part of the impedance is affected drastically decreasing for the same mode of operation. The specific dimensions are provided in Table 3.2 along with the values of the real part of the impedance where λ_0 represents the free space wavelength.

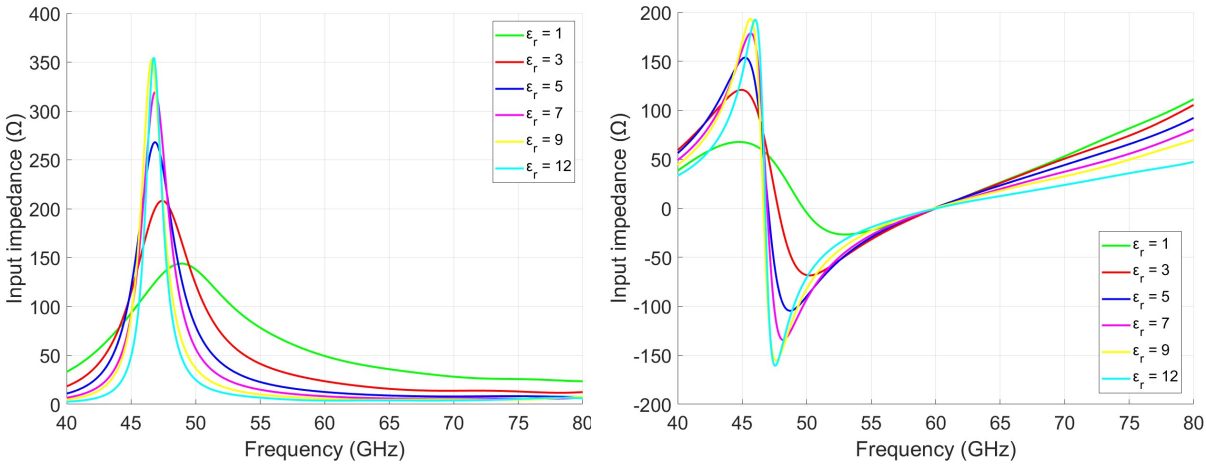

(a) Real part. (b) Imaginary Part.

Figure 3.16: Impedance with different permittivities of the PFSA.

Table 3.2: PFSA dimensions and impedance for different permittivities.

Parameter	L(g=0.05xL / s=0.11xL)					
ε_r	1	3	5	7	9	12
Value (mm)	2.79	2.15	1.79	1.54	1.37	1.17
Value(λ_0)	0.558	0.43	0.358	0.308	0.274	0.234
Value(λ_d)	-	0.746	0.803	0.814	0.820	0.812
Imp(Real Part)(Ω)	49.37	23.59	12.53	8.14	5.72	3.73

We also observed the normalized 2D radiation pattern for $\varepsilon_r = 1$ and $\varepsilon_r = 12$ at 60 GHz in the $\phi = 90°$ and $\phi = 0°$ planes. Figures 3.17a and 3.17b illustrate the radiation pattern for the antenna with a low substrate ($\varepsilon_r = 1$). The antenna exhibits a main lobe

magnitude at $\theta = 0°$ and at $\theta = 180°$, with a maximum gain of 5.52 dBi. However, as the permittivity increases, the radiation pattern loses its symmetry and begins to radiate into the substrate.

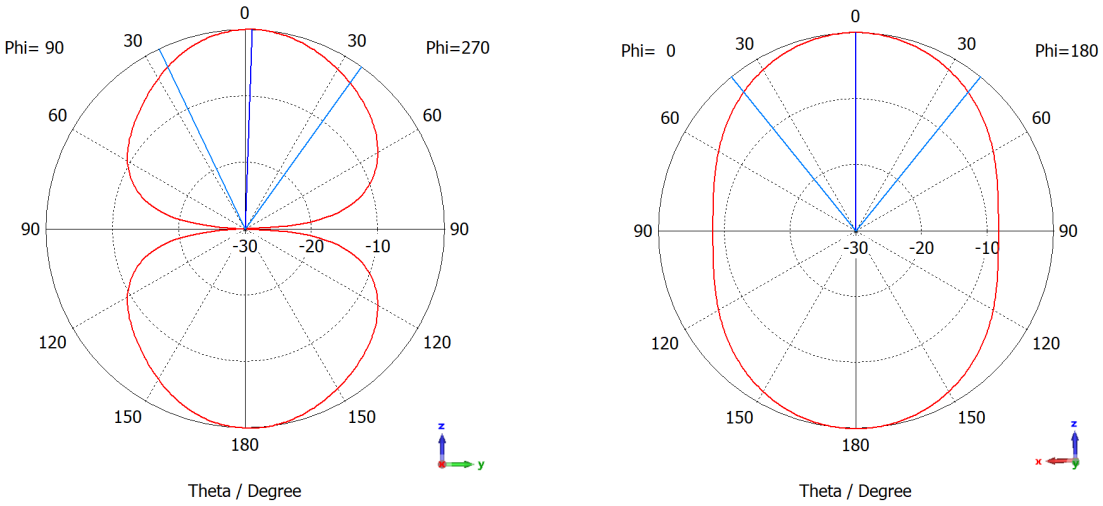

(a) $\phi = 90°$. (b) $\phi = 0°$.

Figure 3.17: $\varepsilon_r = 1$ impact in the radiation pattern.

In Figures 3.18a and 3.18b, the normalized radiation pattern of the antenna on a substrate with $\varepsilon_r = 12$ is observed. The maximum lobe magnitude is at $\theta = 180°$ with a gain of 4.94 dBi, while for $\theta = 0°$, the gain is 1.43 dBi. This behavior becomes more pronounced as the permittivity increases, causing most of the radiated power to be confined in the substrate rather than being radiated into free space, highlighting one of the anticipated issues discussed in Chapter 2.

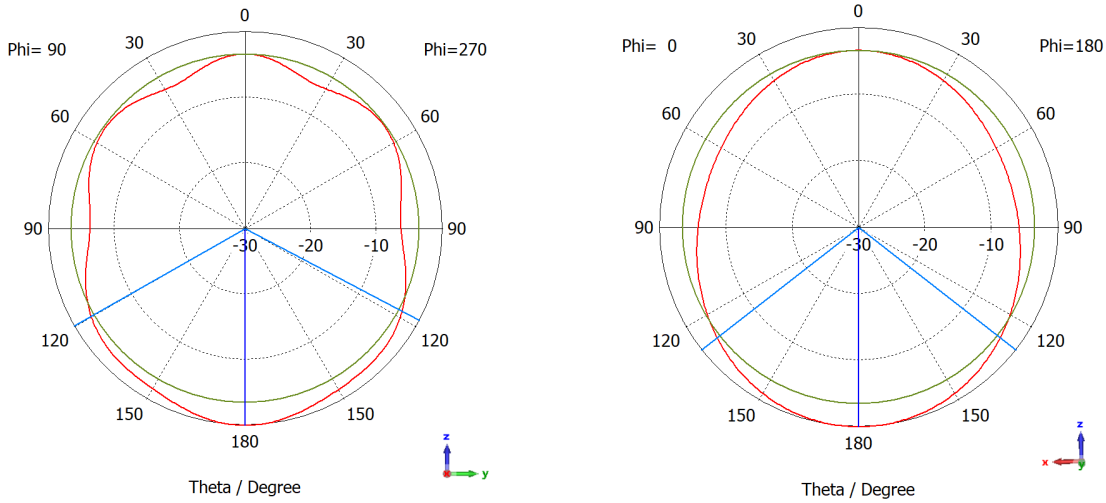

(a) $\phi = 90°$. (b) $\phi = 0°$.

Figure 3.18: $\varepsilon_r = 12$ impact on the normalized radiation pattern.

3.3.2 PFSA with Ground plane

One potential solution to address this issue is introducing a ground plane into the structure. The use of a ground plane effectively reflects the radiation, redirecting any radiation traveling toward the substrate and keeping it in the region above the ground plane.

Beginning with the structure without dielectric material, a study was conducted on the impact of a floating ground plane at various distances ranging from 0.1λ to 0.5λ (0.5 mm to 2.5 mm). The goal was to optimize all structures to achieve at least S_{11} < -10 dB, as shown in Figure 3.19. It is also visible that, as the ground plane is closer to the antenna, the bandwidth is bigger.

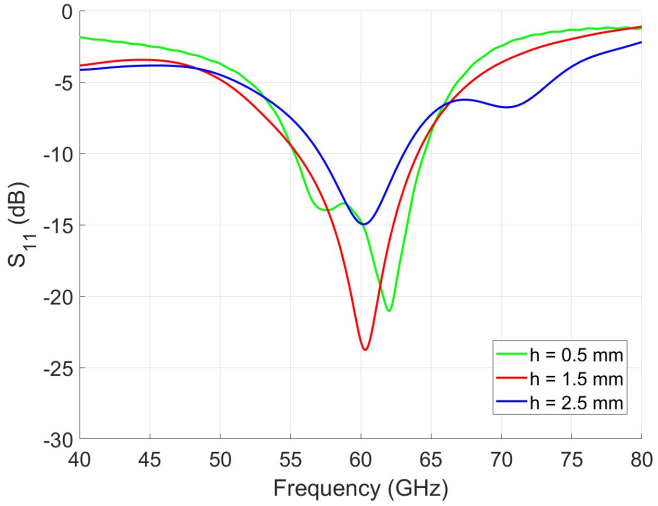

Figure 3.19: Distance of the ground plane impact on the S_{11} of the FSA.

The normalized radiation pattern for the different distances is presented in Figure 3.20, revealing that a significant portion of the radiation is concentrated in the desired direction of 0°, in contrast to Figure 3.17a. Furthermore, a comparison of the various distances shows that, as the distance between the antenna and the ground plane decreases, the main lobe direction shifts towards the intended direction of $\theta = 0°$, and the angular width (3 dB) decreases.

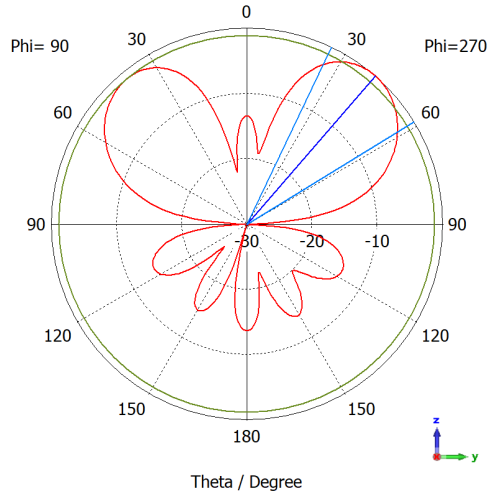

(a) Distance 2.5 mm.

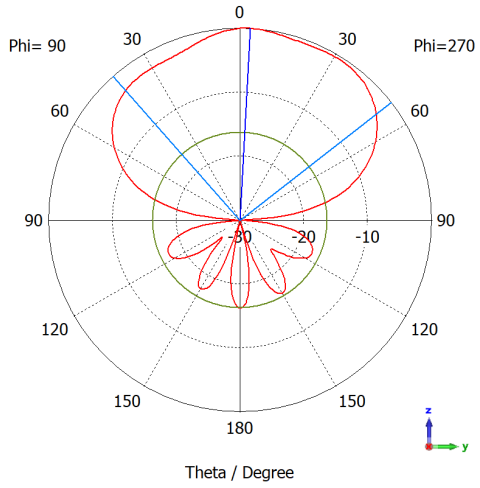

(b) Distance 1.5 mm.

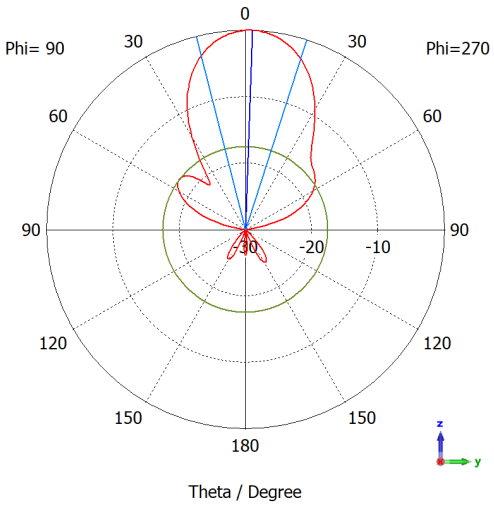

(c) Distance 0.5 mm.

Figure 3.20: Distance of the ground plane impact on the normalized radiation pattern.

A similar analysis was conducted for a substrate with a permittivity of 12, but this time considering distances ranging from 0.1 λ_d to 0.3 λ_d (0.14 mm to 0.43 mm). When examining the S_{11}, shown in Figure 3.21, it becomes evident that additional modes begin to operate in the presence of the ground plane. This observation suggests that the structure is now behaving similarly to a resonant cavity. Since the permittivity of the dielectric is very big the waves are reflected and bounce back and forth between the walls of the cavity.

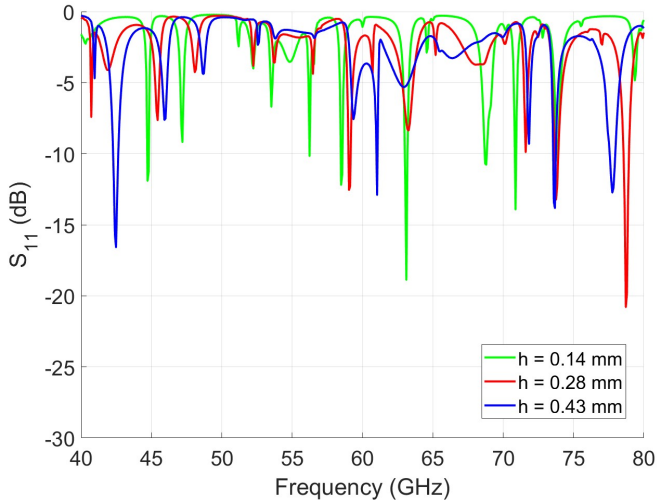

Figure 3.21: S_{11} parameter for different distances of the ground plane with a substrate of $\varepsilon_r = 12$.

Using Equation 3.2, it is possible to calculate the frequencies for different modes of operation denoted by m, n, and p. This calculation takes into account the dimensions of the structure, as illustrated in Figure 3.22 [8]. In this scenario, it is not the antenna dimensions that influence the behavior, but rather the dimensions of the structure, including its width (Wg), length (Lg), and thickness (h).

$$f_{r_{mnp}} = \frac{c}{2 \times \sqrt{\varepsilon_r}} \times \sqrt{\left(\frac{m}{h}\right)^2 + \left(\frac{n}{L}\right)^2 + \left(\frac{p}{W}\right)^2} \tag{3.2}$$

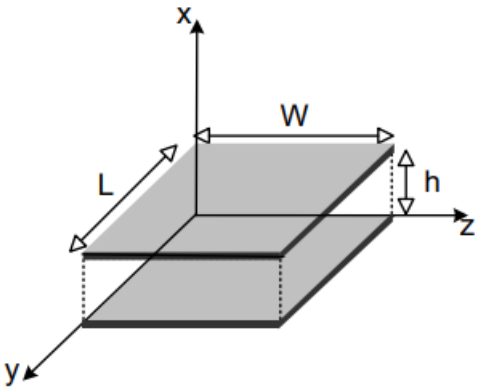

Figure 3.22: Cavity structure.

After adjusting the parameters to achieve a resonant frequency of 60 GHz including the height of the substrate used of 250 μm, we observed the S_{11} in Figure 3.23 and the electric fields shown in Figure 3.24. It was possible to achieve a S_{11} of -21.75 dB,

as for the electric field it reveals that the antenna is not operating in its fundamental mode (first mode of operation). Although it is not possible to conclude the antenna's operating mode, a standing wave pattern is visible in the electric field along the length and width of the structure, which has a resonant behavior.

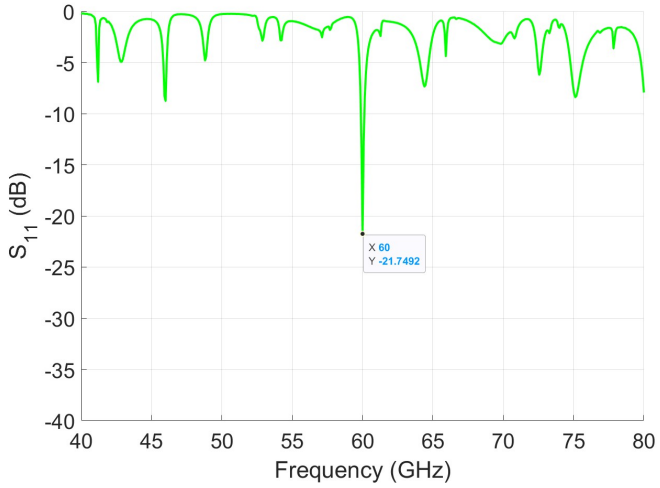

Figure 3.23: S_{11} of the PFSA without losses of the InP.

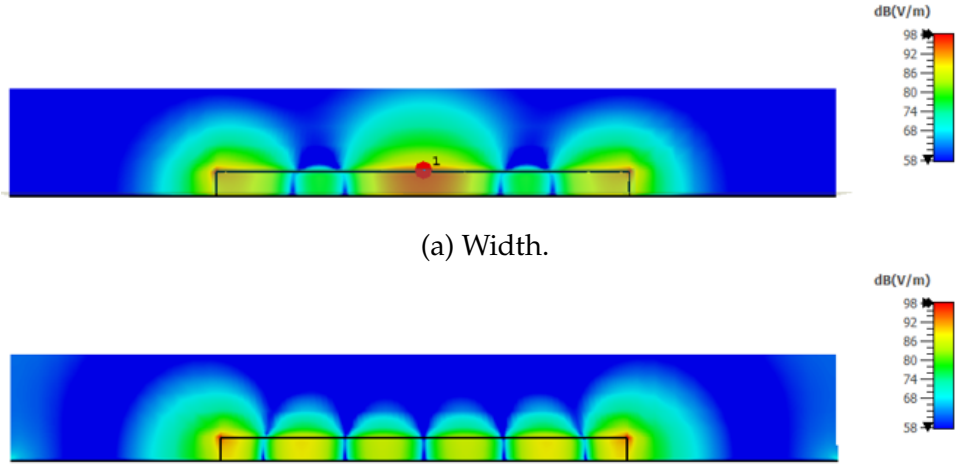

(a) Width.

(b) Length.

Figure 3.24: Electric field distribution.

3.3.3 FPSA design

After adjusting the structural parameters to achieve resonance at 60 GHz, we incorporated the remaining InP characteristics into the simulation, using the values provided in Table 3.3. Figure 3.25 illustrates the impact of InP losses on the input match which reveals that introducing the losses of the substrate lowers the S_{11}.

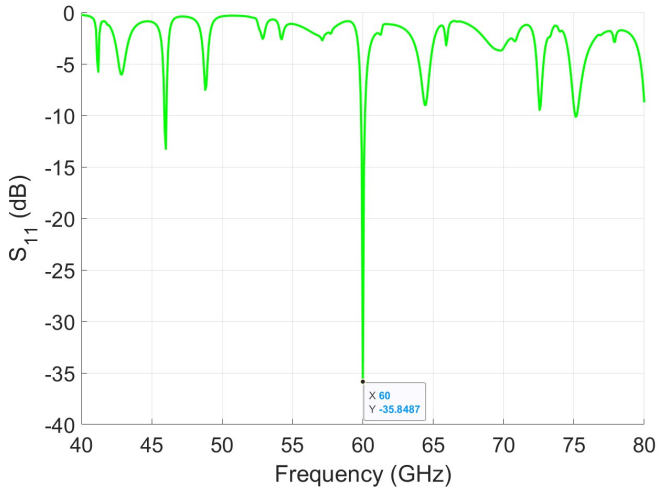

Figure 3.25: S_{11} of the PFSA with losses of the InP.

Table 3.3: InP characteristics

Parameters	Value
Permetivitty	12.4
Height	0.250 mm
Loss tan	0.0012

After incorporating the InP losses, we introduced the CPW to the antenna. The final antenna dimensions are summarized in Table 3.4 and the design is illustrated in Figure 3.26. The ground plane is bigger to understand the impact of a bigger conductive plate since the antenna can be put in a structure such as a PCB. To achieve a 50 Ω CPW line, it was necessary to dimension the center conductor (*Wc*) and the gap (*gap*) between this line and the side ground planes. Using the macro tool from CST, the values for *Wc* and *gap* required to obtain a 50 Ω line were determined as *Wc* = 0.028 mm and *gap* = 0.0187 mm. Figure 3.27 displays the S_{11} with the CPW included, where we were able to achieve S_{11} of -26.43 dB.

Table 3.4: PFSA final dimensions.

Parameters	L	g	s	Lg	Wg
Values (mm)	1	0.1	0.11	4.85	4.81

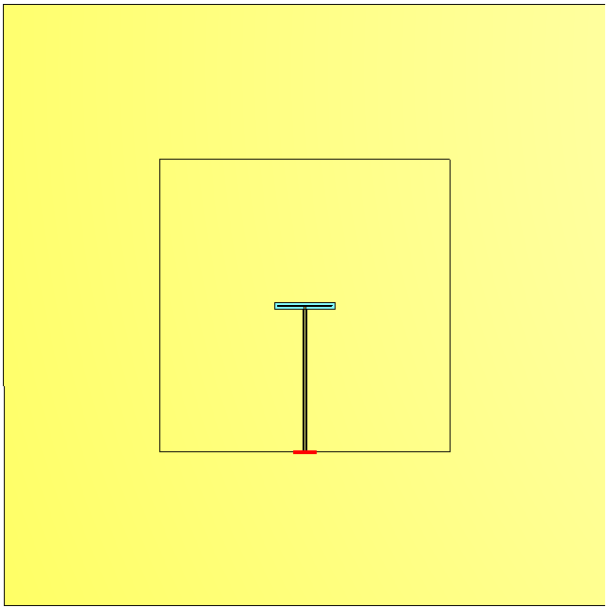

Figure 3.26: FSA final design.

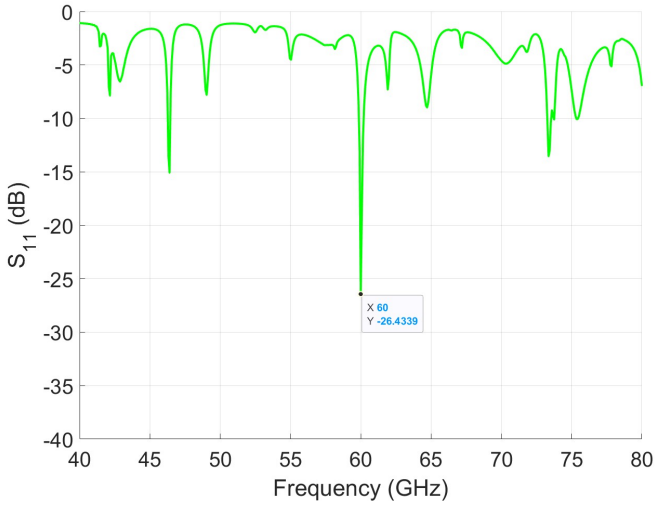

Figure 3.27: S_{11} of the PFSA with CPW.

The radiation pattern was also observed, as depicted in Figure 3.28. This design allowed us to achieve a directive radiation pattern with an angular width of 25.3° and 46.8° in the $\phi = 90°$ and $\phi = 0°$ planes, respectively. Details regarding the gain, efficiency, and bandwidth are provided in Table 3.5.

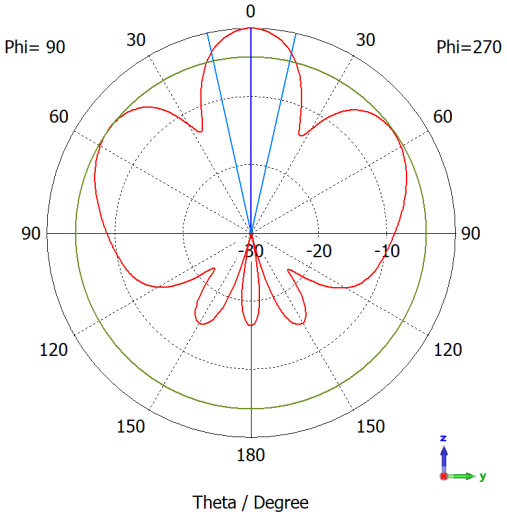

(a) $\phi = 90°$.

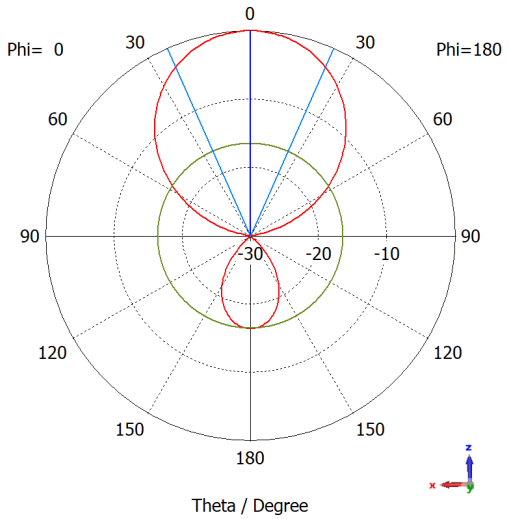

(b) $\phi = 0°$.

Figure 3.28: Normalized radiation pattern of the final design of the PFSA.

Table 3.5: PFSA overall performance.

Parameters	Value
S_{11}	-26.43 dB
Gain	8.5 dBi
Efficiency	51%
Bandwidth	314 MHz

In conclusion, this study has demonstrated the feasibility of operating at 60 GHz with an InP substrate using this structure. However, it is important to note that while the investigation began with a folded slot antenna, the behavior of the structure eventually resembled a resonant cavity. Consequently, it is difficult to attribute the radiation solely to one of these options, not both. Thus, this chapter concludes with the design that has achieved a directive radiation pattern but also leaves open the possibility of further exploring the microstrip antenna as a potential solution.

4

Rectangular Microstrip Antenna

In this chapter, we delve into the study of the microstrip patch antenna. In the preceding chapter, we examined the FSA, and as we introduced the ground plane to achieve a directive radiation pattern, the antenna began to exhibit characteristics resembling those of a resonant cavity, much like the microstrip patch antenna. Therefore, in this chapter, we analyze this structure as one of the potential designs for constructing on-chip antennas for both InP and silicon substrates.

4.1 Microstrip Design

When designing a microstrip patch antenna, several parameters need to be calculated to ensure the antenna operates at the desired working frequency. The goal is to achieve the best possible input match, which means that the parameter S_{11} ideally approaches negative infinity at the frequency of 60 GHz. This implies that the reflection at the entrance of the patch is nearly zero, allowing the entire signal to be radiated.

We begin by calculating the width (W) of the patch, as expressed by Equation (4.1), where c represents the speed of light, f_r denotes the resonant frequency, and ε_r represents the dielectric constant of the substrate material [8].

$$W = \frac{c}{2 \times f_r \times \sqrt{\frac{\varepsilon_r + 1}{2}}} \tag{4.1}$$

Ideally, in microstrip antennas, the electric field lines between the patch and the ground plane predominantly travel through the substrate. However, at the boundaries of the patch, due to its finite size, these electromagnetic waves simultaneously pass through the air and the substrate, giving rise to what is known as the fringe effect, as depicted in Figure 4.1.

To address this effect, it becomes necessary to treat both the air and the substrate as a single medium, homogenizing the permittivities of these layers. This is achieved using the parameter ε_{ref}, as defined in Equation (4.2), with the condition $W/h > 1$, where h represents the height of the substrate. This approach aims to prioritize radiation over transmission.

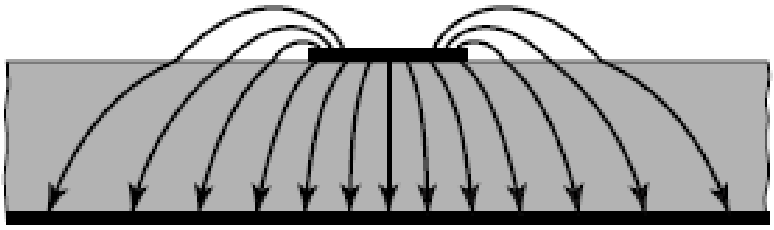

Figure 4.1: Fringe effect [8].

$$\varepsilon_{ref} = \frac{\varepsilon_r + 1}{2} + \frac{\varepsilon_r - 1}{2} \times \left(1 + 12 \times \frac{h}{W}\right)^{-\frac{1}{2}}, \qquad \text{para } \frac{W}{h} > 1 \tag{4.2}$$

When treating the air and dielectric as a single medium with ε_{ref}, the effective length of the patch (L_{eff}) is determined by Equation (4.3) [8].

$$L_{eff} = \frac{c}{2 \times f_r \times \sqrt{\varepsilon_{ref}}} \tag{4.3}$$

Because of the fringe effect, the electric field lines at the edges of the patch exhibit a curved pattern, making it appear as if the patch has larger dimensions than its actual physical dimensions. To account for this effect and remove the contribution to the effective length, we calculate the excess length (ΔL) using Equation (4.4) [8].

$$\Delta L = 0.412h \times \frac{(\varepsilon_{ref} + 0.3) \times (\frac{W}{h} + 0.264)}{(\varepsilon_{ref} - 0.258) \times (\frac{W}{h} + 0.8)} \tag{4.4}$$

Since this effect appears on both sides of the width of the *patch*, these two contributions will have to be removed, and we then conclude that the length of the *patch* will be given by the equation (4.5).

$$L = L_{eff} - 2 \times \Delta L \tag{4.5}$$

Patch impedance

The radiating element exhibits varying input impedances at different feed locations. Specifically, the maximum impedances are found at the ends of the patch, while the minimum impedances occur at a distance of $\lambda/4$ from the ends. This consideration takes into account that $L \approx \lambda/2$, where λ represents the wavelength on the substrate.

According to Constantine A. Balanis [8], the input impedance at the patch (Z_{in}) can be estimated using Equation (4.6), where λ_0 denotes the wavelength under vacuum conditions.

$$Z_{in} = \frac{60 \times \lambda_0}{W} \tag{4.6}$$

In order to optimize the antenna, the input impedance Z_{in} of the radiating element must match the characteristic impedance (Z_o) of the transmission line that feeds it. In this way, the transmission line must be inserted at a given position on the radiating element, in such a way that the impedances are as close as possible.

4.2 Microstrip antenna on InP substrate

After calculating the antenna dimensions to achieve the first resonant frequency at 60 GHz, we proceeded to build the antenna in CST on an InP substrate. The first value for the length and width of the patch used was 0.72 mm. The antenna geometry and S_{11} are shown in Figure 4.2 where it is evident that the resonant frequency falls below the intended 60 GHz.

4.2.1 Parametric study

To gain a better understanding of how the antenna parameters influence its performance, a parametric study was conducted, varying the patch length and width, the

feed point position, and the dimensions of the substrate and the ground plane.

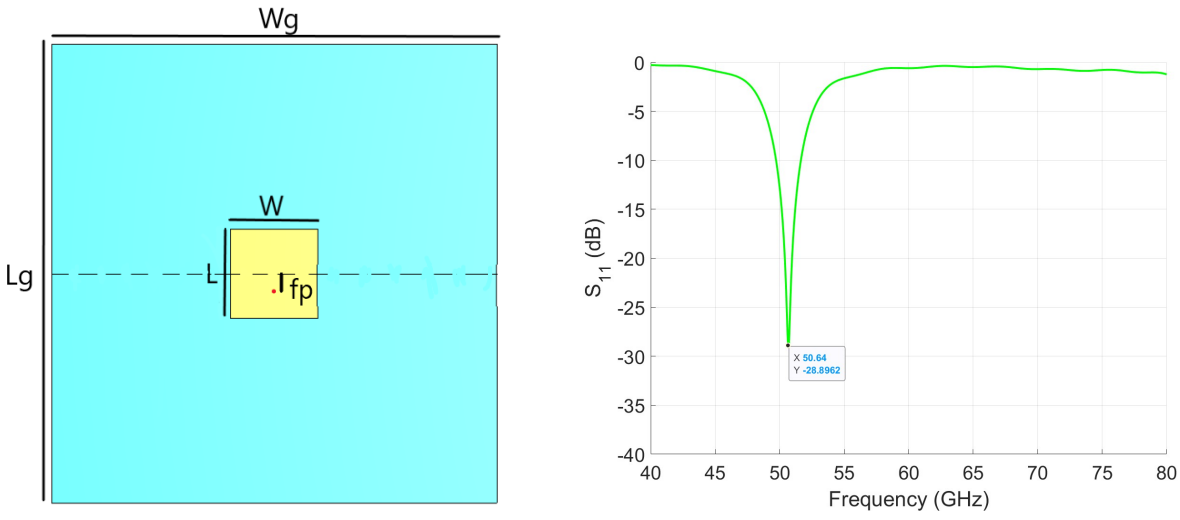

(a) Microstrip structure. (b) S_{11}.

Figure 4.2: Microstrip S_{11} and structure with L = 0.72 mm, W = 0.72 mm, FP = -0.2 mm, Wg = 3 mm and Lg = 3 mm.

We initiated the study with a parametric exploration of the L parameter, varying it by ±0.1 mm from its initially calculated value of 0.72 mm. The input impedance is shown in Figure 4.3 and S_{11} in Figure 4.4. As it can be seen, the L parameter significantly influences the resonant frequency. Increasing the length of the patch leads to a decrease in the resonant frequency, and vice versa. It is also visible that decreasing the length of the patch increases the peak values of both the real and imaginary parts of the impedance.

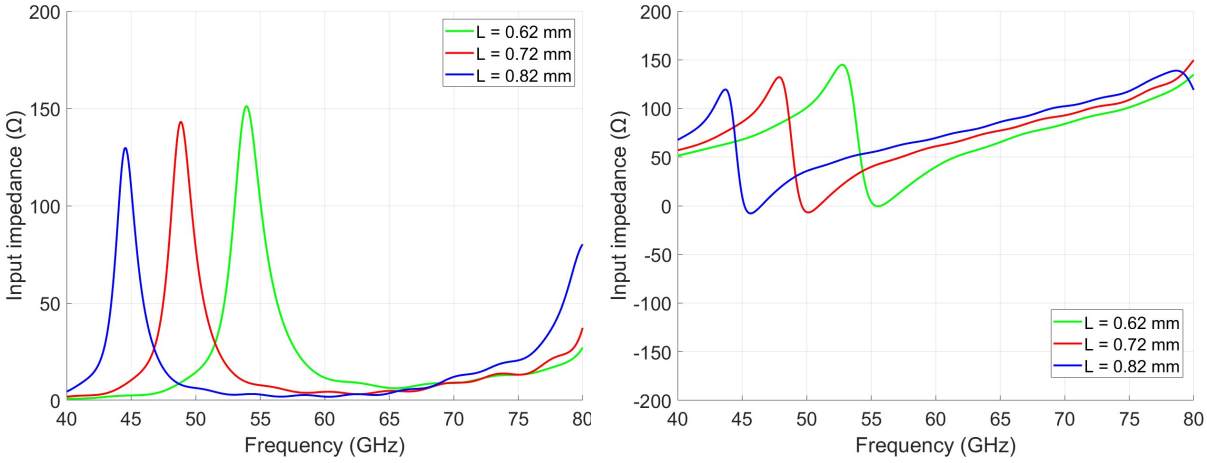

(a) Real Part. (b) Imaginary Part.

Figure 4.3: Impact of L on the input impedance of the Microstrip antenna.

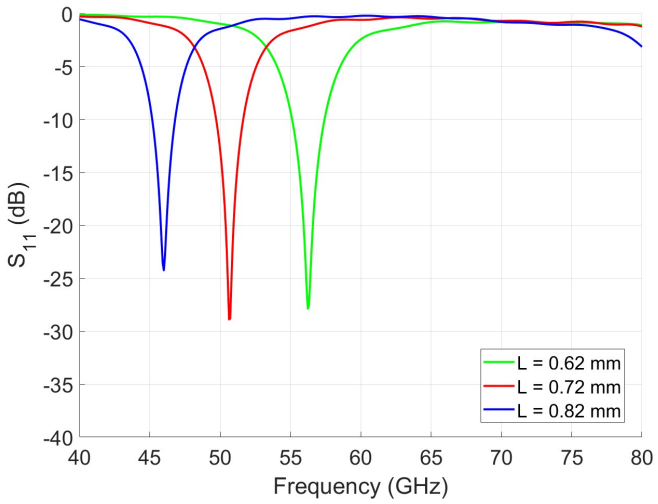

Figure 4.4: Impact of L on the S_{11} parameter of the Microstrip antenna.

The same variation was made for the width (W) of the patch. Looking at input impedance in Figure 4.5 and S_{11} present in Figure 4.6 there is a slight decrease of the resonant frequency with the increase of the W. It is also visible that, by increasing the value of the W the peak values of the real and imaginary parts of the impedance decrease.

The feed point is a crucial parameter in the patch antenna structure, as its location should be as close as possible to the 50 Ω impedance point on the patch to define the antenna's input impedance. To achieve a better match between the patch impedance and the port impedance, the port location must align with the antenna's input impedance.

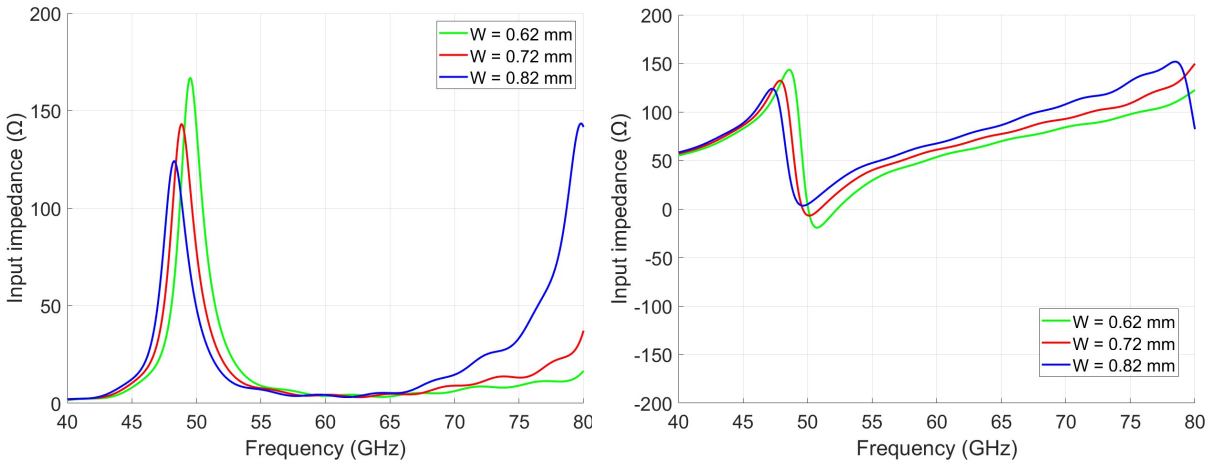

(a) Real Part. (b) Imaginary Part.

Figure 4.5: Impact of W on the input impedance of the microstrip antenna.

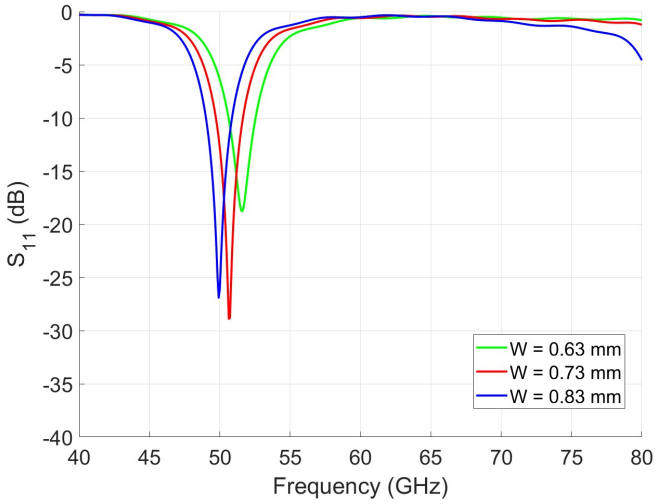

Figure 4.6: Impact of W on the S_{11} parameter of the microstrip antenna.

As explained earlier, the patch exhibits varying impedances depending on the port's placement. To achieve an improved input match, we varied the port's location by ±0.05 mm from its original position. Figure 4.7 illustrates the different outcomes when lowering the feed point from the center of the patch in the input impedance and Figure 4.8 in the input match. By lowering the feed point position, the variation of the real and imaginary parts of the impedance increase. At approximately 50.5 GHz, the impedance closely approaches 50 Ω, resulting in the best input match, accentuated for the *fp* value of -0.20 mm below the center of the patch (red curve).

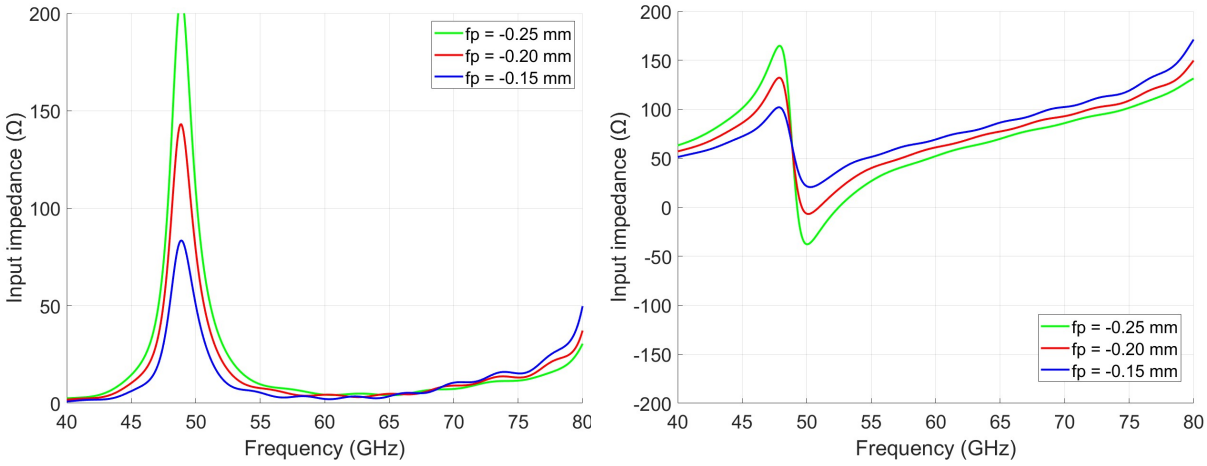

(a) Real Part. (b) Imaginary Part.

Figure 4.7: Impact of *fp* on the input impedance of the microstrip antenna.

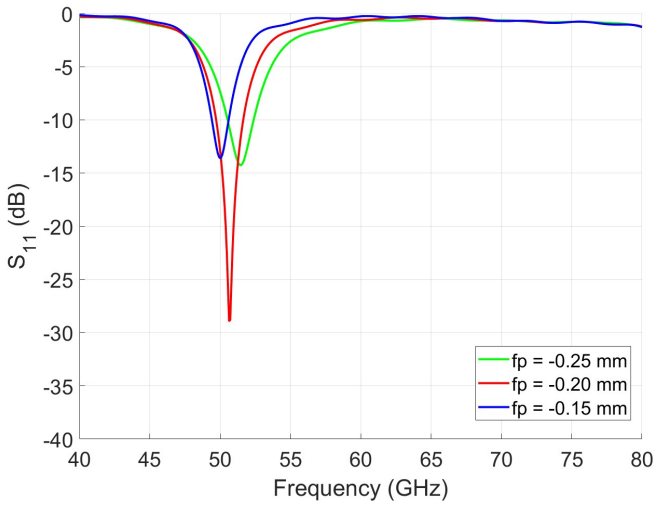

Figure 4.8: Impact of *fp* on the S_{11} parameter of the microstrip antenna.

We also explored the impact of altering the dimensions of the substrate and ground plane to assess their influence on the antenna input match. Starting with the width of the substrate and ground plane (*Wg*), the input impedance and input match are visible in Figure 4.9 and Figure 4.10, respectively. The variation of this parameter had a slight impact on the S_{11} which improved with the decrease of the *Wg*. By observing the impedance, both real and imaginary parts of the impedance slightly change especially around 50 GHz.

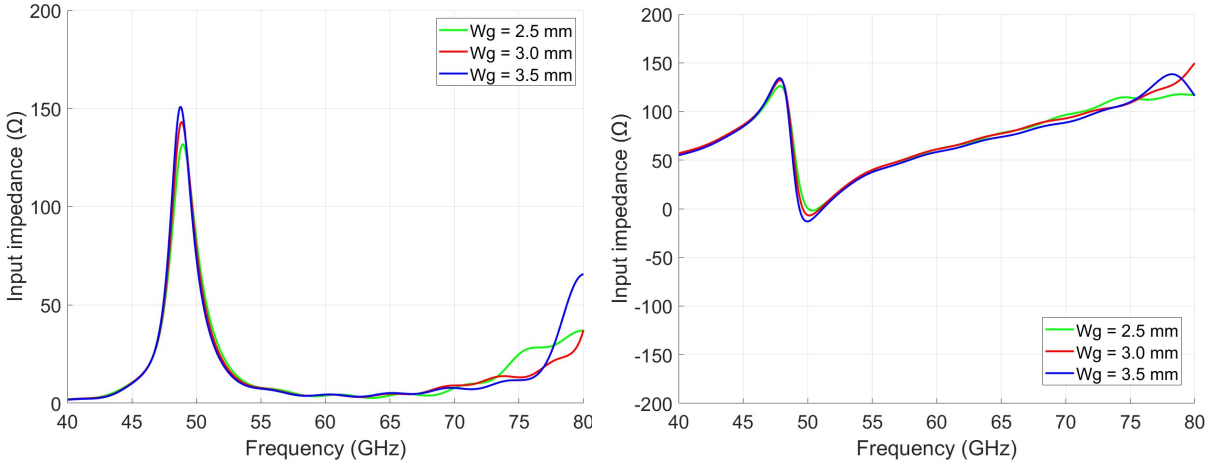

(a) Real Part. (b) Imaginary Part.

Figure 4.9: Impact of *Wg* on the input impedance of the microstrip antenna.

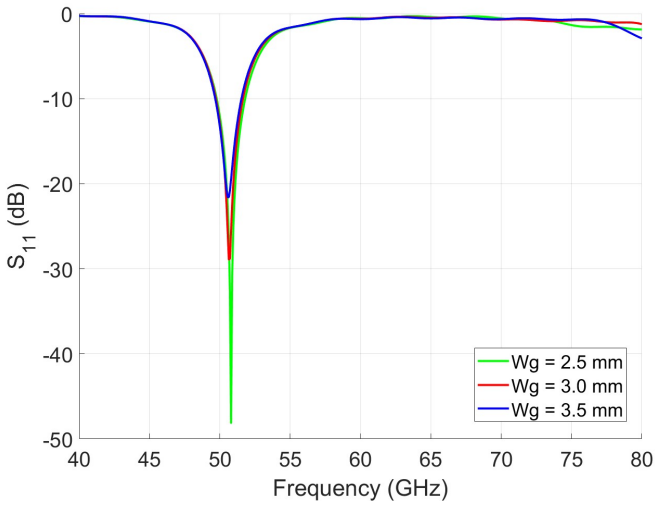

Figure 4.10: Impact of Wg on the S_{11} parameter of the microstrip antenna.

By looking at the variation in the length of the substrate and ground plane Lg, we observe that this parameter has a similar impact to the Wg. By looking at the impedance in Figure 4.11, both real and imaginary parts of the impedance slightly change in a similar way to the Wg, making the S_{11} more accentuated with the decrease of this value observed in Figure 4.12.

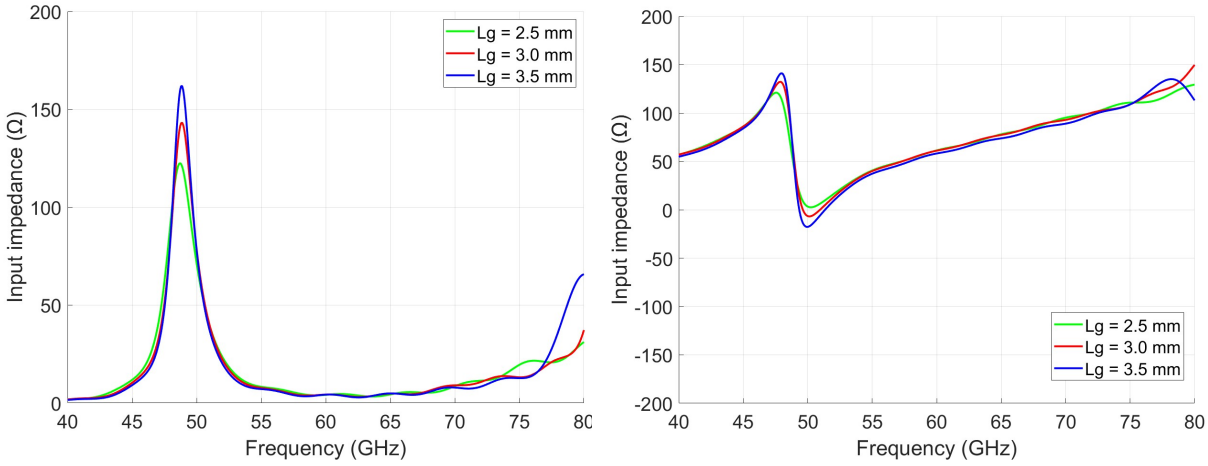

(a) Real Part. (b) Imaginary Part.

Figure 4.11: Impact of Lg on the input impedance of the microstrip antenna.

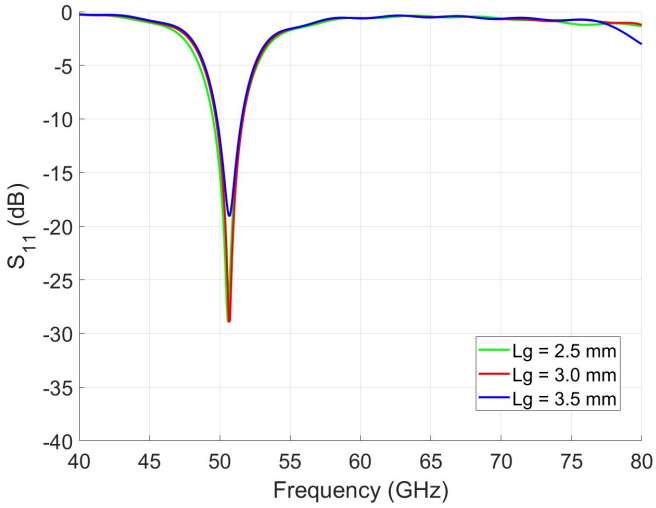

Figure 4.12: Impact of Lg on the S_{11} parameter of the microstrip antenna.

Notably, both the length and width of these elements demonstrated similar effects on antenna performance. Increasing the length and width of the substrate and ground plane led to an increase in the peak values of both the real and imaginary parts of the impedance. However, it is important to note that these changes had a less significant impact compared to the adjustments made to the previous parameters.

So, to increase the resonant frequency, the length of the patch was decreased until the S_{11} obtained in Figure 4.13 of ≈ -30 dB. The final L and W dimensions are 0.574 mm and 0.56 mm, respectively and fp of -0.18 mm.

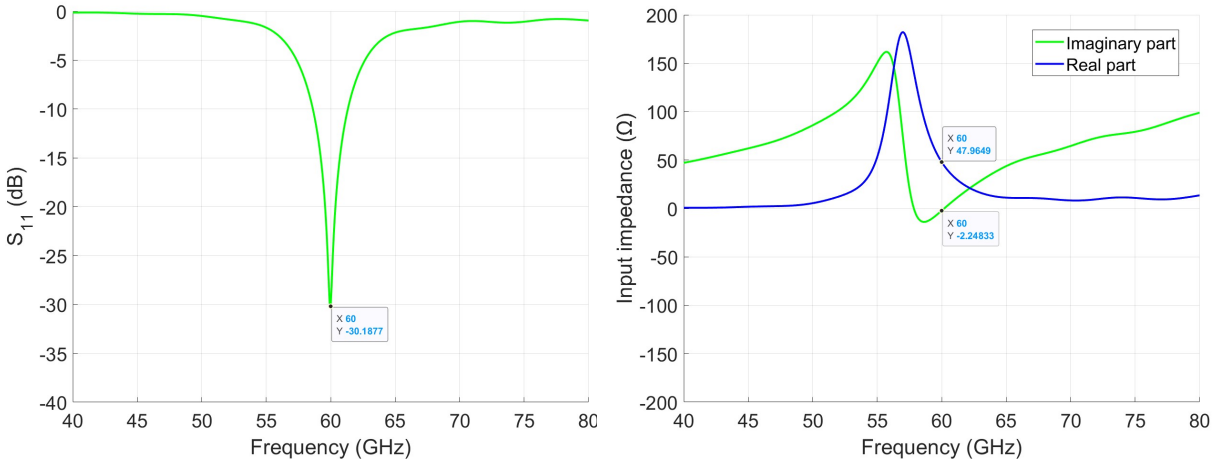

(a) S_{11} (b) Impedance Real Part.

Figure 4.13: Microstrip optimization with discrete port.

As the antenna is intended for integration within an integrated circuit, it is crucial to

consider the dimensions of the chip. For this purpose, we adopted the dimensions of the InP substrate to match the HHI product ID HHI-4-2-8, measuring 2x8 mm² [53]. Additionally, one possibility is to put the chip on top of a PCB, so the dimensions of the ground plane were expanded to understand the impact of having a larger ground plane in the antenna performance. The antenna S_{11} is visible in Figure 4.14. These adjustments in the dimensions of the InP substrate and the ground plane had a small effect on the antenna's resonant frequency. The S_{11} parameter increased from -30 dB to -25 dB.

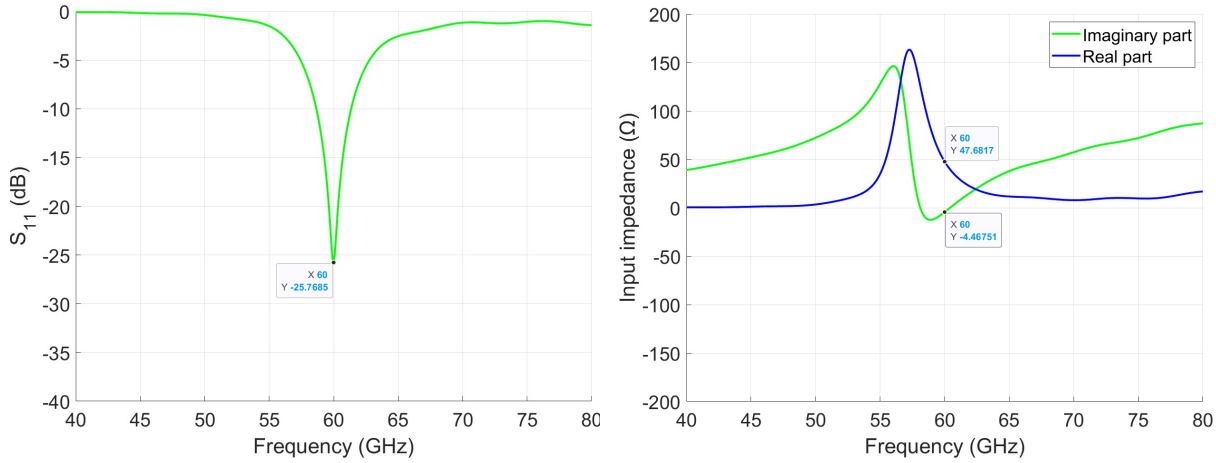

(a) S_{11} (b) Impedance Real Part.

Figure 4.14: Microstrip optimization with discrete port considering dimensions of product HHI-4-2-8.

4.2.2 Inset Feed

Since the CPW is the feeding method used, we opted for the inset feed technique, as illustrated in Figure 4.15. This choice facilitates a direct connection between the 50 Ω CPW line and the 50 Ω point on the antenna. To comprehend this technique thoroughly, we conducted a parametric study.

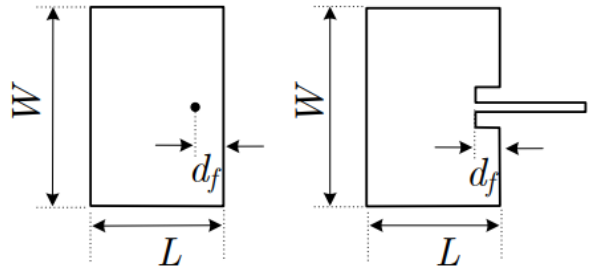

Figure 4.15: Impedance point demonstration in inset feed.

First, let's explore all the relevant parameters associated with this type of feeding technique using CPW. Figure 4.16 illustrates the inset feed and the key parameters involved: *sl* (length of the inset), *sx* (the width of the inset), and the variable *aux* (representing the spacing between the patch and CPW).

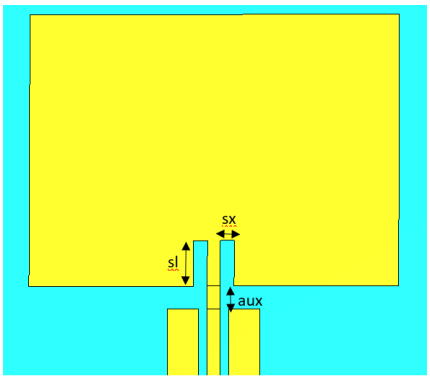

Figure 4.16: Inset feed representation on the antenna.

The first parameter under investigation is denoted as *sl*. This parameter was varied within the range of 0.15 mm to 0.05 mm. Figure 4.17 shows the input impedance and Figure 4.18 the input match. As can be seen, this parameter exerts an influence on the resonant frequency, with the frequency decreasing as this variable increases. It is also visible the appearance of another mode of operation. As for the impedance the peak value of the real part increases as the *sl* decreases.

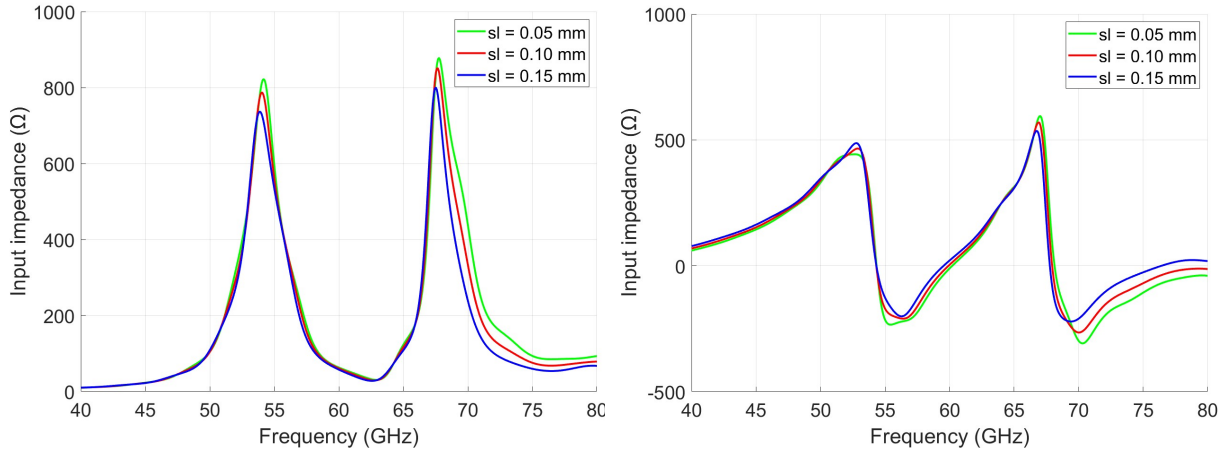

(a) Real Part. (b) Imaginary Part.

Figure 4.17: Impact of *sl* on the input impedance of the microstrip antenna.

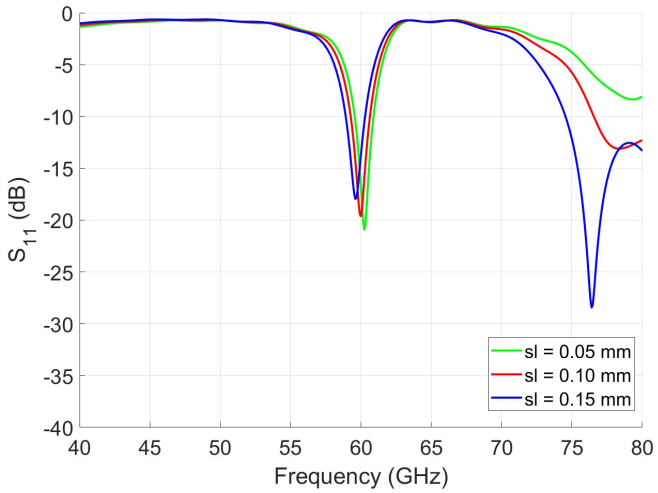

Figure 4.18: Impact of *sl* on the S_{11} parameter of the microstrip antenna.

Next, we examined the parameter *aux*, which was adjusted within the range of 0.15 mm to 0.05 mm. An analysis of the impedance, shown in Figure 4.19, reveals that increasing the value of *aux* results in reduced variations in both the real and imaginary parts across the frequency spectrum and the fading of the other mode of operation near 75 GHz. By looking at the S_{11} visible in Figure 4.20 increasing the *aux* value results in a slight decrease in the resonant frequency. It is also visible, that what appears to be another mode of operation disappears with an increase of this parameter as mentioned before.

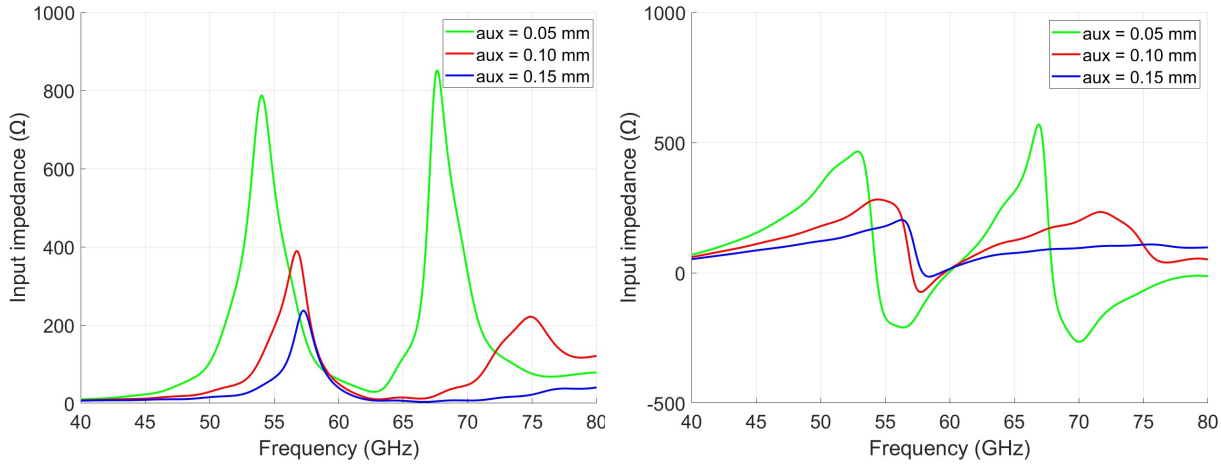

(a) Real Part. (b) Imaginary Part.

Figure 4.19: Impact of *aux* on the input impedance of the microstrip antenna.

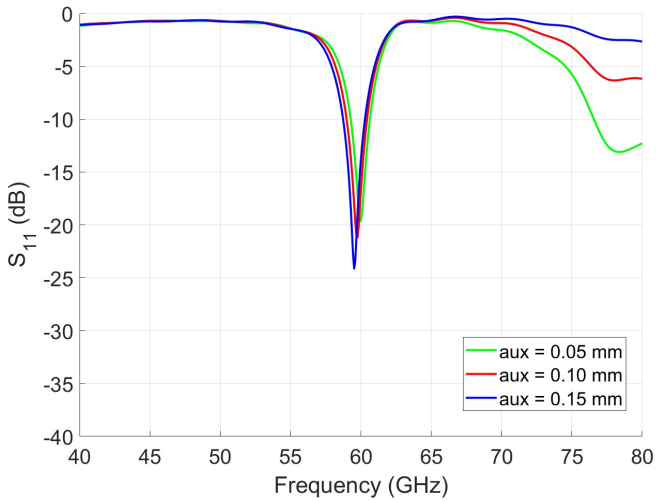

Figure 4.20: Impact of *aux* on the S_{11} parameter of the microstrip antenna.

The final parameter we investigated was *sx*, which was varied from 0.018 mm to 0.03 mm. As depicted in Figure 4.21, it is evident that this parameter has an impact on the input match which increases with the increase of the *sx*. By looking at the impedance in Figure 4.21, it is clear that the real and imaginary parts slightly shift to higher frequencies with the increase of the *sx* value.

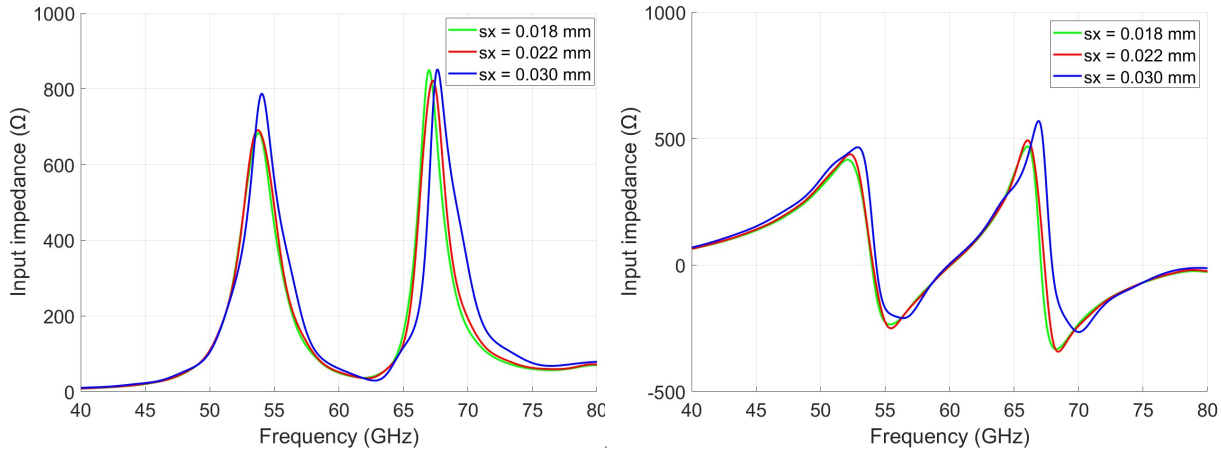

(a) Real Part. (b) Imaginary Part.

Figure 4.21: Impact of *sx* on the input impedance of the microstrip antenna.

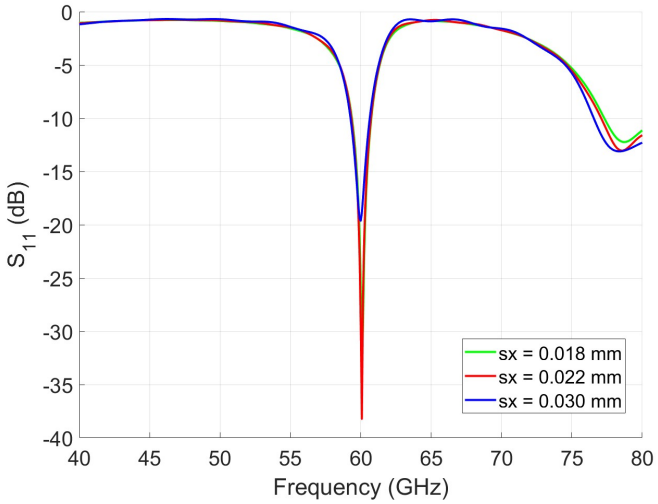

Figure 4.22: Impact of *sx* on the S_{11} parameter of the microstrip antenna.

4.2.3 Microstrip Patch Final Model on InP

Following a comprehensive understanding of how the inset feed functions, adjustments were made to optimize the input match at 60 GHz. For a comprehensive summary of the parameter values for this antenna, please refer to Table 4.1. The final microstrip design is presented in Figure 4.23, where is visible the presence of a bigger ground plane to understand the impact of a bigger metallic structure behind the antenna and the small dimensions of the substrate to respect the dimensions of the materials available from the manufacturer. The corresponding S_{11} and impedance are displayed in Figure 4.24a and Figure 4.24b, respectively. It was possible to obtain a S_{11} of ≈ -38.7 dB with a bandwidth of 1.39 GHz and an impedance of 50.6-j0.9 Ω.

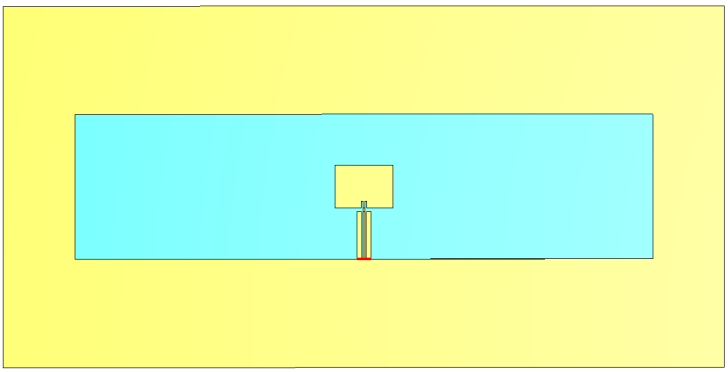

Figure 4.23: Microstrip final design.

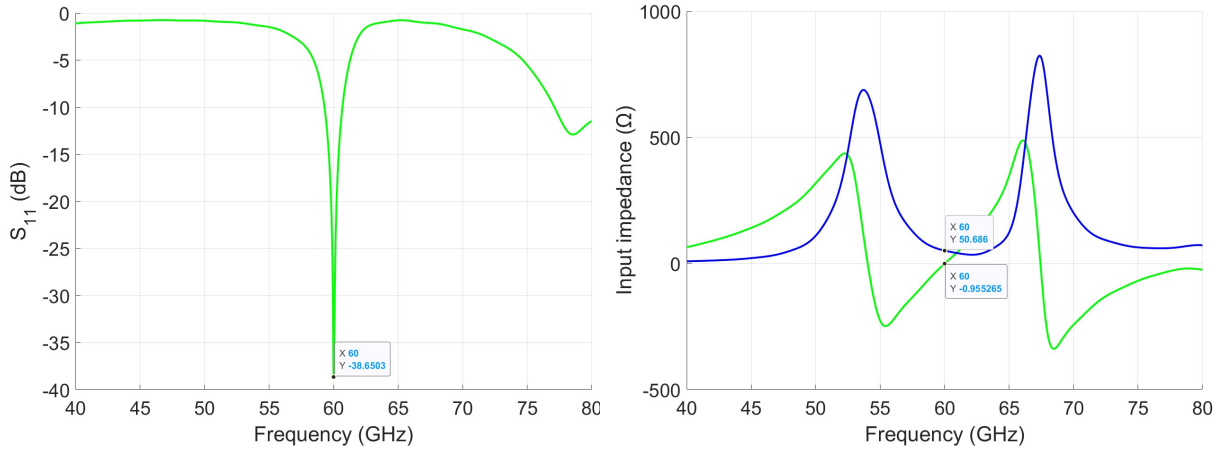

(a) S_{11}. (b) Impedance.

Figure 4.24: Final microstrip S_{11} and impedance.

Table 4.1: Patch antenna parameters and values.

Parameters	Value (mm)
Ground plane Length	5
Ground plane width	10
Patch length (L)	0.597
Patch width (W)	0.8
Substrate Length (Lg)	2
Substrate Width (Wg)	8
CPW line width	0.2
Inset length (sl)	0.1
Inset width (sx)	0.022
Distance between patch and CPW (aux)	0.05

We also examined the 2D and 3D radiation patterns, as illustrated in Figure 4.25 and Figure 4.26. Comparing the performance of this antenna with the FSA discussed in previous sections, it is evident that the FSA has a narrower angular width compared with the angular width of the microstrip which is 123.9° and 92.1° in the $\phi = 90°$ and $\phi = 90°$ planes, respectively, making it more directive and has higher gain. However, the microstrip patch antenna has greater efficiency, achieving a remarkable 95.5% radiation efficiency, and a broader bandwidth of 1.54 GHz.

For a comprehensive summary of the antenna's performance characteristics, please refer to Table 4.5.

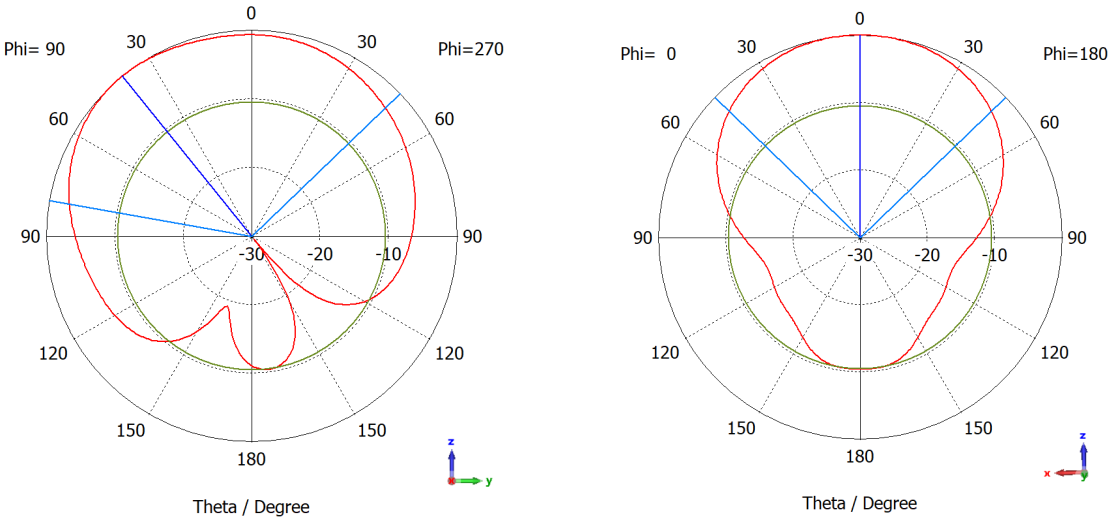

(a) $\phi = 90°$. (b) $\phi = 0°$.

Figure 4.25: Normalized radiation pattern for final microstrip model on InP.

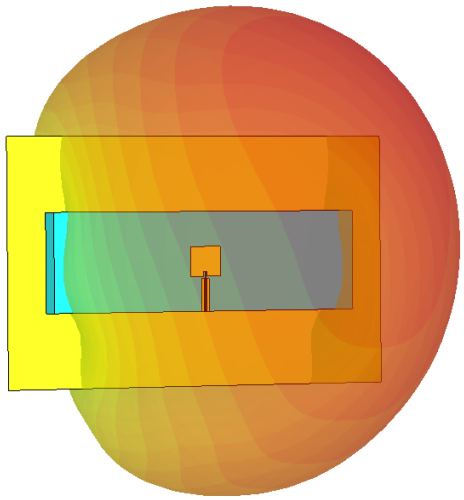

Figure 4.26: 3D radiation pattern microstrip on InP.

Table 4.2: Microstrip on InP overall performance.

Parameters	Value
S_{11}	- 38.6 dB
Gain	5.45 dBi
Efficiency	95.5%
Bandwidth	1.39 GHz

4.3 Microstrip Antenna on Silicon substrate

In this section, a microstrip antenna with a silicon substrate is studied since the manufacture calendar of the InP surpasses the calendar of this dissertation. As mentioned before, one of the problems of OCA's is the substrates used due to the combination of the use of antenna with integrated circuits that are built over lossy and high permittivity substrates such as silicon. So, the impact of the silicon substrate on the antenna is studied including all the other limitations associated such as the height and low resistivity of the silicon substrate.

In Section 4, a microstrip antenna on InP substrate with 250 µm is built. The same antenna was simulated but now on a silicon substrate with the same height and with the characteristics mentioned in Table 4.3.

Table 4.3: Silicon characteristics.

Parameters	Value
Permittivity	11.9
Resistivity	400 kΩ.cm
Height	300-600 μm

It is visible in Figure 4.27 that, by changing the substrate material, the resonant frequency increases. This has to do with the silicon permittivity being slightly smaller than the InP which affects the resonant frequency. So, to get the resonant frequency at 60 GHz the length of the patch was slightly increased to $\approx$ 0.6 mm.

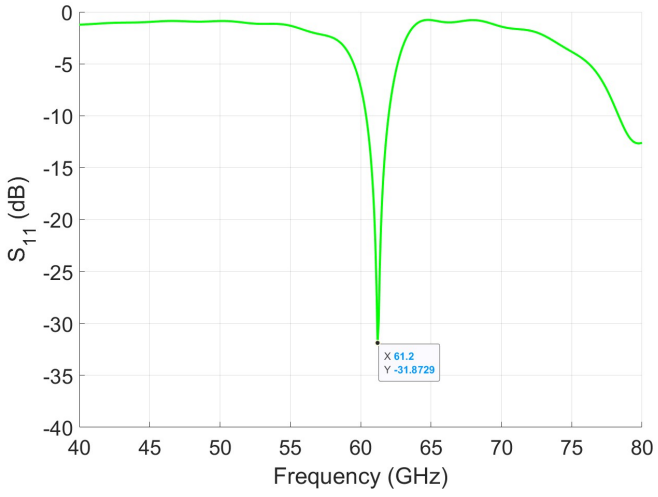

Figure 4.27: S_{11} microstrip antenna with silicon substrate.

4.3.1 Silicon Thickness impact

Depending on manufacturers, silicon substrates come in various thicknesses ranging from $\approx 300 - 600$ µm. In this section, we explore the impact of the thickness on the antenna performance. According to C. Balanis, thick substrates ($h > 0.02\lambda_0$) can increase surface waves [8], which affect the antenna performance. So, a parametric study on the substrate thickness, ranging from 100 µm to 600 µm was made to understand the impact of the thickness on the antenna input match and radiation pattern.

Figure 4.28 shows the impact of different substrate heights on the input match. As we can see, as the height of the substrate increases, the resonant frequency decreases and other modes start to appear in the frequency range. Since the value of the height begins to approach the value of the width and length of the patch, the appearance of other modes can be due to the resonance frequencies imposed by the height of the substrate.

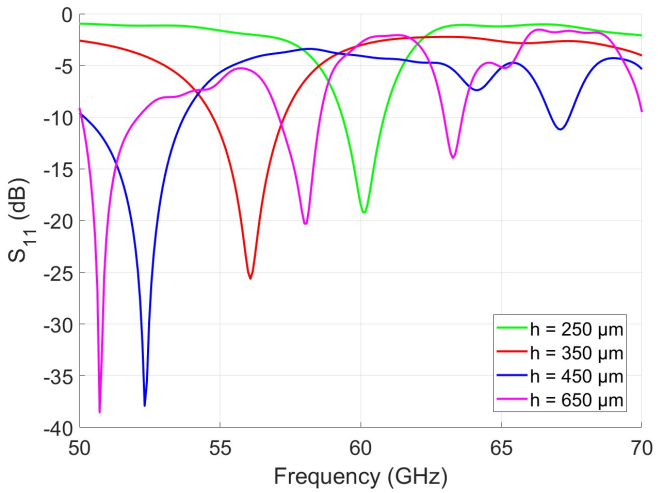

Figure 4.28: Thickness impact on S_{11} of the microstrip antenna on silicon.

Using the S_{11} below -10 dB as fundamental criteria, the microstrip antenna was dimensioned for substrates with heights between 100 µm to 600 µm with an increase of 25 µm. Figure 4.29a displays the input match and Figure 4.29b the total and radiation efficiency for several heights. It is evident that after 350 µm, achieving an input match solely by varying antenna dimensions becomes challenging. It is also visible that the total radiation, as expected, is affected by the input match after 350 µm. However, for a substrate height of 600 µm, the antenna's S_{11} falls below -10 dB. It's worth noting that this phenomenon may be attributed to surface waves and may not be entirely within the author's control.

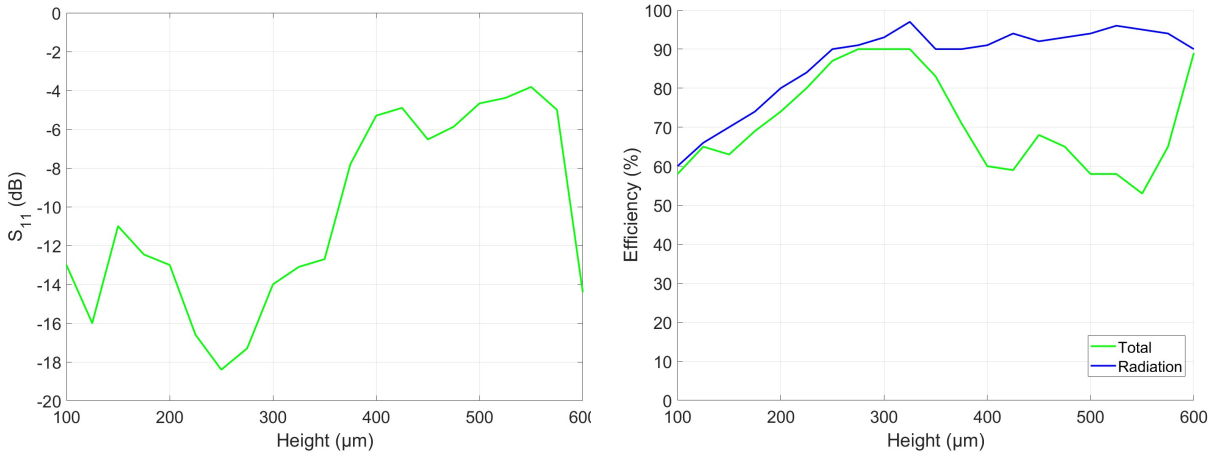

(a) S_{11}. (b) Efficiency.

Figure 4.29: S_{11} and efficiency for several substrate heights of the microstrip antenna on silicon.

The normalized 2D radiation pattern was also observed for substrate heights between 100 µm to 600 µm but with an increase of 100 µm from Figures 4.30 to 4.35.

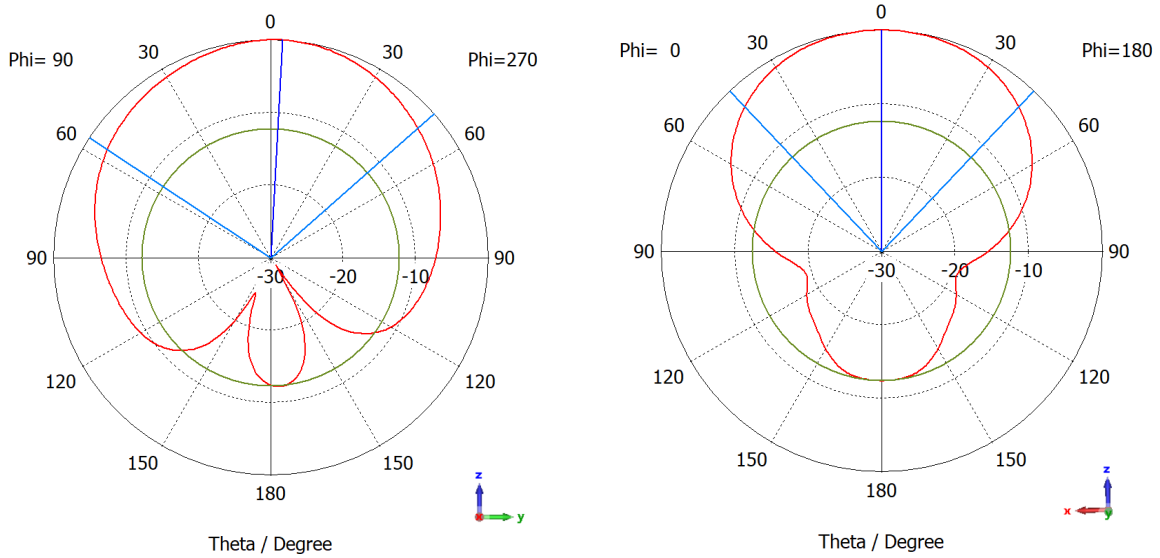

(a) $\phi = 90°$. (b) $\phi = 0°$.

Figure 4.30: Normalized radiation pattern of the microstrip antenna on silicon with a height of 100 µm.

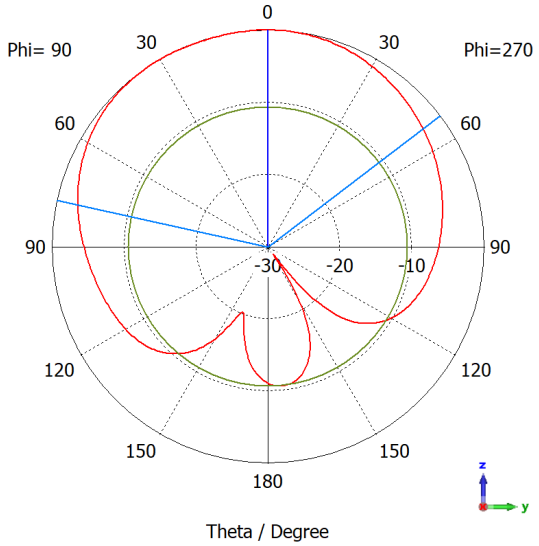

(a) $\phi = 90°$.

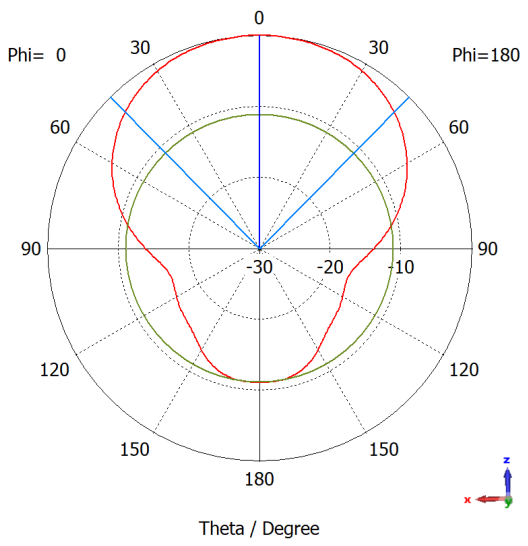

(b) $\phi = 0°$.

Figure 4.31: Normalized radiation pattern of the microstrip antenna on silicon with a height of 200 µm.

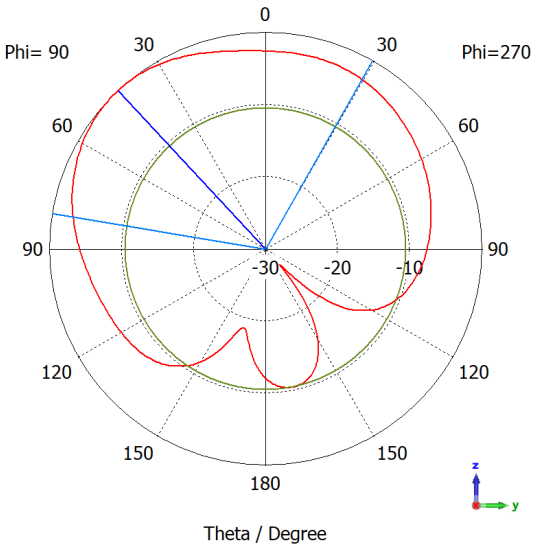

(a) $\phi = 90°$.

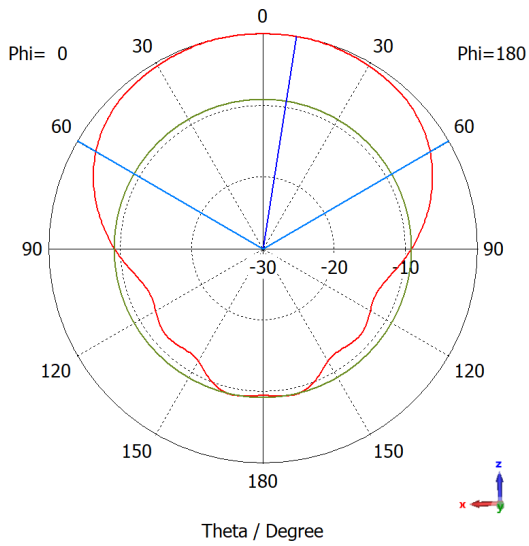

(b) $\phi = 0°$.

Figure 4.32: Normalized radiation pattern of the microstrip antenna on silicon with a height of 300 µm.

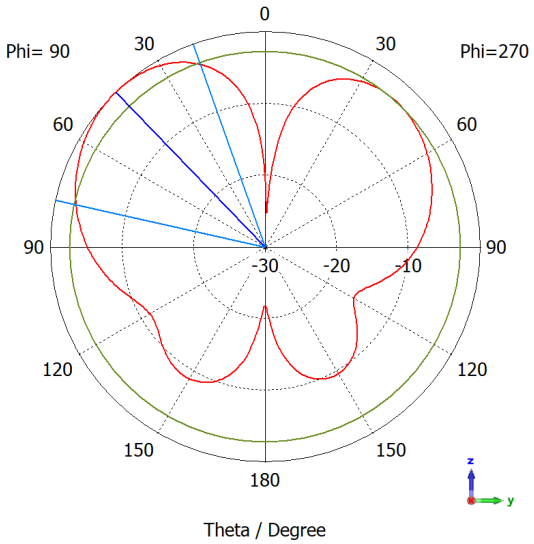

(a) $\phi = 90°$.

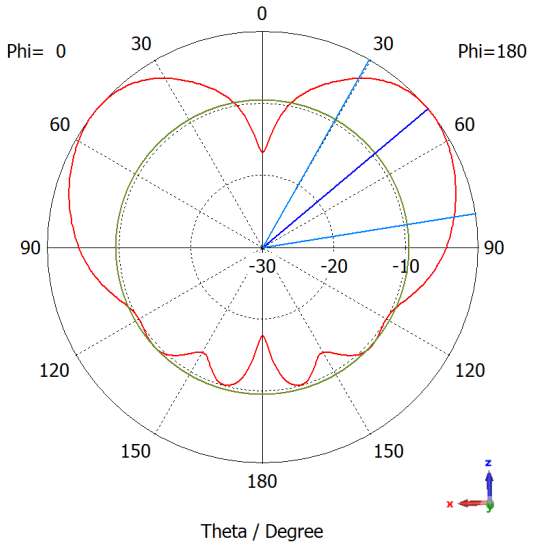

(b) $\phi = 0°$.

Figure 4.33: Normalized radiation pattern of the microstrip antenna on silicon with a height of 400 µm.

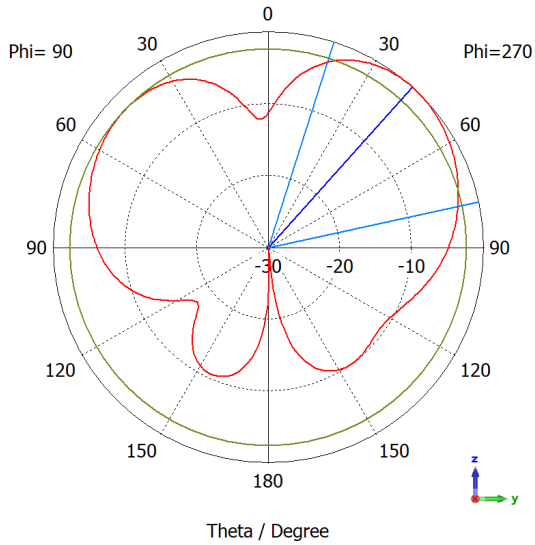

(a) $\phi = 90°$.

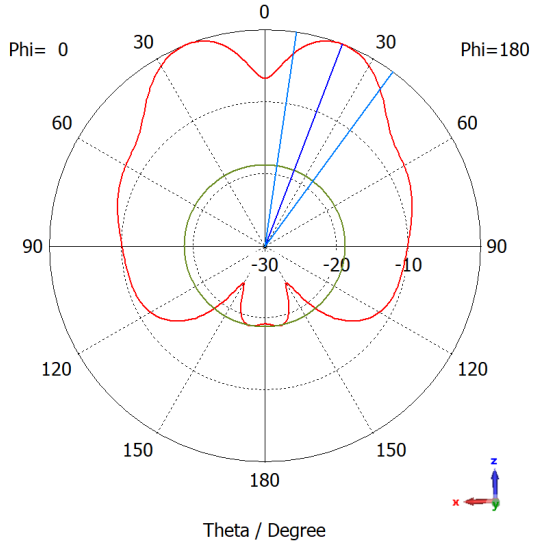

(b) $\phi = 0°$.

Figure 4.34: Normalized radiation pattern of the microstrip antenna on silicon with a height of 500 µm.

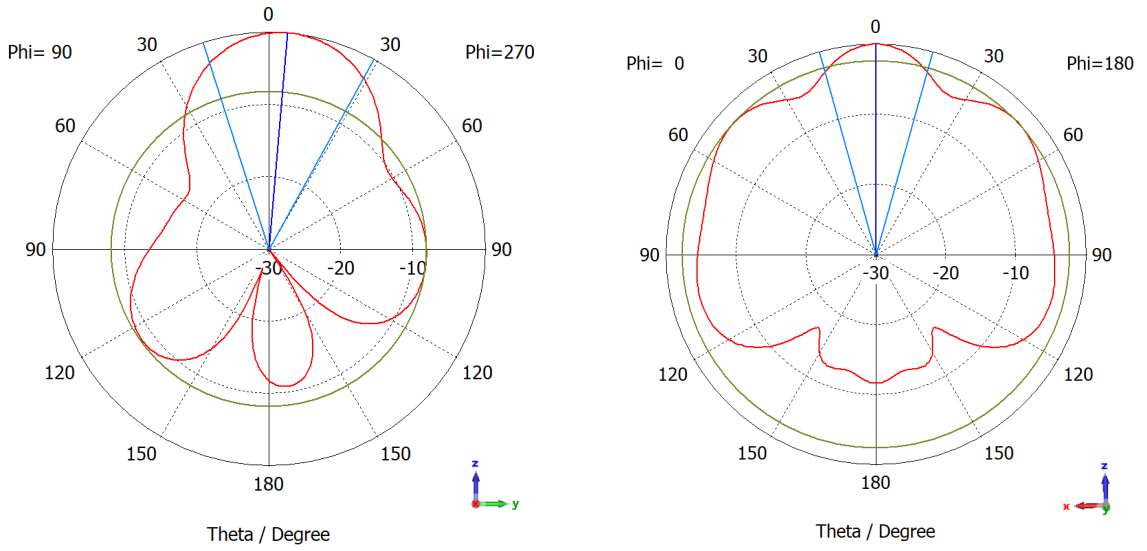

(a) $\phi = 90°$. (b) $\phi = 0°$.

Figure 4.35: Normalized radiation pattern of the microstrip antenna on silicon with a height of 600 µm.

The radiation pattern for values that pass 300 µm starts to deform losing its directivity and total efficiency, by not being possible to get the S_{11} < -10 dB for the first mode of operation. This effect can be caused by surface waves. However, another possible effect can be explained by the modes imposed by the substrate height. As mentioned before, a microstrip patch works like a resonant cavity, the operation modes are imposed by the antenna's dimensions including the height between the upper and lower conductors, i.e. the substrate height. So, the antenna input match at 600 µm can be an effect imposed by the substrate height which is approximately $\lambda/2$. In conclusion, to ensure a good radiation pattern and proper functioning, it is necessary to limit the substrate height to 300 µm.

4.3.2 Resistivity impact

As mentioned in Chapter 2, one of the major issues with silicon substrates for OCA is their low resistivity which affects their loss tangent affecting the antenna performance. To understand this impact three resistivities were tested 10 $\Omega \cdot cm$, 10 $k\Omega \cdot cm$, and 400$k\Omega \cdot cm$. These values are according to the materials available for posterior construction and the last value with the standard silicon substrate present in the CST materials library. As it is visible in Figure 4.36, the resistivities of 10 $k\Omega \cdot cm$ and 400 $k\Omega \cdot cm$ have a similar impact on the antenna operation but, the 10 $\Omega \cdot cm$ resistivity has a significant impact. When examining the radiation pattern, as shown in Figure 4.37, it becomes evident

that the antenna loses its directivity, and the gain and efficiency are reduced to -3.69 dBi and 5%, respectively.

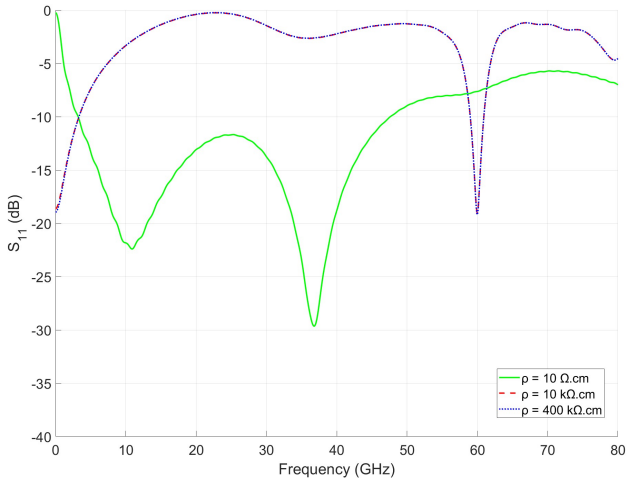

Figure 4.36: Resistivity of the silicon impact on S_{11} of the microstrip antenna.

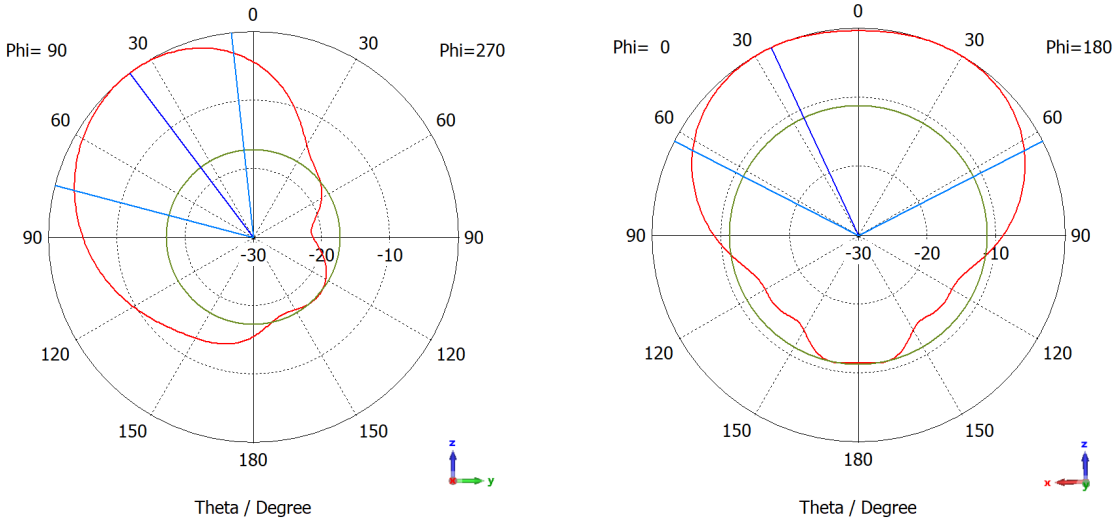

(a) $\phi = 90°$. (b) $\phi = 0°$.

Figure 4.37: Normalized radiation Pattern of the microstrip antenna on silicon with low resistivity substrate.

4.3.3 Microstrip Patch final model in Silicon

Considering every conclusion taken from the previous sections, a final model of the silicon antenna was simulated. Table 4.4 shows the parameter values for the antenna. The S_{11} and impedance are present in Figure 4.38. The antenna exhibits an input match

of approximately -23 dB with a bandwidth of 2.18 GHz at 60 GHz. The height used for this antenna was 300 µm to ensure the proper functioning of the antenna, and the resistivity used was 10 $k\Omega \cdot cm$, in line with the available materials.

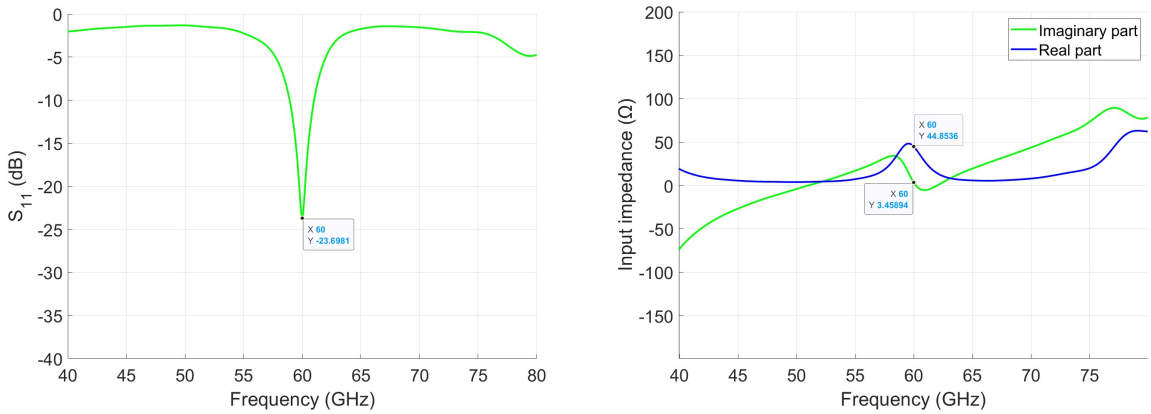

(a) S_{11}. (b) Impedance.

Figure 4.38: Final microstrip S_{11} and impedance on silicon.

Table 4.4: Patch antenna parameters and values with Silicon substrate.

Parameters	Value (mm)
Ground plane Length	5
Ground plane width	10
Patch length (L)	0.58
Patch width (W)	0.73
Substrate Length (Lg)	2
Substrate Width (Wg)	8
CPW line width	0.2
Inset length (sl)	0.05
Inset width (sx)	0.04
Distance between patch and CPW (aux)	0.15

The 2D and 3D radiation patterns were also observed in Figure 4.39 and Figure 4.40, respectively. We can see that the radiation pattern is similar to the one present in Chapter 4 having a slightly larger angular width of 124.1° and 107.9° in the $\phi = 90°$ and $\phi = 0°$ planes, respectively. Table 4.5 resumes the performance of the antenna, which presents a similar gain, smaller efficiency, and a bigger bandwidth than the antenna with the InP substrate.

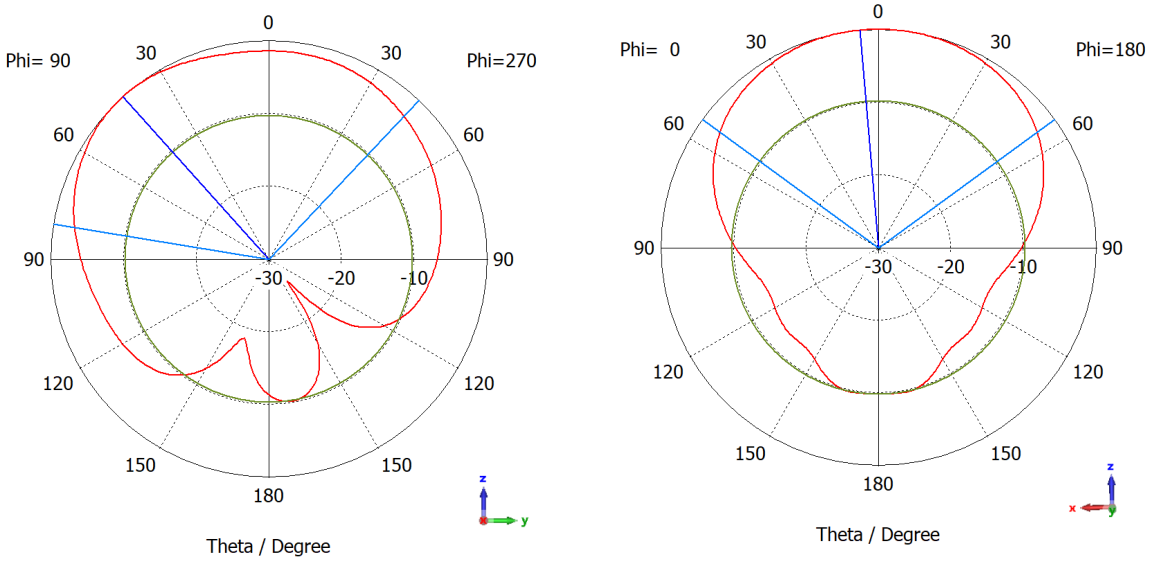

(a) $\phi = 90°$. (b) $\phi = 0°$.

Figure 4.39: Normalized radiation pattern for final microstrip model on silicon substrate.

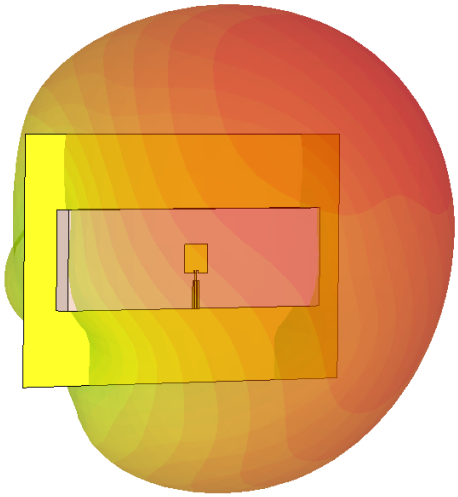

Figure 4.40: 3D radiation pattern of microstrip on silicon substrate.

Table 4.5: Microstrip on silicon overall performance.

Parameters	Value
S_{11}	- 23.7 dB
Gain	5.28 dBi
Efficiency	89%
Bandwidth	2.18 GHz

5

Antenna Array

In this chapter, an antenna array is built on silicon technology. Creating an array can benefit the antenna performance as it can improve the antenna gain and directivity. A previous study based on a tool from CST was made. This study allows a prediction of the antenna radiation pattern, gain, side lobes, etc.. After that, the array was built with several elements in order to compare the results with the prediction and conclude the number of elements necessary and their positioning. A study of the feeding method was made and the final array design is presented.

5.1 Array Design

A single-element antenna can have a relatively wide radiation pattern and low directivity hence low gain. In many applications, it is necessary to design antennas that can reach long distances and so have a high gain. By increasing the electrical size of the antenna, this can be possible. Another approach to increase the electrical length of an antenna and therefore increase directivity (and gain) is to form an assembly of multiple elements of antennas called an array [8]. The total field of the array is determined by the vector addition of the fields radiated by the individual elements assuming that the current in each element is the same as that of the isolated element therefore neglecting coupling. To obtain very directive patterns it is important that each field from each element interfere constructively in the proper direction and destructively in others. So, when building an array of identical elements it is important to consider some

key aspects in order to shape the overall pattern of the antenna [8]. These are:

- Geometrical configuration;
- Displacement between elements;
- Amplitude of each element;
- Phase of each element;
- Relative pattern of each element.

5.1.1 Analitical Model

Besides placing elements along a line (to form a linear array), it is possible to position additional elements along a rectangular grid forming a planar array. Planar arrays can provide additional parameters that allow us to manipulate the pattern of the array providing more symmetrical patterns with lower side lobes. Figure 5.1 represents the geometry of this array which can be looked at as a combination of M linear arrays with N elements. Considering the array factor of a N-element linear array with uniform amplitude and spacing, according to [8], can be given by Equation 5.1.

$$F_{\psi} = \frac{\sin(\frac{N}{2}\psi)}{\sin(\frac{1}{2}\psi)} \tag{5.1}$$

Where N is the number of elements and ψ is given by Equations 5.2 and 5.3 if the array is in the x- and y-directions with d as spacing between elements and β the phase shift along the x- and y- axis The array factor for the entire planar array is given by the array factor of two linear arrays resulting in a total electric field (E_T) give by Equation 5.4 considering the electric field of a single element at the reference point (E_S) times the array factor at X (F_X) and Y (F_Y). Planar arrays have many applications including tracking radar, search radar, remote sensing, communications and others [8].

$$\psi = kd_x \sin\theta\cos\phi + \beta_x \tag{5.2}$$

$$\psi = kd_y \sin\theta\sin\phi + \beta_y \tag{5.3}$$

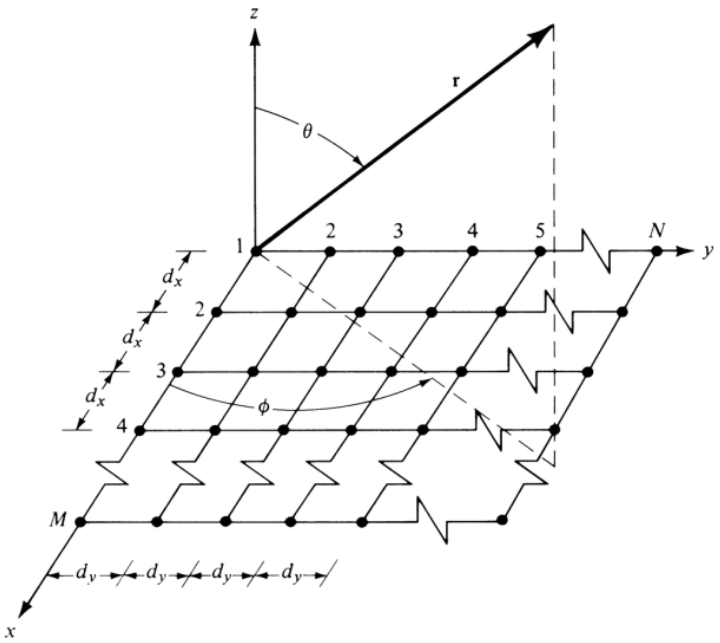

Figure 5.1: Planar array [8].

$$E_T = E_S \times [F_X F_Y] \tag{5.4}$$

5.1.2 Numerical Model

Building an array can be beneficial to the antenna's performance because it can increase the gain compared with a single patch element and can increase the antenna's directivity. However, this depends on other factors such as the number of elements, their position, and spacing. This section aims to explore these factors by predicting the array behavior using the 'Farfield Calculation of Antenna Arrays' tool from CST.

Starting with two elements horizontally, the spacing was changed from 2.5 mm ($\frac{\lambda_0}{2}$) to 1.095 mm (minimum distancing considering $3 \times \frac{L}{2}$). Figures 5.2, 5.3 and 5.4 show the radiation pattern for $\phi = 90°$ and $\phi = 0°$ for 1.095 mm, 1.7595 mm and 2.5 mm distance between elements. As we can observe from these figures, as the distancing increases, the angular width on the $\phi = 0°$ plane decreases turning the radiation pattern in this plane more directive.

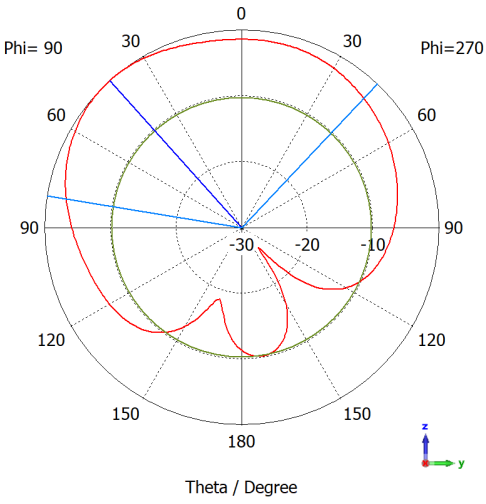

(a) $\phi = 90°$.

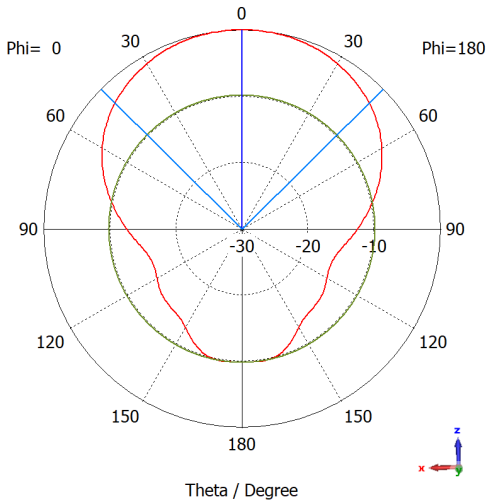

(b) $\phi = 0°$.

Figure 5.2: Normalized radiation pattern of 2-element horizontal array with 1.095 mm distancing.

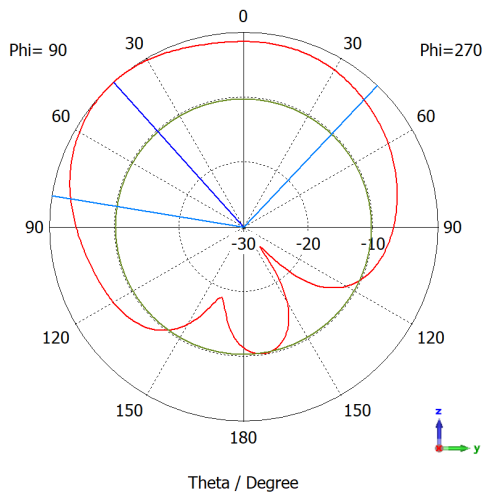

(a) $\phi = 90°$.

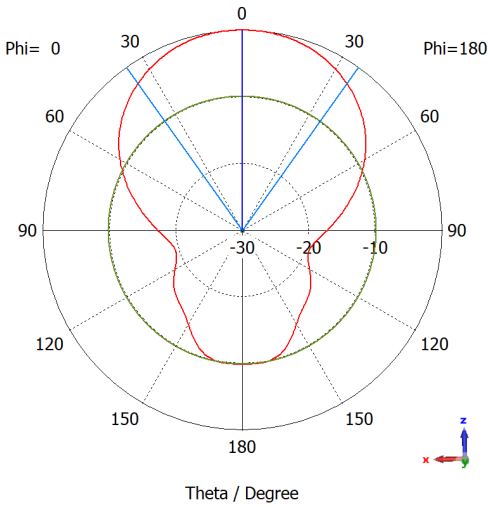

(b) $\phi = 0°$.

Figure 5.3: Normalized radiation pattern of 2-element horizontal array with 1.7595 mm distancing.

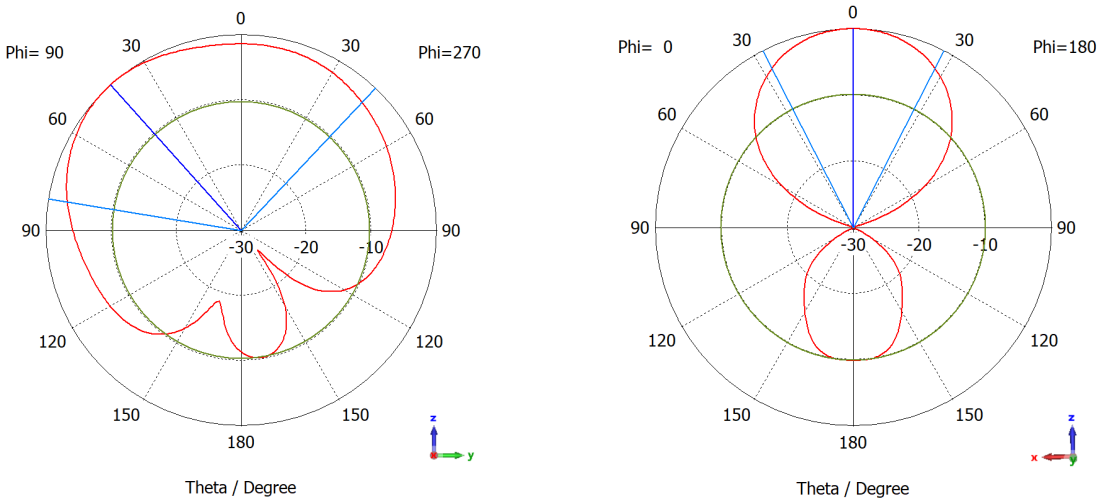

(a) $\phi = 90°$. (b) $\phi = 0°$.

Figure 5.4: Normalized radiation pattern of 2-element horizontal array with 2.5 mm distancing.

Table 5.1 compares the radiation aspects of the 2-element array. It's visible that by increasing the spacing between elements there is an improvement in terms of gain and, as mentioned before, in terms of directivity in the $\phi = 0°$ plane as it decreases from 90.6° to 54.3°. In terms of side lobes, the side lobe level remains practically the same for the three spacings simulated.

Table 5.1: Radiation pattern aspects for the 2-element horizontal array.

Spacing (mm)	Angular width (Degree)		Gain (dBi)	Side lobe level (dB)	
	$\phi = 0°$	$\phi = 90°$	——	$\phi = 0°$	$\phi = 90°$
1.095	90.6	124.4	5.7	-9.8	-10.3
1.7995	70.1	124.4	6.4	-9.9	-10.3
2.5	54.3	124.4	7.3	-9.9	-10.3

The same study was made but now considering a 2-element vertical array. The radiation patterns for several distances are present in Figures 5.5, 5.6 and 5.7. In this case, we can observe that by increasing the distance of the elements on the y-plane, the angular width on the $\phi = 90°$ decreases as the $\phi = 0°$ maintains the same angular width.

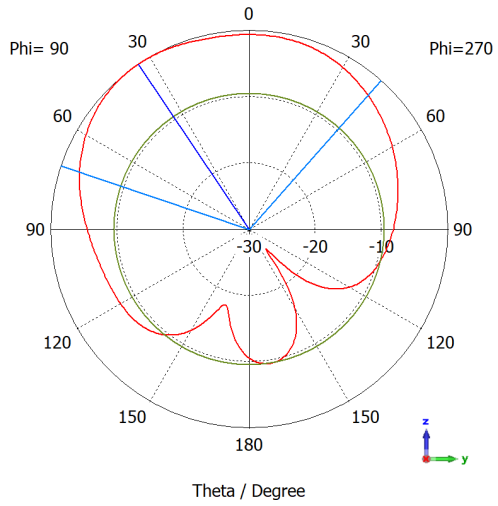

(a) $\phi = 90°$.

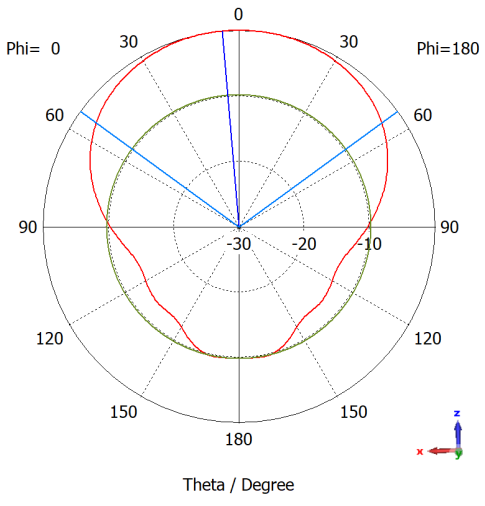

(b) $\phi = 0°$.

Figure 5.5: Normalized radiation pattern of 2-element vertical array with 1.095 mm distancing.

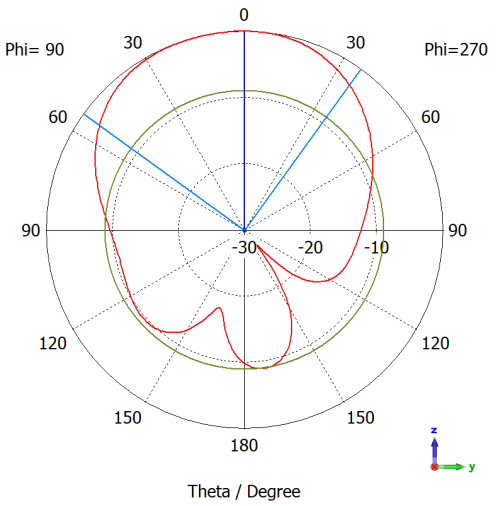

(a) $\phi = 90°$.

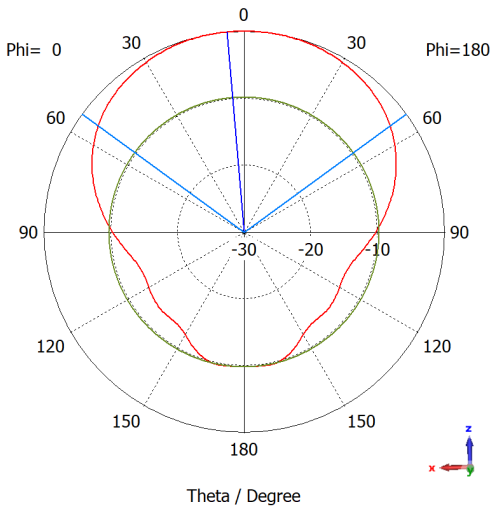

(b) $\phi = 0°$.

Figure 5.6: Normalized radiation pattern of 2-element vertical array with 1.7595 mm distancing.

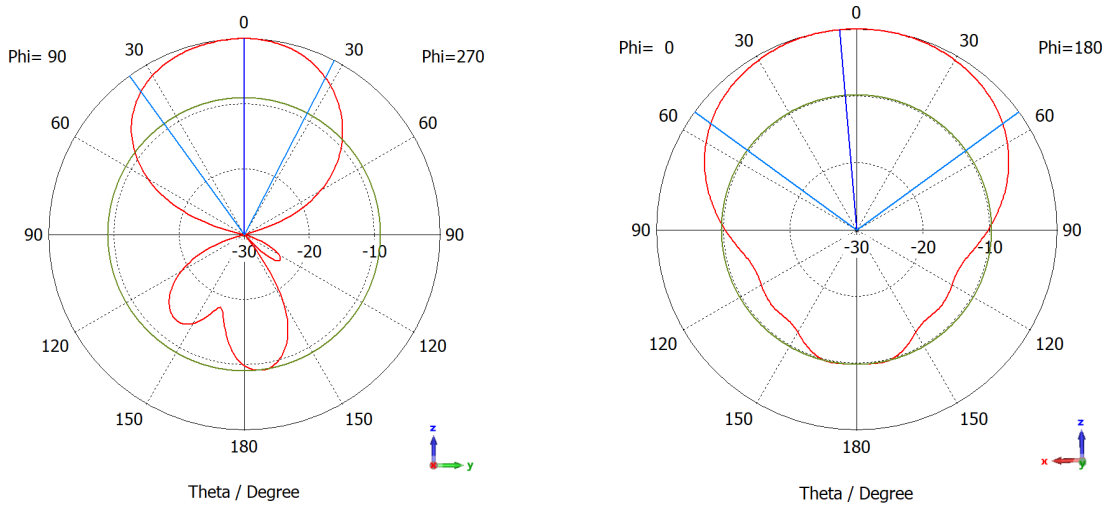

(a) $\phi = 90°$. (b) $\phi = 0°$.

Figure 5.7: Normalized radiation pattern of 2-element vertical array with 2.5 mm distancing.

Table 5.2 resumes the antenna performance in terms of radiation aspects. The element on top brings the same effect as the element on the side by increasing the gain as the distance between elements increases but now in terms of angular width, as mentioned before, the angular width decreases in the $\phi = 90°$ concluding that it may be advantageous to explore the possibility of a 4 element array 2x2 with a maximum distance of 2.5 mm.

Table 5.2: Radiation pattern aspects for 2-element vertical array.

Spacing (mm)	Angular width (Degree)		Gain (dBi)	Side lobe level (dB)	
	$\phi = 0°$	$\phi = 90°$	——	$\phi = 0°$	$\phi = 90°$
1.095	107.7	112.7	5.36	-9.8	-9.5
1.7995	107.7	88.7	5.9	-9.8	-10.3
2.5	107.7	63.4	7.1	-9.8	-9

The same simulation was made but now considering 4 elements with a spacing of 2.5 mm. The radiation pattern is present in Figure 5.8. It was possible to achieve a 9.75 dBi gain and an angular width decrease in both the $\phi = 90°$ and $\phi = 0°$ planes. Table 5.3 resumes these values including the side lobe level which is a little higher compared with the results obtained previously.

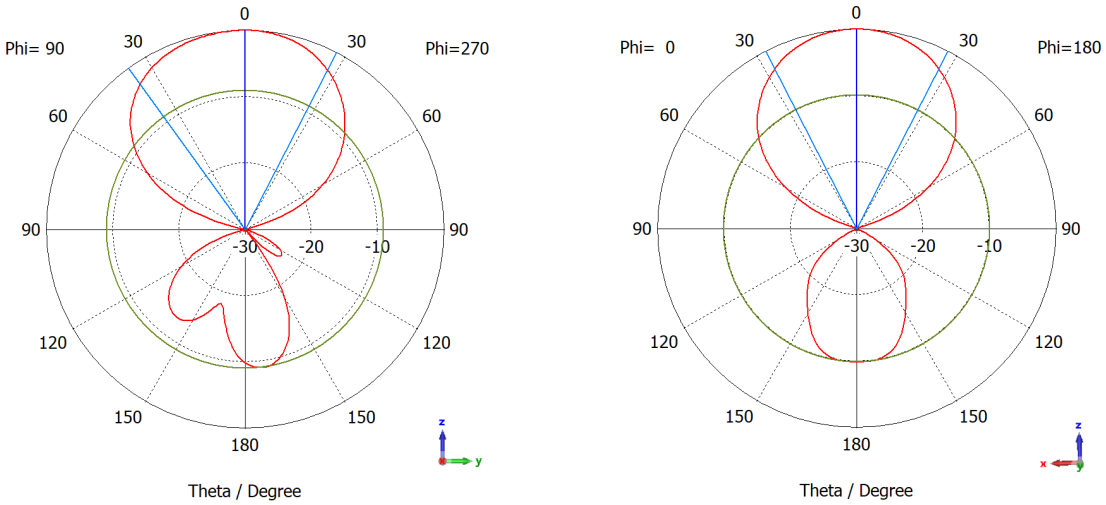

(a) $\phi = 90°$. (b) $\phi = 0°$.

Figure 5.8: Normalized radiation pattern of the 4-element array with 2.5 mm distancing.

Table 5.3: Radiation pattern aspects of the 4-element array.

	Angular width (Degree)		Gain (dBi)	Side lobe level (dB)	
	$\phi = 0^o$	$\phi = 90^o$	——	$\phi = 0^o$	$\phi = 90^o$
4 element array	54.3	63.4	9.75	-9.9	-9

5.2 Simulation with discrete port

In this section, the three arrays were simulated using a discrete port in order to compare the results with the CST prediction tool. Starting with the two elements horizontally, the antenna model is present in Figure 5.9 and the radiation pattern in Figure 5.10. Comparing the results with the previous simulation, described in Table 5.4, it is visible that the simulation with the discrete port showed better results in terms of angular width, gain, and side lobe level than the prediction.

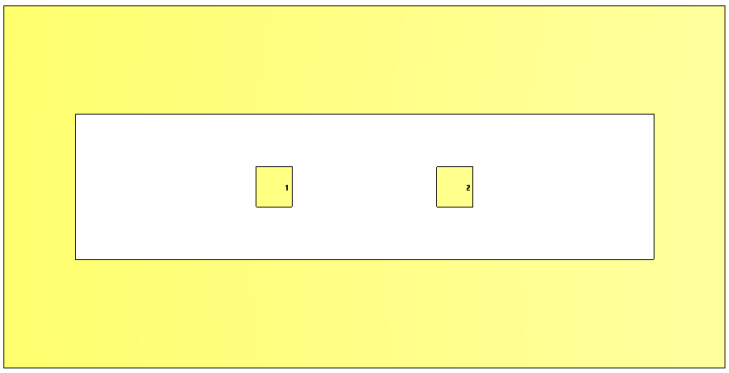

Figure 5.9: 2-element horizontal array structure with discrete port.

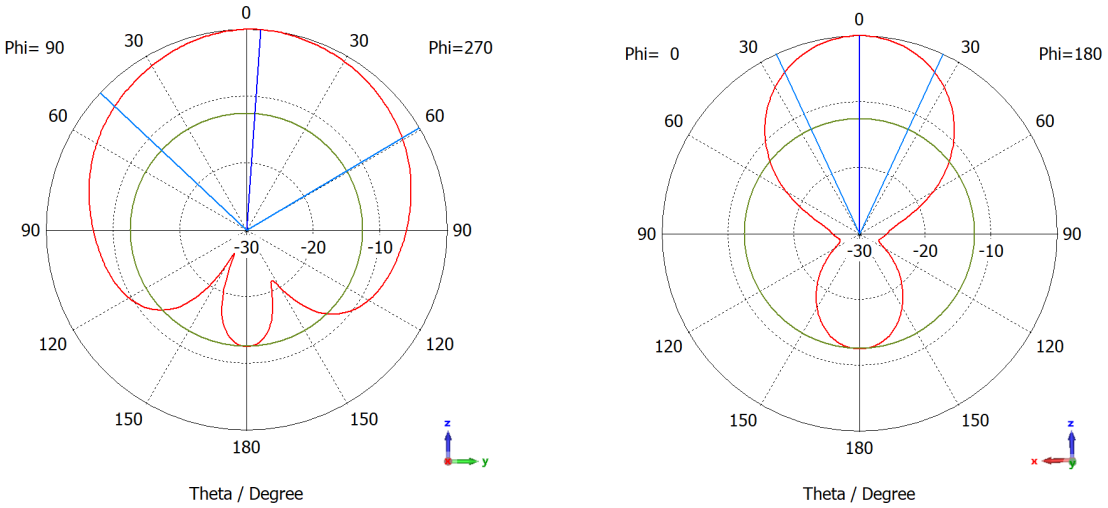

(a) $\phi = 90°$. (b) $\phi = 0°$.

Figure 5.10: Normalized radiation pattern of 2-element horizontal array with discrete port.

Table 5.4: Prediction vs Simulation for 2-element horizontal array.

	Angular width (Degree)		Gain (dBi)	Side lobe level (dB)	
	$\phi = 0^o$	$\phi = 90^o$	——	$\phi = 0^o$	$\phi = 90^o$
Prediction	54.3	124.4	7.3	-9.9	-10.3
Simulation	49.7	106.3	8.3	-12.5	-12.6

As for the 2-element vertical array, present in Figure 5.11, the radiation pattern is present in Figure 5.12, and as it is visible in Table 5.5, the angular width is smaller than expected but the gain is smaller and the side lobe level is greater. The differences

between the expected and simulated radiation pattern come from the need to increase the substrate in order to fit the two elements vertically with a spacing of 2.5 mm.

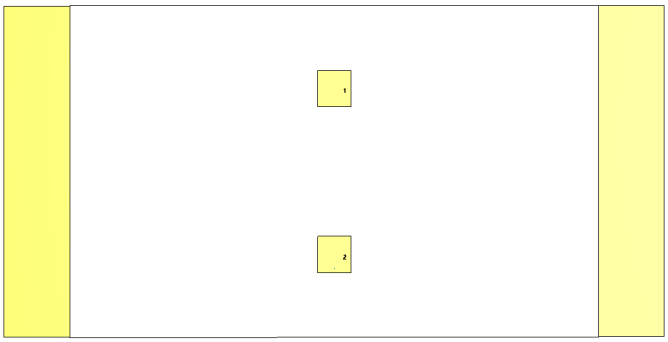

Figure 5.11: 2-element vertical array structure with discrete port.

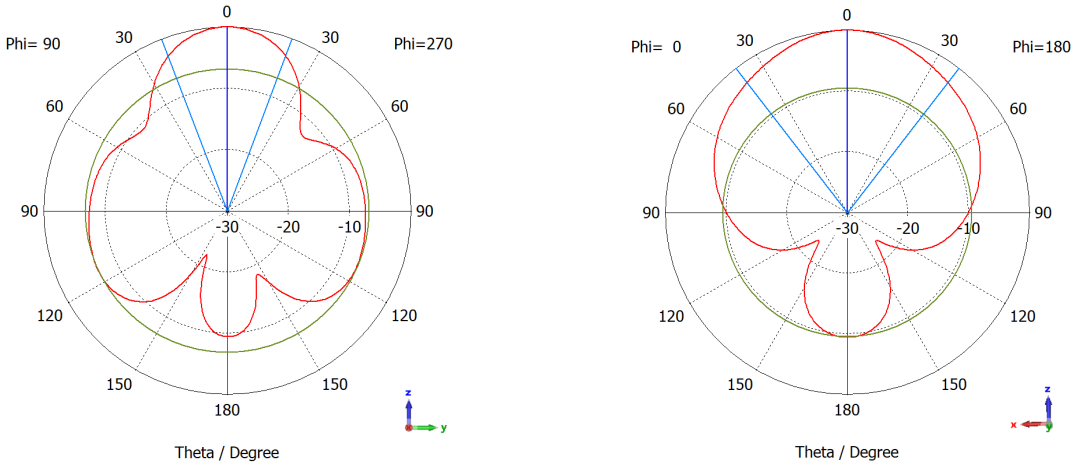

(a) $\phi = 90°$. (b) $\phi = 0°$.

Figure 5.12: Normalized radiation pattern of 2-element vertical array with discrete port.

Table 5.5: Prediction vs Simulation for 2-element vertical array.

	Angular width (Degree)		Gain (dBi)	Side lobe level (dB)	
	$\phi = 0^o$	$\phi = 90^o$	——	$\phi = 0^o$	$\phi = 90^o$
Prediction	107.7	63.4	7.2	-9.8	-9
Simulation	86.5	43.4	6.1	-9.7	-4.1

Later, the 4-element array was built and the antenna design can be seen in Figure 5.13 For the antenna performance compared to the expected results, the same shows an

improvement in directivity in both planes (ϕ = 0° and ϕ = 90°), shown in Figure 5.14, and a higher gain. Table 5.6, presents a comparison between the prediction and the simulation for this array.

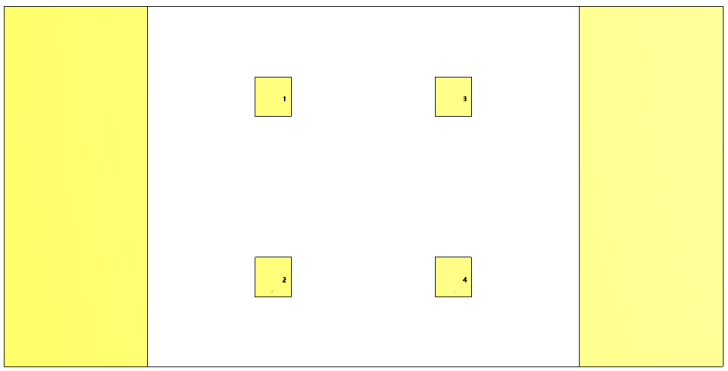

Figure 5.13: 4-element array structure with discrete port.

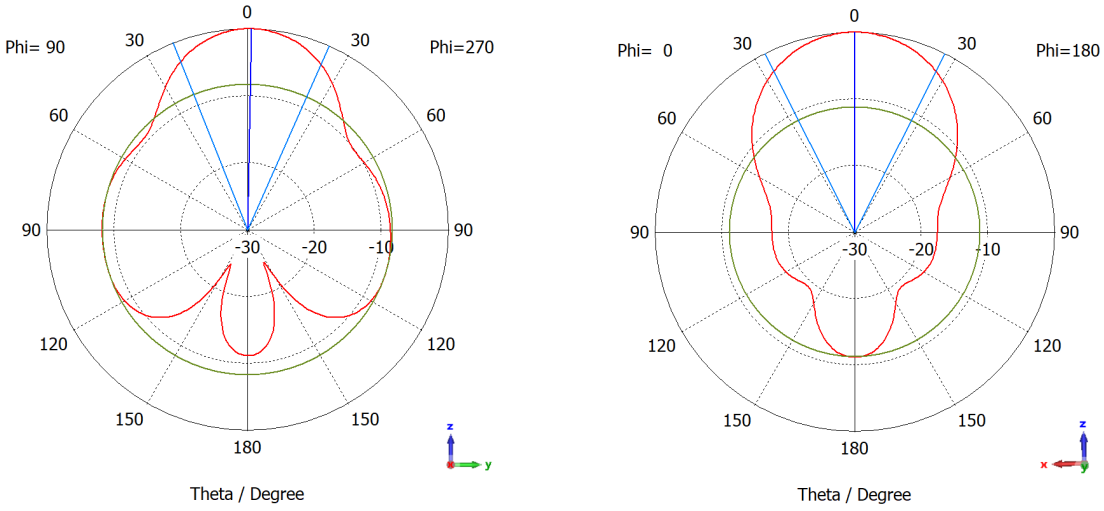

(a) $\phi = 90°$. (b) $\phi = 0°$.

Figure 5.14: Normalized radiation pattern for 4 elements with discrete port.

Table 5.6: Prediction vs Simulation for 4-element array.

	Angular width (Degree)		Gain (dBi)	Side lobe level (dB)	
	ϕ = 0°	ϕ = 90°	——	ϕ = 0°	ϕ = 90°
Prediction	54.3	63.4	9.75	-9.9	-9
Simulation	53.6	45.6	10.28	-11.2	-8.3

5.3 Feeding network

After studying the impact of having various elements present in the array, the implementation of the feed line was studied. In this case, due to the complexity of feeding every element with a CPW line, a feed line network was implemented and the impedance was analyzed in several points in order to obtain a 50 Ω line in the end.

First, a 100 Ω line was built as seen in Figure 5.15, guaranteeing that all elements are in phase with a line that has the same length reaching the four elements of the array the impedance at the center point, marked by the red dot, was observed having 36+j61 Ω impedance present in Figure 5.16.

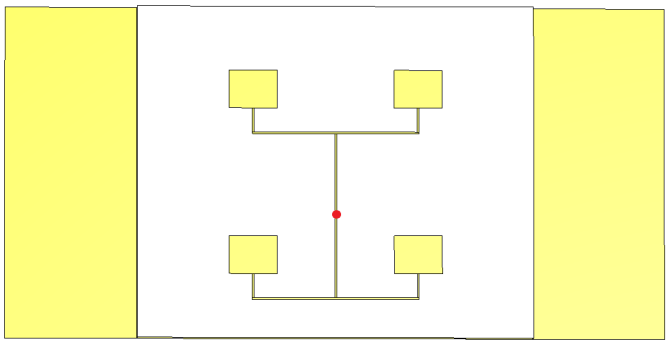

Figure 5.15: Array feeding network line 1.

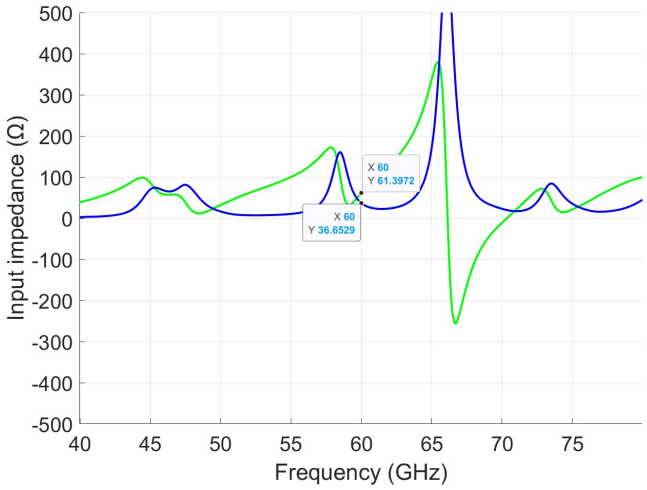

Figure 5.16: Array feeding network line 1 impedance.

In order to cancel the imaginary part of the impedance, a line with a characteristic impedance of 50 Ω was built and the electric length was calculated to have the imaginary part nullified. The line was built until the end of the structure, as visible in Figure

5.17, to enable the use of the waveguide port and change the reference distance to the one matching the electric distance marked by the red line. As we can see in Figure 5.18 it was possible to achieve an impedance of 129+j2 Ω with a line length of 0.518 mm.

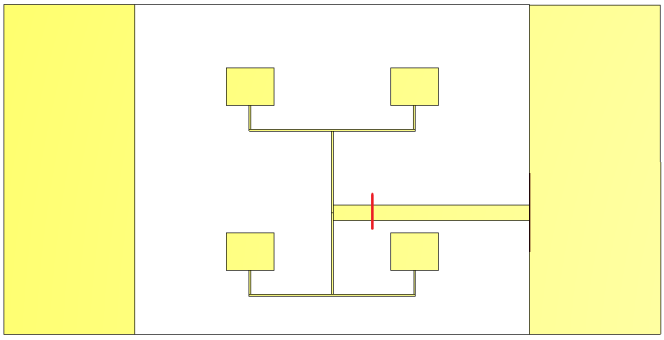

Figure 5.17: Array feeding network line 2.

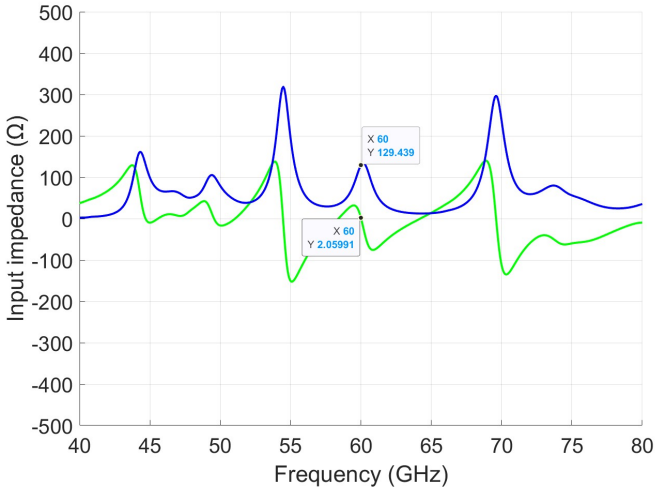

Figure 5.18: Array feeding network line 2 impedance.

At this stage, to get the intended 50 Ω (Z_0) impedance it's necessary to use a quarter wavelength transformer. Using Equation 5.3 it's possible to calculate the characteristic impedance necessary ($Z_{\frac{\lambda}{4}}$).

$$Z_{\frac{\lambda}{4}} = \sqrt{Z_0 \cdot Z_{in}} \tag{5.5}$$

Figure 5.19 shows the structure with the quarter wavelength transformer with a characteristic impedance of 80 Ω (Z_{in}). The distance to achieve the closest value to 50 Ω was 0.372 mm and the impedance can be seen in Figure 5.20 reaching 44-j0.2 Ω.

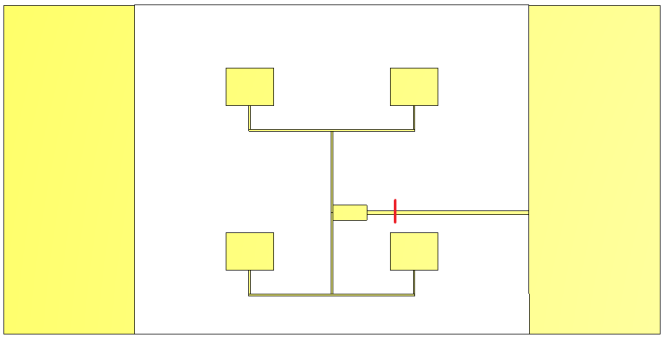

Figure 5.19: Array feeding network line 3.

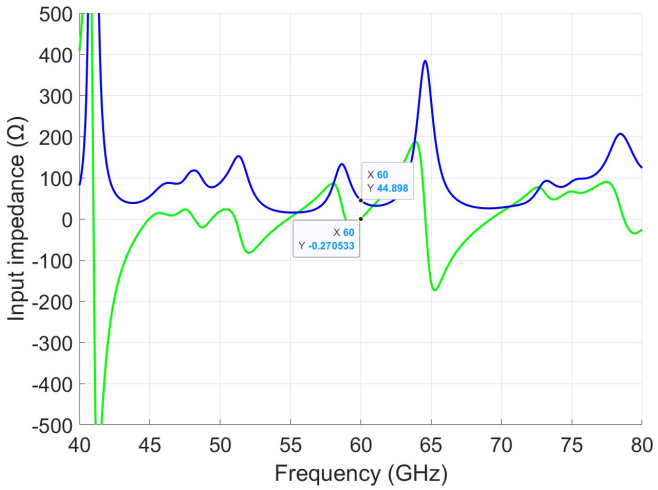

Figure 5.20: Array feeding network line 3 impedance.

Finally, the 50Ω line was implemented as visible in Figure 5.21 and the S_{11} and impedance were observed in Figure 5.22 achieving a $44 - j2\ \Omega$ impedance and a -23.8 dB input match.

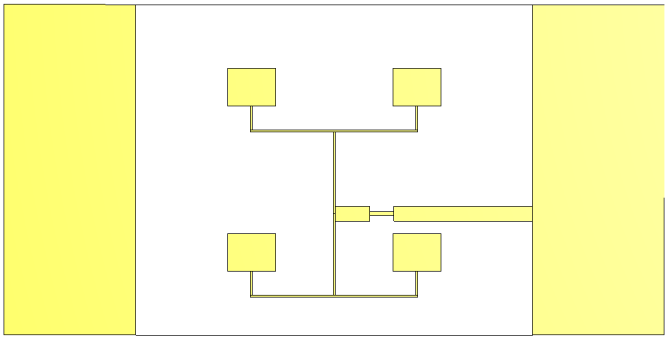

Figure 5.21: Array feeding network line 4.

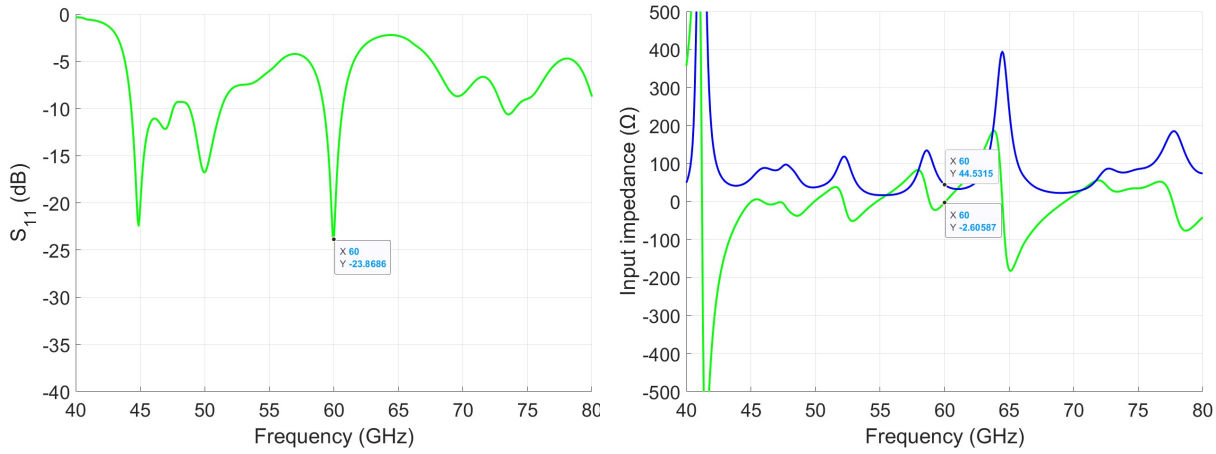

(a) S_{11}. (b) Impedance.

Figure 5.22: Array final feeding network.

5.4 Microstrip to CPW transition

Since the use of the CPW line is necessary for further practical application with the use of microprobes, in this section we explore the transition between the transmission line and CPW. Not many articles can be found on this matter but I would like to highlight [54] and [55] that helped with the design of the following transitions. Figure 5.23 shows the transitions mentioned in these articles. In both transitions, it is possible to obtain good results from ≈ 0 to 40 GHz.

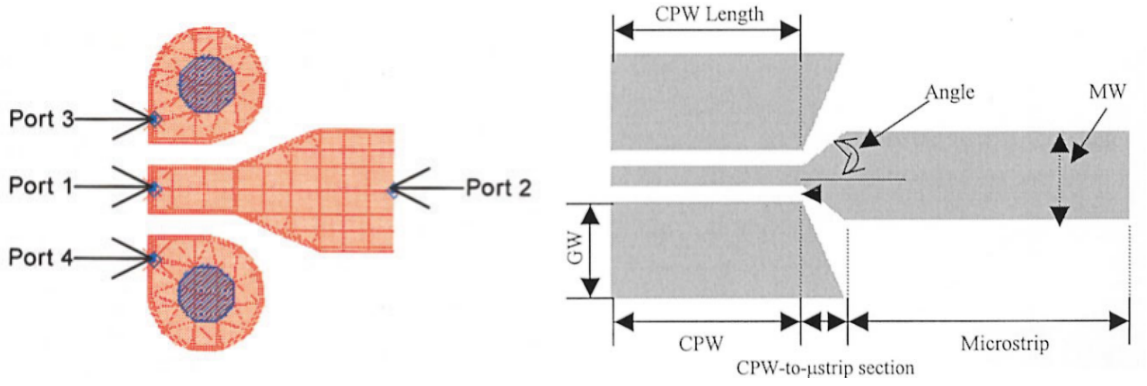

(a) [55]. (b) [54].

Figure 5.23: CPW transition to microstrip line.

Based on the layouts previously shown, two designs were tested for the microstrip-to-CPW transition. For an easier mention, let's call them circular transition and triangular

transition, visible in Figure 5.24. A parametric study was made considering three variable parameters, *dT* which represents the size of the transition, *Wgl* the size of the CPW ground planes and *dimCPW* the distance from the center to the CPW line.

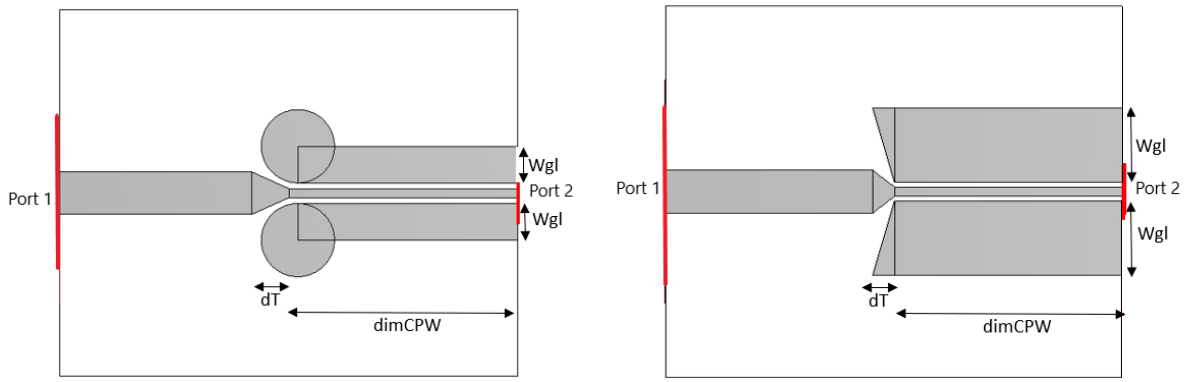

(a) Circular transition. (b) Triangular transition.

Figure 5.24: Microstrip line transition to CPW.

5.4.1 Circular transition

First, the circular transition is studied. In order to get a proper transition, the S-Parameters must all be in agreement, i.e. both S_{11} and S_{22} must be < -10 dB. This indicates that both lines are adapted to the port and there is no reflection of the signal in the frequency range. And both S_{21} and S_{12} must be in agreement with the reflection coefficients and near 0 dB.

The first parameter in study is the size of the transition *dT*. Figure 5.25 shows the S-Parameters for 0.2 mm, 0.4 mm and 0.6 mm. As it is visible, the increase of the transition dimension affects the S_{11} and S_{22} at certain frequencies, but overall it doesn't have a big impact on the structure performance. Figure 5.26 shows the variation of the side ground planes (*Wgl*) of the CPW. With the increase of the ground plane, there is a variation in the resonant frequency in the $\approx$ 30 to 60 GHz frequency band which decreases.

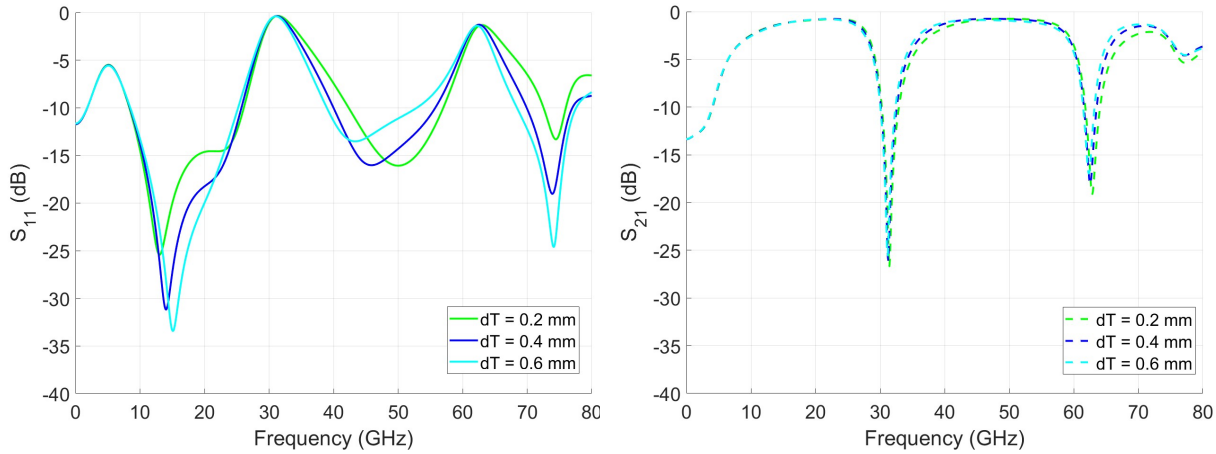

(a) S_{11}

(b) S_{21}.

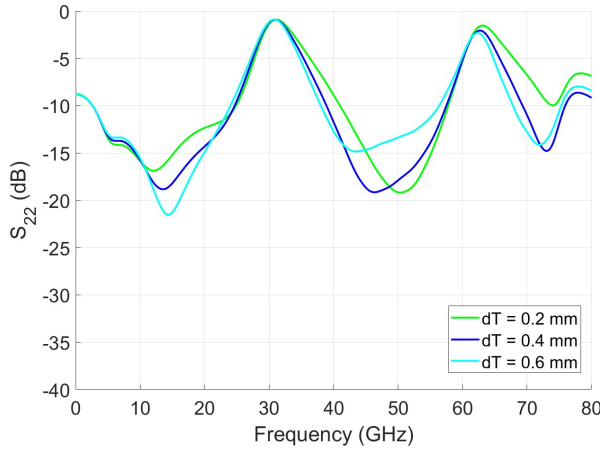

(c) S_{22}.

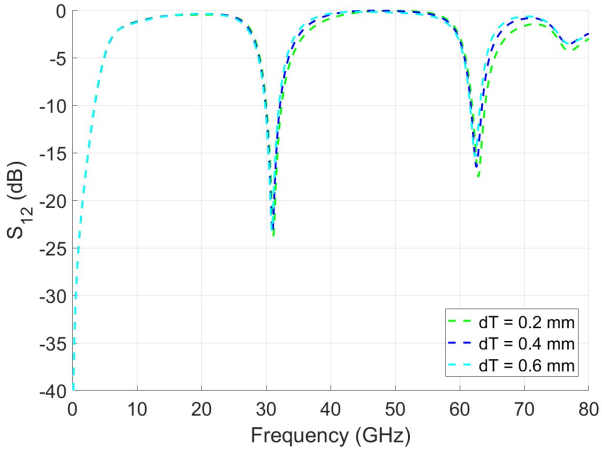

(d) S_{12}.

Figure 5.25: Impact of dT on the circular transition.

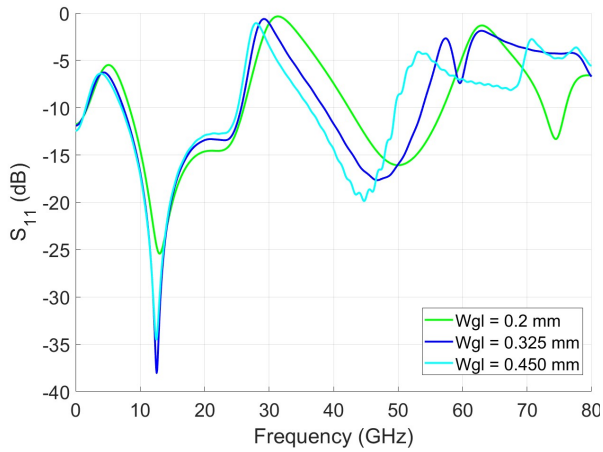

(a) S_{11}

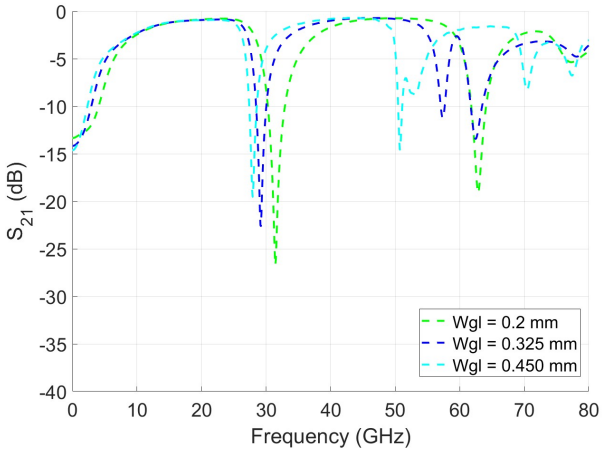

(b) S_{21}.

Figure 5.26: Impact of Wgl on the circular transition.

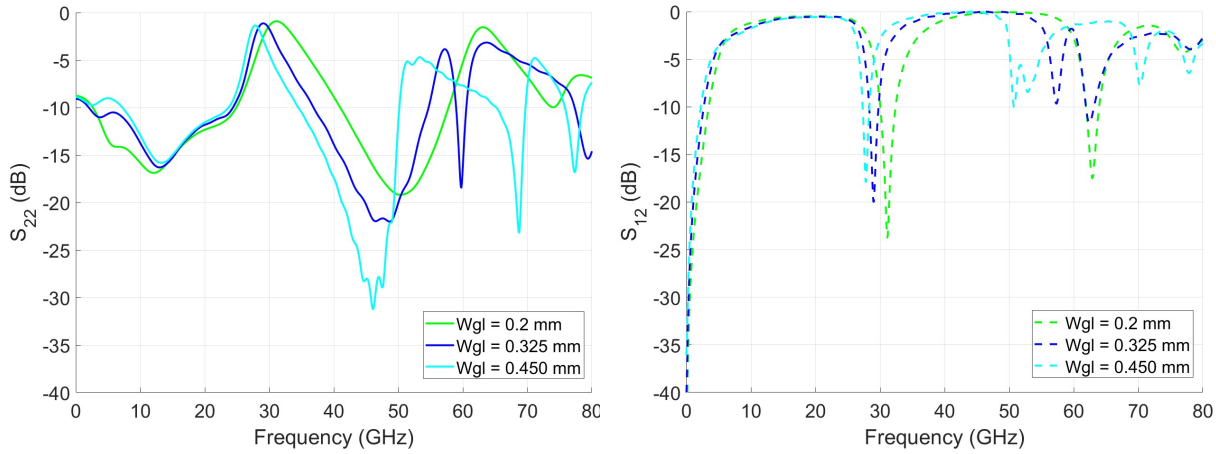

(c) S_{22}. (d) S_{12}.

Figure 5.26: Impact of *Wgl* on the circular transition.

The dimension of the CPW show to be the parameter that has a bigger impact in the S-Parameters as it is visible in Figure 5.27. With the decrease of the size of the CPW (*dimCPW* >) it was possible to increase the bands where the S_{11} and S_{22} were below -10 dB. However, this band ($\approx$ 10 to 40 GHz) does not cover the frequency of interest.

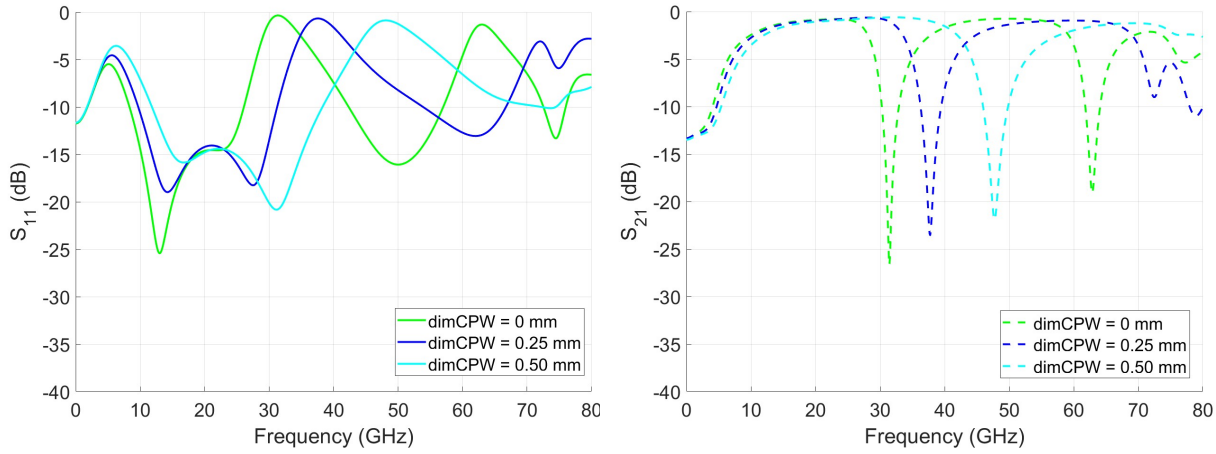

(a) S_{11} (b) S_{21}.

Figure 5.27: Impact of *dimCPW* on the circular transition.

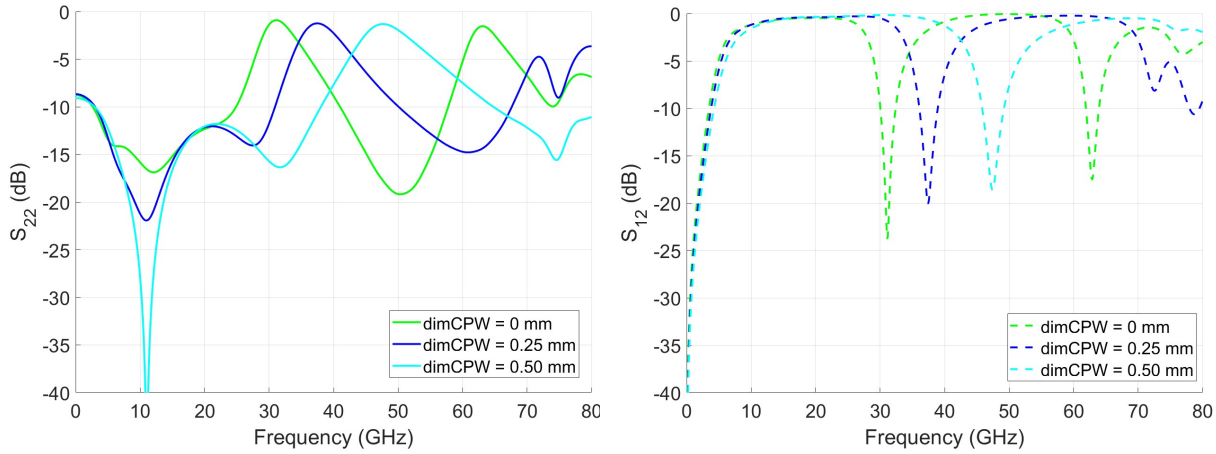

(c) S_{22}. (d) S_{12}.

Figure 5.27: Impact of *dimCPW* on the circular transition.

Considering the parametric study above, efforts were made to increase the bandwidth however, changing only the parameters in the study, it was not possible for this structure to get a bandwidth that covered the frequency spectrum shown especially around 60 GHz. So the study continued with the triangular transition.

5.4.2 Triangular transition

For the triangular transition, the same parametric study was performed starting with the size of the transition dT. In this transition, the increase of the dT affects the resonant frequency which decreases with the rise of the size dT as visible in Figure 5.28.

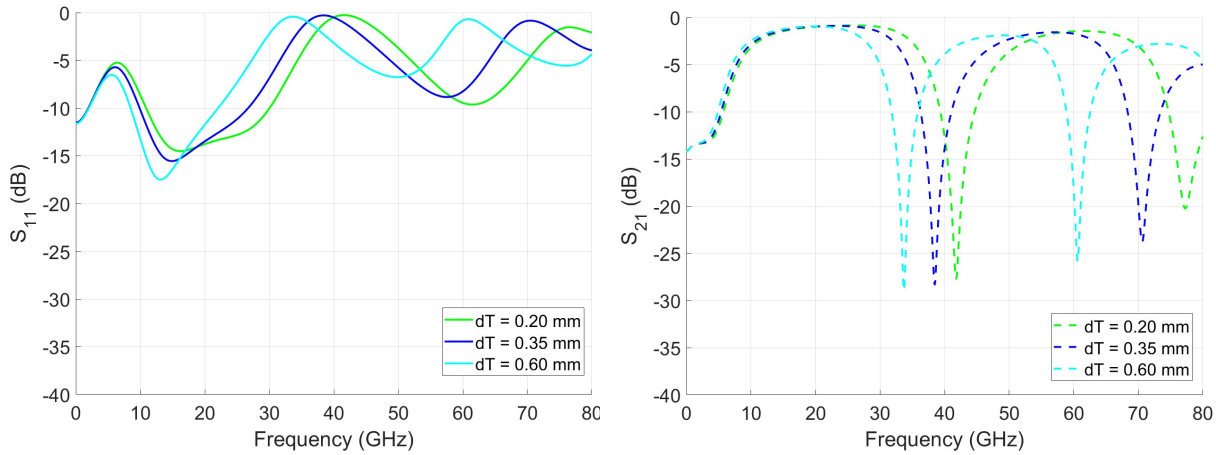

(a) S_{11} (b) S_{21}.

Figure 5.28: Impact of dT on the triangular transition.

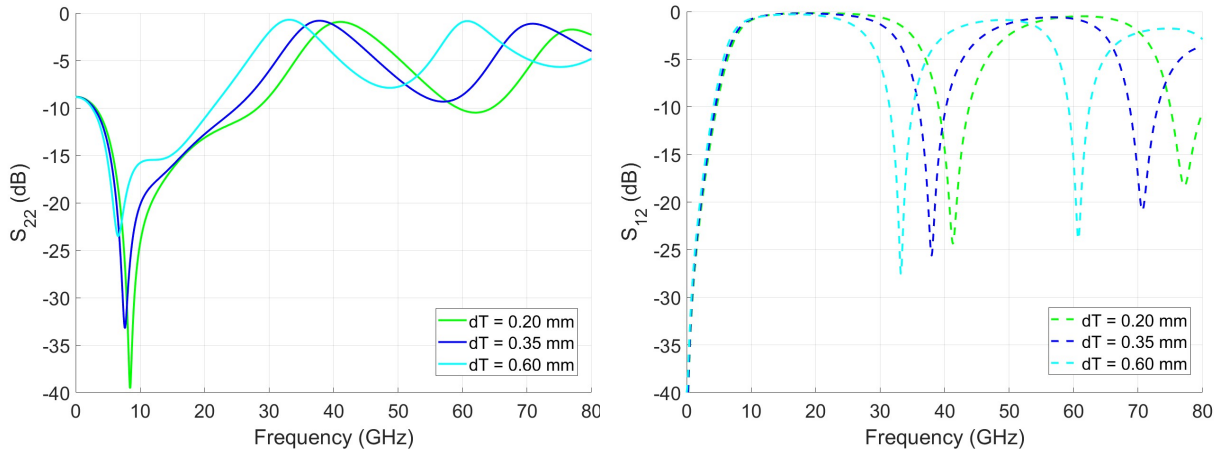

(c) S_{22}. (d) S_{12}.

Figure 5.28: Impact of dT on the triangular transition.

As for the ground plane width (*Wgl*) variation shown in Figure 5.29, the increase of this value increases the bandwidth of operation, and for the value 0.55 mm, the S_{11} and S_{22} are below -10 dB from $\approx$ 10 to 30 GHz and $\approx$ 50 to 70 GHz which is of great interest because it covers the 60 GHz band.

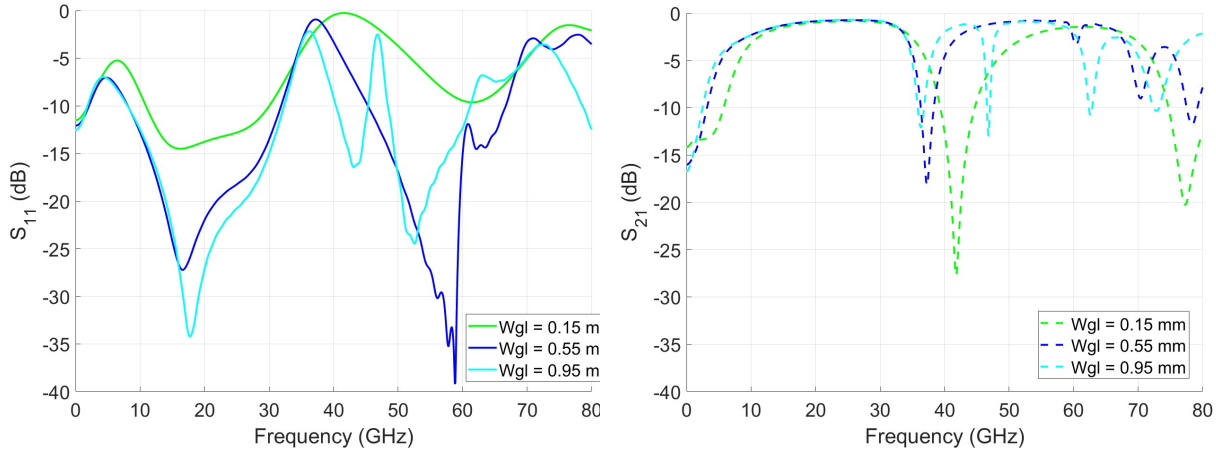

(a) S_{11} (b) S_{21}.

Figure 5.29: Impact of *Wgl* on the triangular transition.

The parameter *dimCPW*, showed to be of great interest aswell because it increased the bandwidth of operation. Although the S_{11} and S_{22} are not far below -10 dB, as we can see in Figure 5.30, the bandwidth increased significantly, almost covering up to 20 GHz.

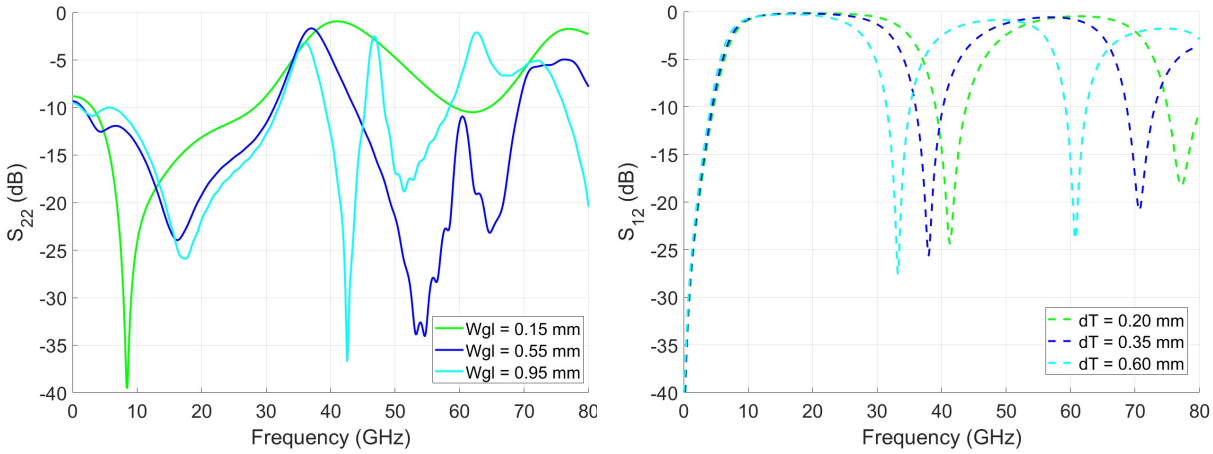

(c) S_{22}. (d) S_{12}.

Figure 5.29: Impact of *Wgl* on the triangular transition.

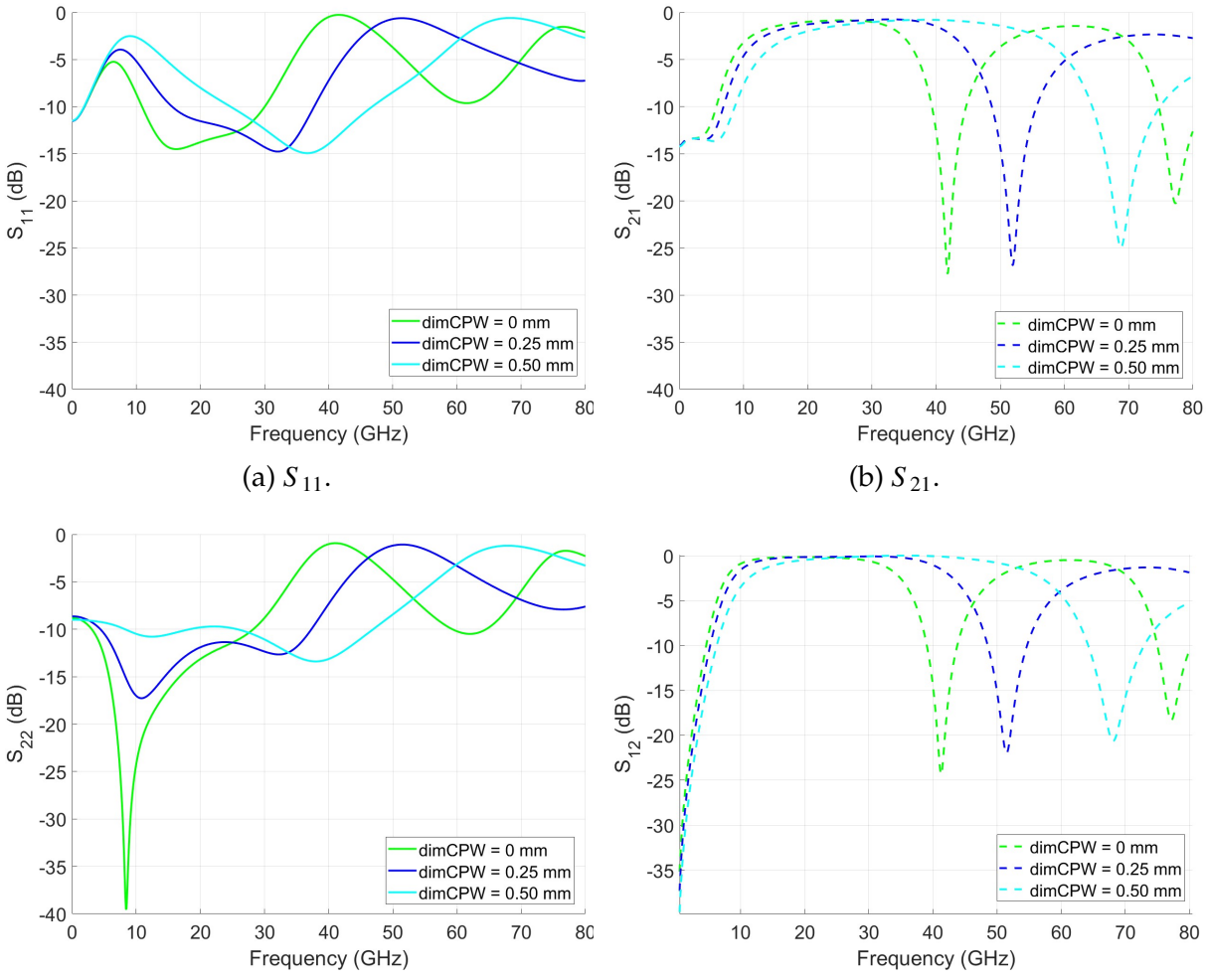

(a) S_{11}. (b) S_{21}.

(c) S_{22}. (d) S_{12}.

Figure 5.30: Impact of *dimCPW* on the triangular transition.

In conclusion, the parameters in question showed to have a bigger impact on the triangular transition with some of the simulations covering the interest band of 60 GHz.

5.4.3 Final transition model

A few adjustments were made on the triangular transition where it was possible to obtain a bandwidth of 56.3 GHz and 70 GHz for the S_{11} and S_{22}, respectively. Figure 5.31, presents the S-Parameters for the triangular transition and Table 5.7 the final values for the *dT*, *Wgl* and *dimCPW*.

Table 5.7: Final parameter values for triangular transition.

Parameters	Value (mm)
dT	0.1
Wgl	0.4
dimCPW	0.75

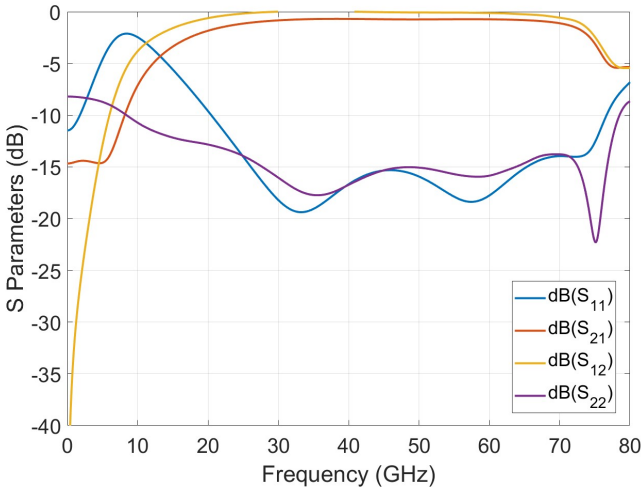

Figure 5.31: S-Parameters final transition.

5.5 Final Array

After studying the transition between the transmission line and the CPW line the same was implemented in the array, obtaining the final antenna array visible in Figure 5.32 with 10x5 mm^2 ground plane and 6x5 mm^2 substrate. The array input match, visible in Figure 5.33, was -24.6 dB at 60 GHz and bandwidth of 1.5 GHz.

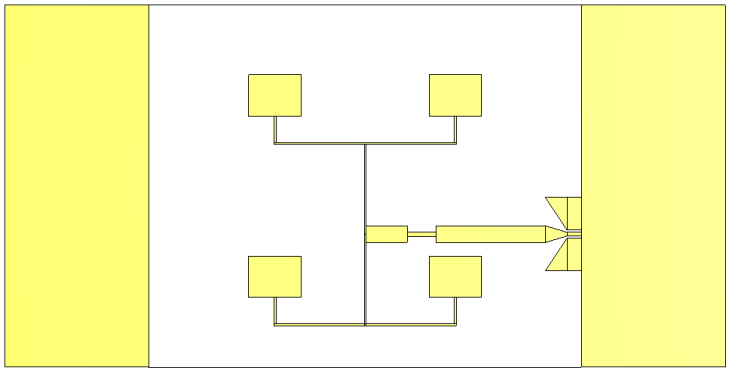

Figure 5.32: Array with Microstrip to CPW transition.

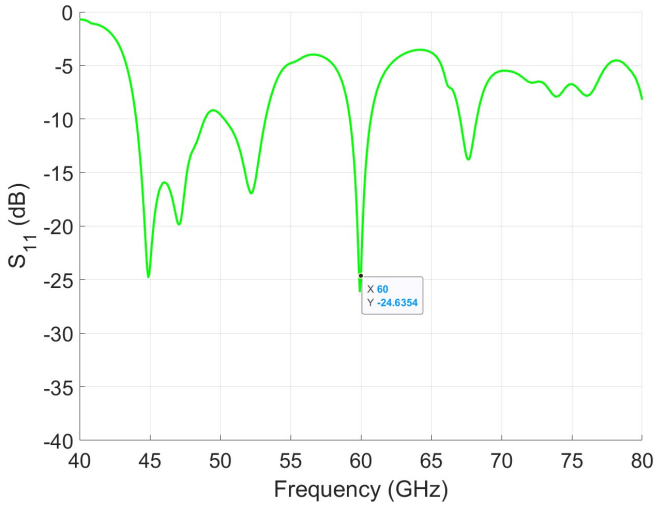

Figure 5.33: S_{11} Array with Microstrip to CPW transition.

The normalized radiation pattern was also observed and compared with the array without feeding network, studied in section 5.2, in Table 5.8. The array with a feeding network has a more narrow angular width and bigger side lobe level Figure 5.34 shows the 2D radiation pattern in both $\phi = 0°$ and $\phi = 90°$ planes.

Table 5.8: Comparison between the array fed with the discrete port and transmission line transition to CPW.

	Angular width (Degree)		Gain (dBi)	Side lobe level (dB)	
	$\phi = 0$	$\phi = 90$	——	$\phi = 0$	$\phi = 90$
Array without feeding network	53.6	45.6	10.28	-11.2	-8.3
Array with feeding network	42.8	44.8	10.17	-7.9	-7.7

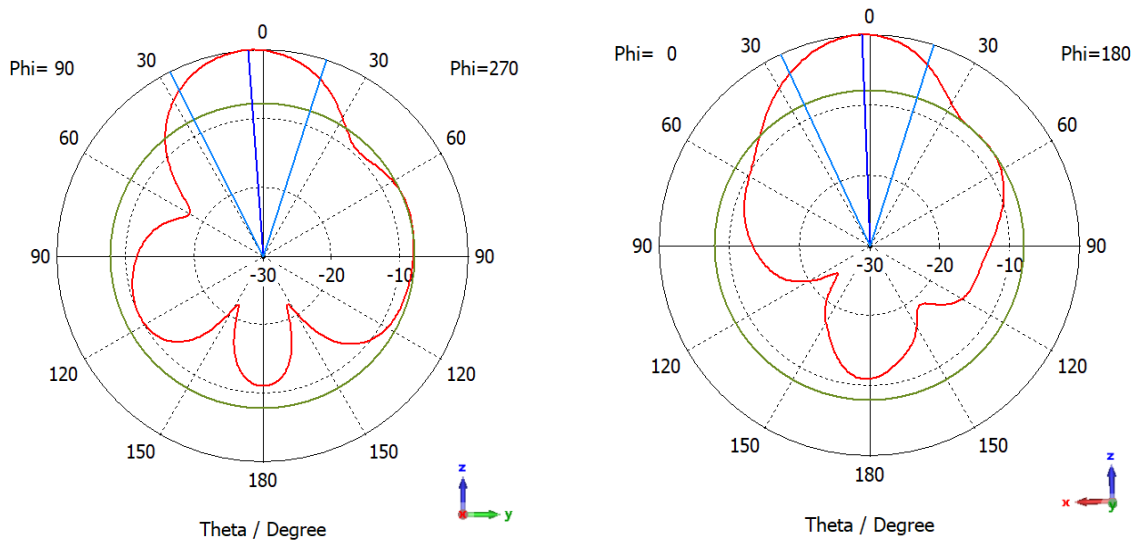

(a) $\phi = 90°$. (b) $\phi = 0°$.

Figure 5.34: Normalized radiation pattern of the array with microstrip to CPW transition.

According to the stack layer provided by the manufacturer, it was necessary to implement a 2 µm silicon nitride between the silicon substrate and the conductor layers. So two layers were implemented in the original array design. The silicon nitride characteristics are present in Table 5.9.

Table 5.9: Silicon Nitride characteristics.

Parameters	Value
Permittivity	7.8
Loss tan	0.0004
Height	2 µm

Also, the pitch of the contacts of the probe (distance between the contacts), that are going to be used in the posterior phase of this dissertation, is 150 µm. So, it was necessary to adjust the CPW line to respect this and still get the wanted 50 Ω. After making some adjustments to the transition it was possible to obtain an input match of -23.8 dB, visible in Figure 5.35.

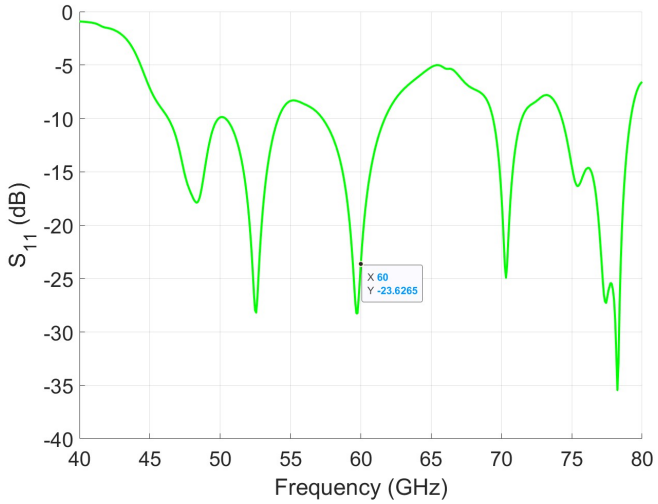

Figure 5.35: S_{11} of the array with silicon nitride layers.

As mentioned earlier, the ground plane is bigger than the whole structure to emulate the presence of a bigger metallic structure behind the antenna. With the previous simulations, it was concluded that this had a minor impact on the input match of the microstrip patch antenna. In this phase, the antenna array design is concluded, so before submitting the antenna design for fabrication the ground plane was reduced to the substrate dimensions of 6x5 mm^2. The array dimensions are present in Figure 5.36, to facilitate the reader's understanding of all dimensions.

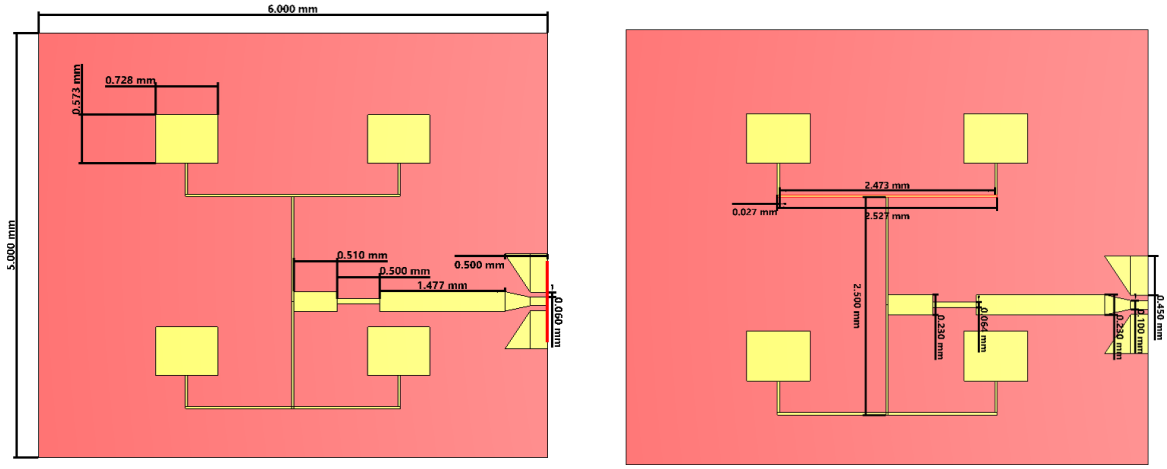

(a) 1. (b) 2.

Figure 5.36: Array dimensions.

Figure 5.37, shows the input match after reducing the size of the ground plane. It is visible that this doesn't impact the resonant frequency at 60 GHz but, lowers the S_{11} value for other frequencies, particularly for 53 GHz.

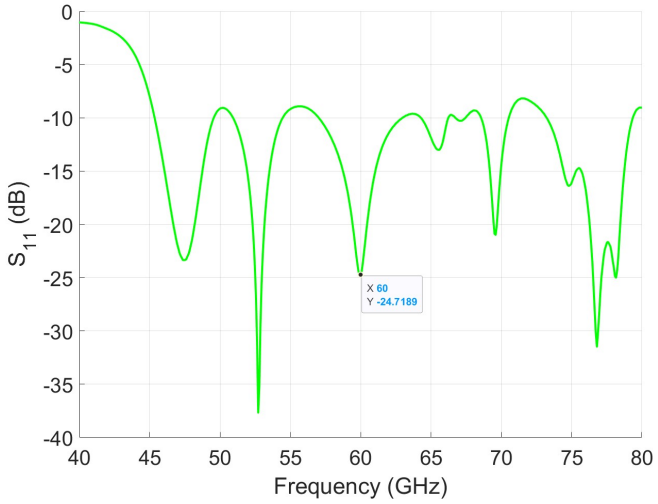

Figure 5.37: S_{11} of the final array.

The normalized 2D radiation pattern is visible in Figure 5.38 and 3D radiation pattern in Figure 5.39. In the final array design, it was possible to achieve an angular width of 44.4º and 49º on the principal planes, slightly bigger than with the bigger ground plane, a maximum gain of 8.5 dBi, and an efficiency of 85.5%. These characteristics are summarized in Table 5.10.

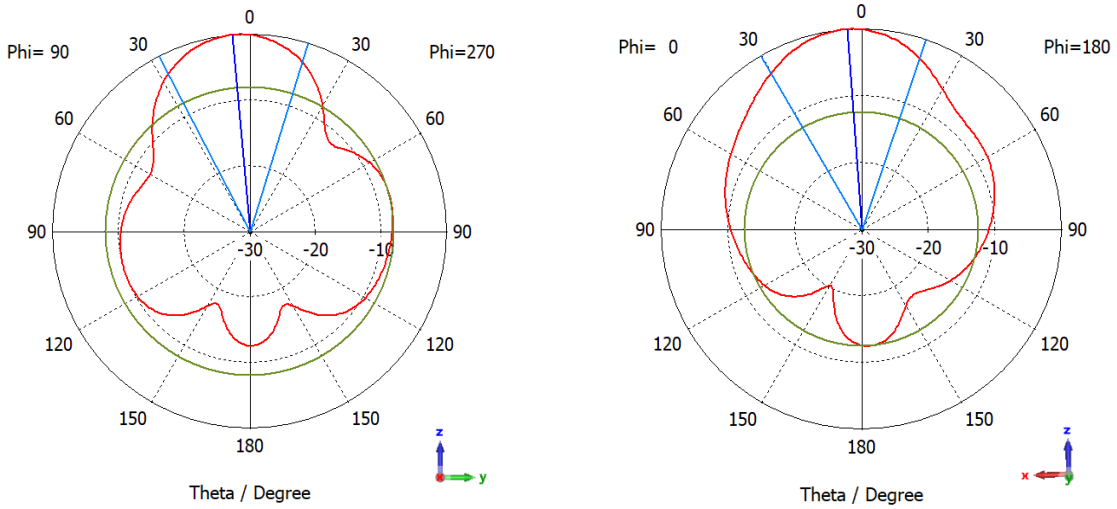

(a) $\phi = 90°$. (b) $\phi = 0°$.

Figure 5.38: Normalized radiation pattern of the final array.

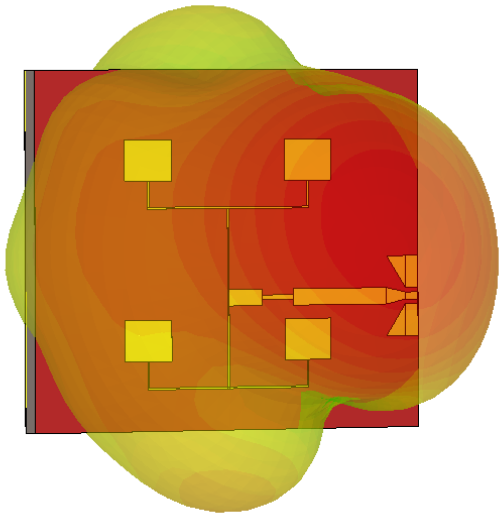

Figure 5.39: 3D radiation pattern of the final array.

Table 5.10: Array overall performance.

Parameters	Value
S11	- 24.7 dB
Gain	8.5 dBi
Efficiency	85.5%
Bandwidth	5.78 GHz

Four antennas were built, to evaluate the antenna design but also the possibility of having any manufacturing errors. The antennas are present in Figure 5.40 with a 1-cent coin for scale.

Figure 5.40: Antennas under test.

5.6 Antenna Array Measurement

The OCA was built and subsequently tested at the Instituto de Telecommunications de Aveiro using a Probe Station and VNA (Vector Network Analyzer). During the antenna evaluation, it was necessary to understand the problems associated with the setup. Conventional connector-based methods on an anechoic chamber cannot be used unless the chip is mounted on a PCB, complicating the antenna's performance accuracy. So, an RF-probe base setup is used to measure the antenna S_{11}. This chapter will explain the setup, the process of testing the OCA and the conclusions drawn from the observations made in the laboratory will be explained in this chapter.

5.6.1 Measurement Setup

The OCA was built and later tested in Instituto de Telecomunicações de Aveiro. When testing the OCA it is important to know that there are some challenges associated with the measuring setup. Conventional testing setups, using SMA connectors are a possibility, however, working with relatively small antennas can require the antenna's placement on a PCB which further complicates the accurate characterization of the antenna performance [56]. A simpler way to test the antenna is to resort to the use of RF-probes to measure the antenna input match in a probe station. However, when using this method there is a possibility of unwanted coupling between the antenna and the measurement equipment which can cause considerable discrepancies in the measured results of the antenna [56]. The probe body consists of a large conducting part that not only radiates itself but also tends to block and reflect the antenna radiation resulting in a distorted radiation pattern measurement. For this dissertation, only the reflection coefficient will be tested in a probe station to understand if it is possible to evaluate the antenna S_{11} and the measurement of the gain and radiation pattern will be included in future work. In Figure 5.41a is present the probe station used for the measurements and in Figure 5.41b the RF-probe. For a comprehensive summary of the equipment used and the model reference, please refer to Table 5.11.

Table 5.11: Materials used for practical measurements.

Materials	Model Reference
VNA	Anritsu MS4647B
Cable	415-0537-M1.0
Probe	Cascade Microtech Inc PQ2D6
Probe Station	Cascade Microtech 9000

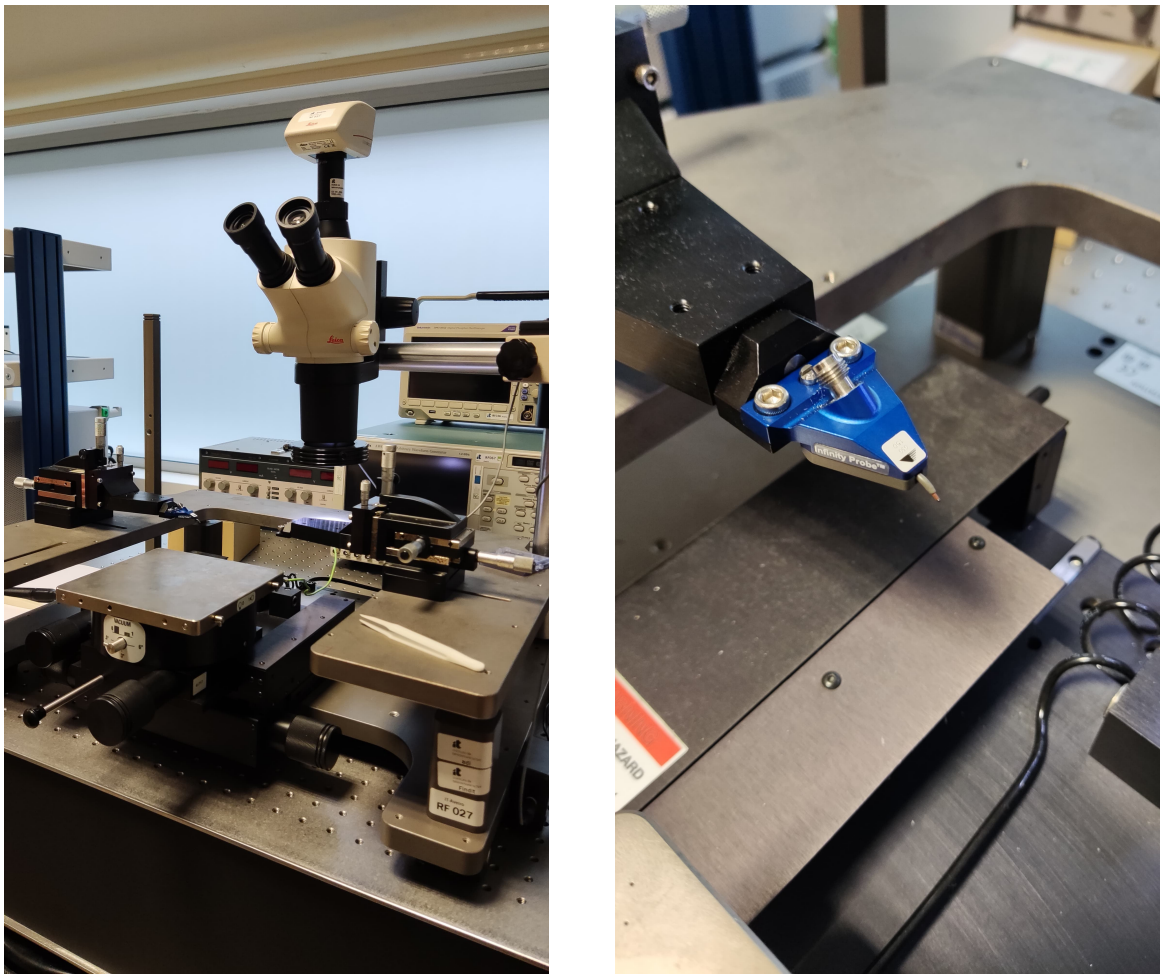

(a) Probe Station. (b) RF-Probe.

Figure 5.41: Setup equipment.

Probe alignment and calibration

Before performing measurements with the antenna it is necessary to align and calibrate the probe. First, the alignment or planarization of the RF probe is made. This procedure is made to ensure that there is no tilt associated with the RF probe and ensure all contacts are at the same height preventing the probe from being damaged. Figure 5.42 shows the contact substrate needed to make this procedure. It is important to adjust planarity until equal marks from all probe contacts on the contact substrate.

After securing that all of the contacts are in position, the contact substrate is replaced by a calibration substrate present in Figure 5.43. This substrate contains short, open, and 50 Ω loads and the contacts of the RF-Probe must align with these G-S-G lines to ensure proper calibration of the system and guarantee minimal loss and secure feasibility in the results measured.

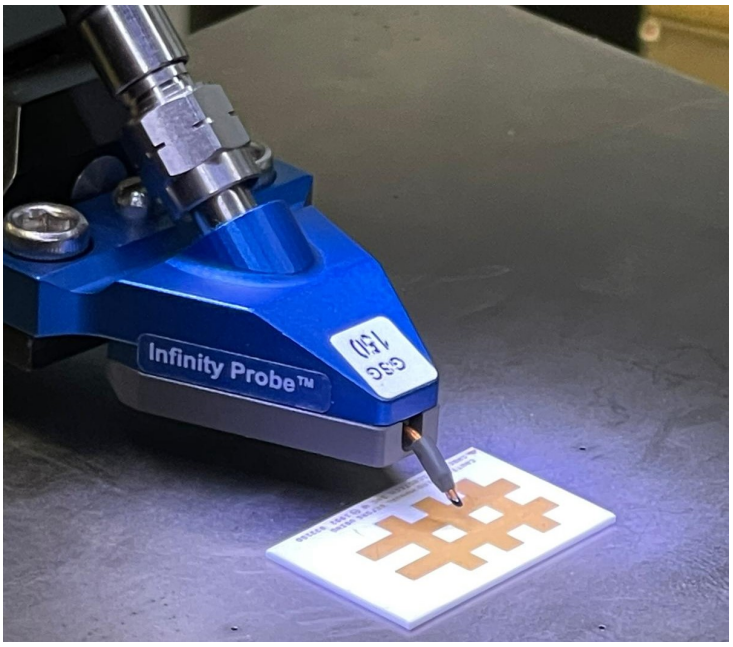

Figure 5.42: Contact substrate.

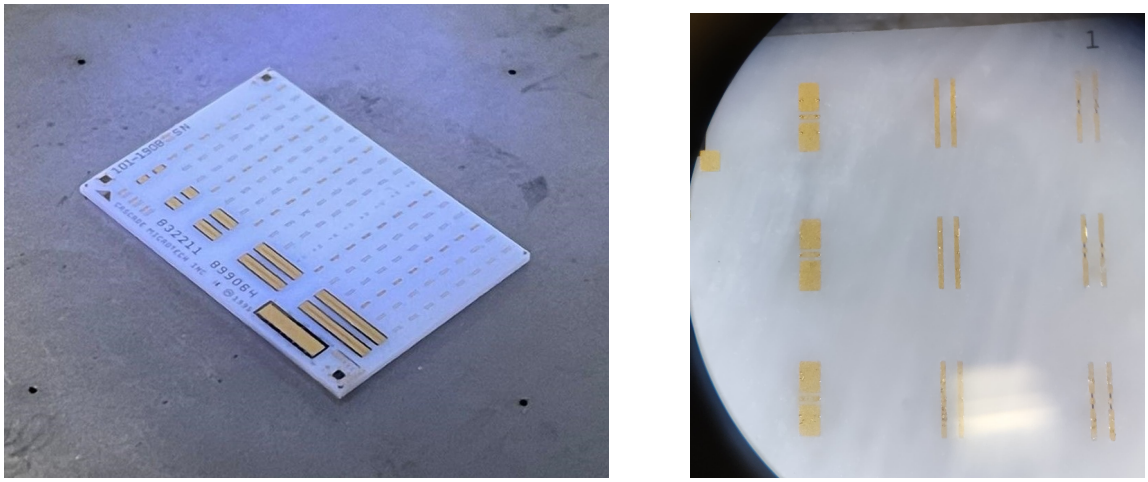

(a) Substrate. (b) Microscope view.

Figure 5.43: Calibration substrate.

5.6.2 Input Match Measurements

After ensuring all the conditions for the tests, the antenna was placed on the probe dish, as shown in Figure 5.44, to measure the reflection coefficient. This dish has a vacuum mechanism to ensure that the devices placed on it do not move minimizing the risk of breaking any equipment or damaging the device under test.

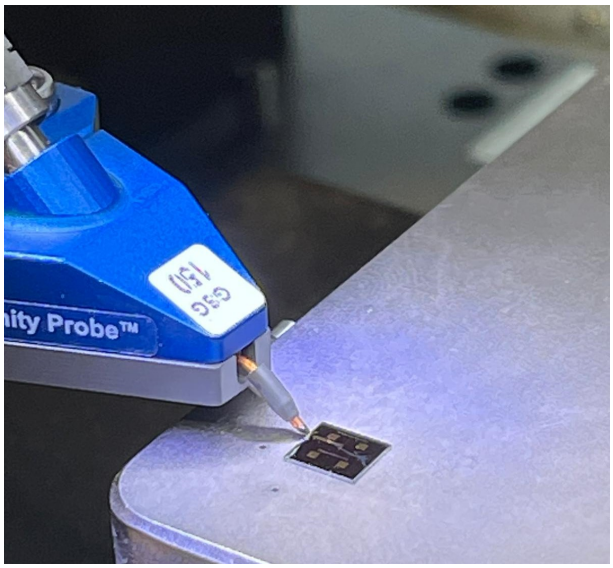

Figure 5.44: Antenna placement on the probe station.

The S_{11} of the four antennas was measured in a VNA and the results can be observed in Figure 5.45. The frequency range chosen for the measurements was from 53 GHz to 67 GHz. As can be seen, the measured antennas are slightly detuned from the target 60 GHz. Also, the input match is below -10 dB from 53 to approximately 62 GHz for all four antennas. Given the range used to measure the antennas, it is not possible to conclude with certainty the bandwidth of the antennas. Since these measurements require a time-consuming process, these four measurements are used to validate this measurement technique and the antenna design in terms of input match and other measurements will be required to measure the bandwidth, gain, efficiency, and radiation pattern.

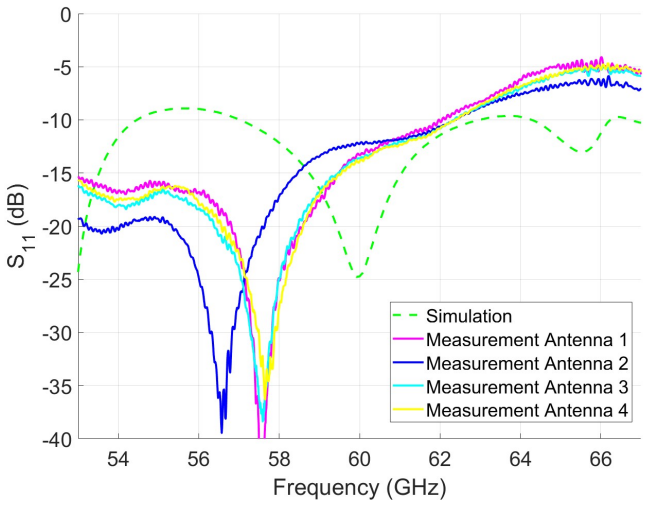

Figure 5.45: S_{11} comparison between simulation and measured results.

6

Conclusions and Future work

This thesis's main goal was to design an antenna that would serve the purpose of an OCA at 60 GHz considering all the problems associated when building this kind of antenna and present a simple design i.e without appealing to more complex methods like the ones presented in the state of the art.

Chapter 2 presents an overview of OCAs for the millimeter-wave and terahertz bands. The interest in these bands arises from the demand for high capacity due to technological advancements and IoT devices, supporting applications with extreme data rates. By implementing an OCA, not only can device interconnectivity be achieved, but also network sustainability through environmentally-friendly solutions. However, designing an OCA presents challenges such as antenna integration in high permittivity substrates, interference with other components, propagation losses at high frequencies, and more. To enhance antenna performance, several techniques are discussed in the literature.

In Chapter 3, the folded slot antenna was designed, and an analysis of the impact of permittivity on this structure was conducted, addressing one of the challenges associated with OCA design. To direct the antenna's radiation towards the intended direction ($\theta = 0°$), a ground plane is introduced. However, the introduction of the ground plane transforms the structure into a resonant cavity, imposing limitations on structural dimensions and the antenna's mode of operation. Despite these challenges, the design manages to achieve good adaptation and a directive radiation pattern with an InP substrate, achieving a bandwidth of 314 MHz, with a maximum gain of 8.5

dBi, half-power beamwidths of 25.3º and 46.8º in the two principal planes, and an efficiency of 51%. However, since the antenna operates in a mode other than the first mode, nearby modes can potentially interfere with antenna performance.

Building upon the conclusions drawn in the previous chapter, Chapter 4 explores the potential of a microstrip antenna as a solution for OCA applications. The microstrip antenna is meticulously designed, taking into account the constraints of chip dimensions. This antenna demonstrates favorable results, achieving a directive radiation pattern and good adaptation outperforming the folded slot antenna in terms of bandwidth and efficiency achieving a bandwidth of 1.39 GHz with a maximum gain of 5.45 dBi, half power beamwidth of 123.9º and 92.1º in the two principal planes, and an efficiency of 95.5%.

Furthermore, the substrate material is transitioned from InP to silicon, due to the availability of the material. However, this transition introduces new challenges due to higher thickness and resistivity. These constraints, which are explored in this chapter, require the microstrip design on silicon to be limited to a maximum substrate thickness of 300 μm and have high resistivity. The microstrip antenna on a silicon substrate achieved a 2.18 GHz bandwidth, 5.28 dBi maximum gain, a half power beamwidth of 124.1º and 107.9º in the two principal planes, and an efficiency of 89%.

In Chapter 5, a 2x2 microstrip patch array was designed aiming to enhance antenna performance. To construct the array, it was essential to study the design of the feeding network and the transition between the transmission line and CPW. Ultimately, the array successfully increased directivity and improved gain achieving a bandwidth of 5.78 GHz, a gain of 8.5 dBi with 42.7º and 42.6º half power beamwidth on the principal planes, and an efficiency of 85.5% This dissertation concludes with the measurements of four array prototypes built. The input match of these four antennas was measured and the results revealed that the antennas are slightly detuned from the target 60 GHz.

Future work

OCA is a topic of some complexity and therefore there is still much to explore in this subject so for future work, some of the following topics are suggested:

- To measure the radiation pattern it is necessary to study a possible alternative to the limited setup used to measure the antenna input match. One alternative is to place the antenna on a PCB and connect the feed line using bond wires. This would also require the design of the bond wire compensation circuit;

- Explore the 'One antenna gain measurement' as a possibility to measure the antenna gain without using the other antennas;
- The simulation bandwidth achieved was small so techniques to improve it should also be investigated;
- Some research must also be done to understand why the best input match is below the target frequency as well as understand why the input match level is better than expected;

References

[1] H. M. Cheema and A. Shamim, "The last barrier: On-chip antennas", *IEEE Microwave Magazine*, no. 1, pages 79–91, Jan. 2013.

[2] Takaaki Kakitsuka, Koichi Hasebe, Takuro Fujii, Tomonari Sato, Koji Takeda, and Shinji Matsuo, "InP-based membrane optical devices for large-scale photonic integrated circuits", *NTT Technical Review*, no. 5, page 6, 2015.

[3] Ali Hajimiri, "Mm-wave silicon ICs: Challenges and opportunities", *IEEE 2007 Custom Intergrated Circuits Conference (CICC)*, pages 741–747, 2007.

[4] ITU-R, "Attenuation by atmospheric gases", *Electronic Publication Geneva*, page 25, 2016.

[5] Chris Koh, "The benefits of 60 GHz unlicensed wireless communications", page 7, 2001.

[6] Josef Buechler, Erich Kasper, Peter Russers, Enior Membeire, and Karl M Strohm, "Silicon high-resistivity-substrate millimeter-wave technology", *Microwave and Millimeter-Wave Monolithic Circuits*, pages 93–97, 1986.

[7] N. Camilleri and B. Bayraktaroglu, "Monolithic millimeter-wave IMPATT oscillator and active antenna", in *1988., IEEE MTT-S International Microwave Symposium Digest*, IEEE, 1988, pages 955–958.

[8] Constantine A. Balanis, *Antenna Theory: Analysis and Design*. Wiley, 2015.

[9] Shun-Sheng Hsu, Kuo-Chih Wei, Cheng-Ying Hsu, and Huey Ru-Chuang, "A 60-GHz millimeter-wave CPW-fed yagi antenna fabricated by using 0.18- μm CMOS technology", *IEEE Electron Device Letters*, no. 6, pages 625–627, Jun. 2008.

[10] Wanlan Yang, Kaixue Ma, Kiat Seng Yeo, and Wei Meng Lim, "A 60ghz on-chip antenna in standard CMOS silicon technology", in *2012 IEEE Asia Pacific Conference on Circuits and Systems*, IEEE, Dec. 2012, pages 252–255.

[11] Y P Zhang, M Sun, and L H Guo, "On-chip antennas for 60-GHz radios in silicon technology", *IEEE TRANSACTIONS ON ELECTRON DEVICES*, no. 7, page 5, 2005.

[12] C.-C. Lin, S.-S. Hsu, C.-Y. Hsu, and H.-R. Chuang, "A 60-GHz millimeter-wave CMOS RFIC-on-chip triangular monopole antenna for WPAN applications", in *2007 IEEE Antennas and Propagation Society International Symposium*, IEEE, Jun. 2007, pages 2522–2525.

[13] F. Gutierrez, S. Agarwal, K. Parrish, and T.S. Rappaport, "On-chip integrated antenna structures in CMOS for 60 GHz WPAN systems", *IEEE Journal on Selected Areas in Communications*, no. 8, pages 1367–1378, Oct. 2009.

[14] Shivam Upadhyay and Shweta Srivastava, "A 60-GHz on-chip monopole antenna using silicon technology", page 2, 2013.

[15] Benjamin Goettel, Stefan Malz, and Thomas Zwick, "Active multiple feed on-chip antennas with efficient in-antenna power combining operating at 200–320 GHz", *IEEE TRANSACTIONS ON ANTENNAS AND PROPAGATION*, no. 2, page 8, 2017.

[16] Xiao-Dong Deng, Yihu Li, Hailin Tang, Wen Wu, and Yong-Zhong Xiong, "Dielectric loaded endfire antennas using standard silicon technology", *IEEE TRANSACTIONS ON ANTENNAS AND PROPAGATION*, no. 6, page 11, 2017.

[17] Hui Chu, Yong-Xin Guo, Teck-Guan Lim, Yee Mong Khoo, and Xiangquan Shi, "135-GHz micromachined on-chip antenna and antenna array", *IEEE TRANSACTIONS ON ANTENNAS AND PROPAGATION*, no. 10, page 7, 2012.

[18] Jeong-Geun Kim, Hyung Suk Lee, Ho-Seon Lee, Jun-Bo Yoon, and S. Hong, "60-GHz CPW-fed post-supported patch antenna using micromachining technology", *IEEE Microwave and Wireless Components Letters*, no. 10, pages 635–637, Oct. 2005.

[19] S Keyrouz and D Caratelli, "Dielectric resonator antennas: Basic concepts, design guidelines, and recent developments at millimeter-wave frequencies", *International Journal of Antennas and Propagation*, pages 1–20, 2016.

[20] Yexi Song, Yunqiu Wu, Jie Yang, and Kai Kang, "The design of a high gain on-chip antenna for SoC application", *2015 IEEE MTT-S International Microwave Workshop Series on Advanced Materials and Processes for RF and THz Applications (IMWS-AMP)*, pages 1–3, 2015.

[21] Debin Hou, Wang-Ling Goh, and Mohammad Madihian, "130-GHz on-chip meander slot antennas with stacked dielectric resonators in standard CMOS technology", *IEEE TRANSACTIONS ON ANTENNAS AND PROPAGATION*, no. 9, page 8, 2012.

[22] Debin Hou, Yong-Zhong Xiong, Wei Hong, Wang Ling Goh, and Jixin Chen, "Silicon-based on-chip antenna design for millimeter-wave/THz applications", *2011 IEEE Electrical Design of Advanced Packaging and Systems Symposium (EDAPS)*, pages 1–4, 2011.

[23] Chun-Hsing Li and Te-Yen Chiu, "Single flip-chip packaged dielectric resonator antenna for CMOS terahertz antenna array gain enhancement", *IEEE Access*, pages 7737–7746, 2019.

[24] Zunnurain Ahmad, "On-chip dual-polarized dielectric resonator antenna for millimeter wave applications", *IEEE Antennas and Wireless Propagation Letters*, vol. 17, no. 10, pages 1769–1772, 2018.

[25] Chun-Hsing Li and Te-Yen Chiu, "340-GHz low-cost and high-gain on-chip higher order mode dielectric resonator antenna for THz applications", *IEEE TRANSACTIONS ON TERAHERTZ SCIENCE AND TECHNOLOGY*, no. 3, page 11, 2017.

[26] Aobo Li, Shreya Singh, and Dan Sievenpiper, "Metasurfaces and their applications", *Nanophotonics*, no. 6, pages 989–1011, Jun. 27, 2018.

[27] A.P. Feresidis, G. Goussetis, Shenhong Wang, and J.C. Vardaxoglou, "Artificial magnetic conductor surfaces and their application to low-profile high-gain planar antennas", *IEEE Transactions on Antennas and Propagation*, no. 1, pages 209–215, Jan. 2005.

[28] Liwen Jing, Corbett R. Rowell, Salahuddin Raju, Mansun Chan, R.D. Murch, and C. Patrick Yue, "Fabrication and measurement of millimeter-wave on-chip MIMO antenna for CMOS RFIC's", in *2016 IEEE MTT-S International Wireless Symposium (IWS)*, IEEE, Mar. 2016, pages 1–4.

[29] Rui Wu, Wei Deng, Shinji Sato, Takuichi Hirano, Ning Li, Takeshi Inoue, Hitoshi Sakane, Kenichi Okada, and Akira Matsuzawa, "A 60-GHz efficiency-enhanced on-chip dipole antenna using helium-3 ion implantation process", in *2014 44th European Microwave Conference*, IEEE, Oct. 2014, pages 108–111.

[30] Junfeng Xu and David S Ricketts, "Broadband w-band on-chip yagi antenna using superstrate for high efficiency and endfire radiation", *2014 Asia-Pacific Microwave Conference*, pages 360–362, 2014.

[31] Hua Zhu, Xiuping Li, Zhihang Qi, and Jun Xiao, "A 320 GHz octagonal shorted annular ring on-chip antenna array", *IEEE Access*, vol. 8, pages 84 282–84 289, 2020.

[32] Mohammad Alibakhshikenari, Naser Ojaroudi Parchin, Bal Singh Virdee, Chan Hwang See, Raed A. Abd-Alhameed, Francisco Falcone, and Ernesto Limiti, "High performance metasurface-based on-chip antenna for terahertz integrated circuits", in *2020 Third International Workshop on Mobile Terahertz Systems (IWMTS)*, Essen, Germany: IEEE, Jul. 2020, pages 1–4.

[33] Hao Tian Huang, Bo Yuan, Xiao Hong Zhang, Zhi Fang Hu, and Guo Qing Luo, "A circular ring-shape monopole on-chip antenna with artificial magnetic conductor", in *2015 Asia-Pacific Microwave Conference (APMC)*, IEEE, Dec. 2015, pages 1–3.

[34] Francesco Giuppi, Haiqiang Sheng, Chuan Men, Ivan Russo, Renato Lombardi, and Maurizio Mattivi, "Substrate integrated waveguide-oriented design applied to the antenna section of mm-w communication systems: Challenges and advantages", in *2019 IEEE MTT-S International Wireless Symposium (IWS)*, IEEE, May 2019, pages 1–3.

[35] Xiao-Dong Deng, Yihu Li, Wen Wu, and Yong-Zhong Xiong, "340-GHz SIW cavity-backed magnetic rectangular slot loop antennas and arrays in silicon technology", *IEEE Transactions on Antennas and Propagation*, no. 12, Dec. 2015.

[36] Xiuping Li, Jun Xiao, Zihang Qi, and Hua Zhu, "Broadband and high-gain millimeter-wave and terahertz antenna arrays", in *2019 International Conference on Microwave and Millimeter Wave Technology (ICMMT)*, IEEE, May 2019, pages 1–3.

[37] Xiao-Dong Deng, Yihu Li, Chao Liu, Wen Wu, and Yong-Zhong Xiong, "340 GHz on-chip 3-d antenna with 10 dBi gain and 80% radiation efficiency", *IEEE Transactions on Terahertz Science and Technology*, no. 4, pages 619–627, Jul. 2015.

[38] Mohammad Alibakhshikenari, Bal S. Virdee, Ayman Abdulhadi Althuwayb, Sonia Aïssa, Chan H. See, Raed A. Abd-Alhameed, Francisco Falcone, and Ernesto Limiti, "Study on on-chip antenna design based on metamaterial-inspired and substrate-integrated waveguide properties for millimetre-wave and THz integrated-circuit applications", *Journal of Infrared, Millimeter, and Terahertz Waves*, no. 1, pages 17–28, Jan. 2021.

[39] Mohammad Alibakhshikenari, Bal S. Virdee, Chan H. See, Raed A. Abd-Alhameed, Francisco Falcone, and Ernesto Limiti, "High-gain metasurface in polyimide on-chip antenna based on CRLH-TL for sub-terahertz integrated circuits", *Scientific Reports*, no. 1, page 4298, Dec. 2020.

[40] Mohammad Alibakhshikenari, Bal S. Virdee, Chan H. See, Raed A. Abd-Alhameed, Francisco Falcone, and Ernesto Limiti, "Silicon-based 0.450-0.475 THz series-fed double dielectric resonator on-chip antenna array based on metamaterial properties for integrated-circuits", in *2019 Thirteenth International Congress on Artificial Materials for Novel Wave Phenomena (Metamaterials)*, IEEE, Sep. 2019, pages X–026–X–028.

[41] Mohammad Alibakhshikenari, Bal S. Virdee, Ayman A. Althuwayb, Ernesto Limiti, and Dion Mariyanayagam, "Compact and low-profile on-chip antenna using underside electromagnetic coupling mechanism for terahertz front-end transceivers", *Electronics*, no. 11, page 1264, May 25, 2021.

[42] Jiantong Li and Nima Ghalichechian, "Suspended highly-efficient on-chip phased array antenna at 60 ghz", *2019 IEEE International Symposium on Antennas and Propagation and USNC-URSI Radio Science Meeting*, pages 2195–2196, 2019.

[43] Sanjukta Mandal, Sujit Kumar Mandal, and Ashis Kumar Mal, "On-chip antennas using standard CMOS technology: A brief overview", in *2017 International Conference on Innovations in Electronics, Signal Processing and Communication (IESC)*, IEEE, Apr. 2017, pages 74–78.

[44] Robert C. Daniels, James N. Murdock, Theodore S. Rappaport, and Robert W. Heath, "60 GHz wireless: Up close and personal", *IEEE Microwave Magazine*, no. 7, pages 44–50, Dec. 2010.

[45] Hongwei Zhao, Sergio Pinna, Fengqiao Sang, Bowen Song, Simone Tommaso Suran Brunelli, Larry A. Coldren, and Jonathan Klamkin, "High-power indium phosphide photonic integrated circuits", *IEEE Journal of Selected Topics in Quantum Electronics*, no. 6, pages 1–10, Nov. 2019.

[46] Haruichi Kanaya, Masahiko Koga, Kota Tsugami, Guan Chai Eu, and Kazutoshi Kato, "4x4 planar array antenna on indium phosphide substrate for 0.3-THz band application", presented at the SPIE OPTO, Laurence P. Sadwick and Tianxin Yang, Eds., Feb. 24, 2017, 101031N.

[47] Jian Yu and Guoqing Luo, "A novel cavity-backed slot antenna on InP", in *2015 IEEE 16th International Conference on Communication Technology (ICCT)*, IEEE, Oct. 2015, pages 252–254.

[48] Khalid Hamed Alharbi, Ata Khalid, Afesomeh Ofiare, Jue Wang, and Edward Wasige, "Diced and grounded broadband bow-tie antenna with tuning stub for resonant tunnelling diode terahertz oscillators", *IET Microwaves, Antennas & Propagation*, no. 3, pages 310–316, Feb. 2017.

[49] Yunfeng Dong, Tom K. Johansen, and Vitaliy Zhurbenko, "On-chip patch antenna on InP substrate for short-range wireless communication at 140 GHz", in *2017 SBMO/IEEE MTT-S International Microwave and Optoelectronics Conference (IMOC)*, IEEE, Aug. 2017, pages 1–5.

[50] Wonseok Choe and Jinho Jeong, "A broadband THz on-chip transition using a dipole antenna with integrated balun", *Electronics*, no. 10, page 236, Oct. 5, 2018.

[51] Yong Li and Ruiliang Song, "A high gain on-chip terahertz antenna with high efficiency", in *2016 IEEE 9th UK-Europe-China Workshop on Millimetre Waves and Terahertz Technologies (UCMMT)*, IEEE, Sep. 2016, pages 222–224.

[52] Peng Lu, Thomas Haddad, Benedikt Sievert, Besher Khani, Sumer Makhlouf, Sebastian Dulme, Jose Fernandez Estevez, Andreas Rennings, Daniel Erni, Ullrich Pfeiffer, and Andreas Stohr, "InP-based THz beam steering leaky-wave antenna", *IEEE Transactions on Terahertz Science and Technology*, no. 2, pages 218–230, Mar. 2021.

[53] Fraunhofer. "Fraunhofer mpw run". (2023), [Online]. Available: https://www.hhi.fraunhofer.de/en/departments/pc/research-groups/photonic-inp-foundry/our-offer/prices.html.

[54] Guizhen Zheng, J. Papapolymerou, and M.M. Tentzeris, "Wideband coplanar waveguide RF probe pad to microstrip transitions without via holes", *IEEE Microwave and Wireless Components Letters*, vol. 13, no. 12, pages 544–546, Dec. 2003.

[55] M. C. Maya, A. Lázaro, P. DePaco, and L. Pradell, "A method for characterizing coplanar waveguide-to-microstrip transitions, and its application to the measurement of microstrip devices with coplanar microprobes", *Microwave and Optical Technology Letters*, vol. 39, no. 5, pages 373–378, Dec. 5, 2003.

[56] Hammad M. Cheema, Fatima Khalid, and Atif Shamim, *Antenna-on-Chip: design, challenges, and opportunities*. Boston London: Artech House, 2021, 259 pp.